Pizzone, Andrea (2017) *Advanced photon counting applications with superconducting detectors*. PhD thesis.

http://theses.gla.ac.uk/8630/

Advanced photon counting applications with superconducting detectors

Andrea Pizzone

A thesis presented for the degree of

Doctor of Philosophy

School of Engineering

September 2017

Abstract

Superconducting nanowire single photon detectors (SNSPDs) have emerged as mature detection technology that offers superior performance relative to competing infrared photon counting technologies. SNSPDs have the potential to revolutionize a range of advanced infrared photon counting applications, from quantum information science to remote sensing. The scale up to large area SNSPD arrays or cameras consisting of hundreds or thousands of pixels is limited by efficient readout schemes.

This thesis gives a full overview of current SNSPD technology, describing design, fabrication, testing and applications. Prototype 4-pixel SNSPD arrays (30 x 30 μm^2 and 60 x 60 μm^2) were fabricated, tested and time-division multiplexed via a power combiner. In addition, a photon-number resolved code-division multiplexed 4-pixel array was simulated. Finally, a 100 m calibration-free distributed fibre temperature testbed, based on Raman backscattered photons detected by a single pixel fibre-coupled SNSPD housed in a Gifford McMahon cryostat was experimentally demonstrated with a spatial resolution of approximately 83 cm. At present, it is the longest range distributed thermometer based on SNSPD sensing.

Author's declaration

I declare that, except where explicit reference is made to the contribution of others, this thesis is the result of my own work and has not been submitted for any other degree at the University of Glasgow or any other institution. Specifically, I am responsible:

- For mounting the cryostat presented in § **3.2**;
- For the characterization of the detector presented in § **4.3**;
- For the fabrication and characterization of the detector presented in § **4.4**;
- For the simulations presented in § **4.5**;
- For the design of the optical testbed, the optical measurements and the data analysis of the experiment presented in *Chapter 5*.

Acknowledgement

In the last four years, many people contributed to my academic and personal life.

Firstly, I would like to express my sincere gratitude to my supervisor Prof. Hadfield for offering me a scholarship, for the continuous support of my Ph.D. study and related research, for his patience, motivation, and immense knowledge. His guidance helped me in all the time of research and writing of this thesis. I could not have imagined having a better advisor and mentor for my Ph.D. study.

Besides my supervisor, I am forever beholden to the rest of academics who contributed to my research projects: Prof. Marc Sorel, Dr. Nathan Gemmell, Dr. Alessandro Casaburi and Dr. Robert Heath. Through them, my professional skills have improved significantly.

Many thanks also to the other members of the research group who were present all over this journey. Thus, thanks to Dr. Robert Kirkwood who gave me also a tour of London three years ago, thanks to Gavin Orchin, Kleanthis Erotokritou, Luke Baker, Archan Banerjee and to Dr. Mouli Natarajan who had also aligned a detector I needed.

I am deeply grateful toward the Mexican community in Glasgow for adopting me since summer 2014. Some deserved mentions are for Abraham Ortiz, my first friend in Glasgow, for Dr. Gerardo Aragón and Susy Palma, with whom I had the honour to manage the Mexican Society of the University, and for Alan Flores for his everyday friendship, so strong to be felt like a brotherhood.

I would like to thank my friends Eugenio Di Gaetano and Manuel Reza for destressing my days, inside and outside the University. I am very thankful also to my “viking sisters” Anna Bjorkman and Hildur Helgadottir. Their friendships are sweet notes in my life.

I am indebted to my friends Andrea Benecchi and Spyros Lazarakis for hosting me, in their flat, during the last weeks before the submission of the thesis. I will never forget this favour and I will pay it back as best as I can.

I would like to express my appreciations to my whole family. My parents, my uncles, my grandmother and Cristina have always been admirable examples of inspiration. Now we are all called to do even better for Renato.

The last acknowledgment is for the Lord, not only for this adventure in Scotland but for every single day given to me on Earth.

Contents

2.1 Principle of single-photon detection

2.3 Semiconductor based single-photon detectors

2.4 Superconducting single-photon detectors

2.5 Single-photon sensing applications

3.1 Fabrication procedures

3.2 Construction of a 2.4 K Gifford-McMahon cryostat

3.3 Electro-optical analysis

4.2 Large area SNSPD-arrays fabrication

4.3 30 x 30 µm^2 array characterization

4.4 30 x 30 µm^2 array characterization

4.5 On-chip code-division multiplexer for SNSPDs

6.1 SNSPDs arrays: conclusion and prospects

6.2 Distributed fibre temperature sensing: conclusion and prospects

List of tables

List of figures

Glossary

Acronyms

AC	Alternating current
APC	Angled physical contact
APD	Avalanche photodiode
BCS	Bardeen-Cooper-Schrieffer
BSS	Beam step size
CCD	Charge-coupled device
CDM	Code-division multiplexing
CMOS	Complementary metal-oxide semiconductor
CPW	Coplanar waveguide
CW	Continuous wave
DBR	Distributed Bragg reflector
DC	Direct current
DCF	Dispersion compensating fibres
DCR	Dark count rate
EBL	Electron beam lithography
FBG	Fibre Bragg Grating
FDM	Frequency-division multiplexing
FPGA	Field programmable gate array
FUT	Fibre under test
FWHM	Full width at half maximum
GM	Gifford-McMahon
GVD	Group velocity dispersion
HEMT	High electron-mobility transistor
IPA	Isopropanol
LC	Inductor-capacitor
LIDAR	Light detection and ranging
MCM	Miniature confocal microscope
MKID	Microwave kinetic inductance detector
NA	Numerical aperture
OFDR	Optical frequency-domain reflectometry
OSA	Optical spectrum analyzer.
OTDR	Optical time-domain reflectometry
PDM	Polarization-division multiplexing
PMT	Photomultiplier tube
PNR	Photon number resolution/resolving
PPG	Pulse/pattern generator

PT	Pulse tube
QKD	Quantum key distribution
RC	Resistor–capacitor
RIE	Reactive ion etching
RF	Radio-frequency
RR	Repetition Rate
SBR	Signal to background ratio
SDE	System detection efficiency
SDM	Space-division multiplexing
SEM	Scanning Electron Microscope
SFQ	Single flux quantum
SMP	Sub-miniature push on
SNSPD/SSPD	Superconducting nanowire single photon detector
SNR	Signal-to-noise ratio
SPAD	Single photon avalanche diode
SPD	Single photon detector
SPICE	Simulation program with integrated circuit emphasis
SQUID	Superconducting quantum interference device
SR	Spatial resolution
SS	Spot size
STES	Superconducting transition-edge sensor
STJ	Superconducting tunnel junction
TAC	Time to amplitude converter
TDC	Time to digital converter
TCSPC	Time-correlated single photon counter
TDM	Time-division multiplexing
VRU	Variable resolution unit

Greek symbols

γ	Heat capacity ratio
Δ	Energy gap
$\Delta\lambda$	Wavelength shift
$\Delta\varepsilon$	Permittivity mismatch
Δf_{AS}	Bandwidth of the anti-Stokes filters
Δf_{S}	Bandwidth of the Stokes filters
ΔT	Temperature shift
ε	Permittivity
η	Efficiency
$\eta_{absorption}$	Absorption efficiency
η_{AS}	Anti-Stokes optical channel efficiency
$\eta_{coupling}$	Coupling efficiency

$\eta_{registering}$	Registering efficiency
η_S	Stokes optical channel efficiency
λ	Wavelength
λ_{AS}	Anti-Stokes peak wavelength
λ_p	Pump peak wavelength
λ_r	Reflected wavelength
λ_S	Stokes peak wavelength
ν	Frequency
ξ	Coherence length
ρ_{cp}	Cooper pair volume density
σ	Standard deviation
σ_{AS}	Standard deviation of the anti-Stokes histogram
σ_S	Standard deviation of the Stokes histogram
σ_{S_AS}	Covariance of the Stokes and anti-Stokes histograms
τ	Time
Φ	Photon flux
ω	Radial frequency shift
ω_{AS_p}	Anti-Stokes radial frequency shift
ω_{S_p}	Stokes radial frequency shift

Roman symbols

α_Λ	Thermal expansion coefficient
α_n	Thermo-optic coefficient
B_{AS}	Anti-Stokes channel backscattered dark pulses
B_S	Stokes channel backscattered dark pulses
C	Nanowire's cross-section constriction on the critical current
c	Speed of light in vacuum
D_c	Duty cycle
E	Energy
F_{AS_p}	Frequency shift between anti-Stokes peak and pump peak
$g_{R,AS}$	Anti-Stokes Raman gain
$g_{R,S}$	Stokes Raman gain
$\boldsymbol{H}$	Magnetic field
$\boldsymbol{H_c}$	Magnetic critical field
h	Planck constant
$\hbar$	Reduced Planck constant
I	Current
I_{AS}	Anti-Stokes backscattered photo-intensity
I_B	Brillouin photo-intensity
I_b	Bias current
I_c	Critical current

${I^*}_c$	Theoretical prediction of the critical current
I_R	Rayleigh photo-intensity
I_S	Stokes backscattered photo-intensity
$\boldsymbol{J_c}$	Critical current density
k_B	Boltzmann constant
L_0	Inductance of an SNSPD for zero bias
L, L_k	Kinetic inductance
l	Length
m	Electron mass
N	Phonons population
N_c	Number of counted photons
N_{dp}	Number of dark pulses
n	Refractive index
n_b	Average number of background counts per bin
n_p	Number of counts in the maximum bin
P_o	Optical power
p_e	Momentum of the electrons
q	Electric charge
R_{gr}	Raman gain ratio
R_L	Load resistor
R_n	Hotspot resistance
R_S	Shunt resistor
S	Cross-section
T	Temperature
T_c	Critical temperature
V	Voltage
v_f	Fermi velocity
x	position
Z_0	Load impedance

Chapter 1 – Introduction

The detection of light consists in a first step where, after the absorption of photons, an element changes its state (electrical, mechanical or chemical) and a second step in which the collected light-signal, usually analogical and continuous over the time-space domain (or the reciprocal frequency domain) is converted into an electrical unit, reproduced as a numerical/discrete signal in one of the two domains.

A seminal contribution to the study of light was made in the first decade of the XX century when Albert Einstein and Max Planck developed a solution to the “wave-particle duality”. Maxwell’s theory explained that light is no more than a sub-ensemble of the all possible frequencies (spectrum) of the energy from electromagnetic fields (radiations). However, there was still uncertainty about the propagation of light, especially for the microscopic scale. Quantum mechanics, supported by some contradictions after the investigation of the black body radiation, postulated the presence of an undividable packet of light called “photon”, showing both corporeal and waveform properties. Like a wave, it has no mass and no electric charge but like a particle it can exchange energy. Hence, every light-source is a multiple of that packet and the energy E of a single component is equal to $h \cdot c/\lambda$, where h is the Planck’s constant, c is the speed of light in vacuum and λ is the wavelength of a photon. What is ordinarily called light is the energy associated to wavelengths from about 400 nm to 700 nm but, in science, photons at higher (infrared) or lower (ultraviolet) wavelengths follow the same behaviour.

About 40 years later, a device was finally able to isolate a single photon. This detector, called “Photomultiplier tube” [1, 2], can perfectly reveal a single photon in the visible and the near infrared regions of the electromagnetic spectrum. The opportunity to measure signals as weak as single-photons offers the ultimate sensitivity for every purpose in photonics and other kind of measurements correlated to light, e.g. thermal energy.

The progress in semiconductor technology resulted in other kinds of single-photon detectors like avalanche photodiodes, combined with the reliability of time-correlated single-photon counting techniques [3], have already made possible a wide variety of applications, especially in the visible region of the electromagnetic spectrum. Concurrently, there is considerable demand for improved performances at infrared wavelengths (>1 micron). Indeed, Quantum Technology applications require new devices detecting light at the quantum level across the electromagnetic spectrum [4]. The use of single quantum objects (as photons) to encode, process and transmit information is ready to revolutionize not only telecommunications [5], electronics [6] and computer science [7] but other less related research fields, like bio-medicine [8] or fibre-optic sensing [9].

A solid step forward for single-photon sensitivity arrived from superconductivity. In 2001, Gregory Gol'tsman developed thin strips (around 10 nm x 200 nm) patterned by electron beam lithography in an ultrathin superconducting film, usually called Superconducting Nanowires Single-Photon Detectors (abbreviated in SNSPDs or SSPDs). At the time of writing, it is the fastest single-photon-detecting and single-photon-counting technology and can outperform semiconductor detectors [10].

Today, real challenge is the setup of scalable readout schemes for arrays of SNSPDs. Modern applications in telecommunications require a large amount of data to be processed. Therefore, the wider adoption of SNSPDs in real-world applications is deeply linked to the availability of high-density-pixels arrays.

Target of this thesis is to prove that SNSPD fabrication is mature enough to obtain homogenous array to be used in a tangible application like a fibre optic temperature sensor system for deployment in borehole studies for geothermometry.

In *Chapter 2*, an introduction to single-photon sensing technologies and superconductivity is given. In *Chapter 3*, experimental and analytical methods for SNSPDs fabrication and testing are discussed. In *Chapter 4*, results from a 30 x 30 μm^2 and 60 x 60 μm^2 arrays are presented, alongside simulations for an alternative multiplexing scheme. In *Chapter 5*, a fibre temperature sensing setup based on SNSPD is reported. *Chapter 6* is dedicated to conclusions and future developments.

References

[1] Iams, H., & Salzberg, B. (1935). The secondary emission phototube. Proceedings of the Institute of Radio Engineers, 23(1), 55-64.

[2] Zworykin, V. K., Morton, G. A., & Malter, L. (1936). The secondary emission multiplier-a new electronic device. Proceedings of the Institute of Radio Engineers, 24(3), 351-375.

[3] Becker, W. (2005). Advanced time-correlated single photon counting techniques (Vol. 81). Springer Science & Business Media.

[4] Dowling, J. P., & Milburn, G. J. (2003). Quantum technology: the second quantum revolution. Philosophical Transactions of the Royal Society of London A: Mathematical, Physical and Engineering Sciences, 361(1809), 1655-1674.

[5] Robinson, B. S., Kerman, A. J., Dauler, E. A., Barron, R. J., Caplan, D. O., Stevens, M. L., et al., & Berggren, K. K. (2006). 781 Mbit/s photon-counting optical communications using a superconducting nanowire detector. Optics Letters, 31(4), 444-446.

[6] Xiang, Z. L., Ashhab, S., You, J. Q., & Nori, F. (2013). Hybrid quantum circuits: Superconducting circuits interacting with other quantum systems. Reviews of Modern Physics, 85(2), 623.

[7] Takesue, H., Nam, S. W., Zhang, Q., Hadfield, R. H., Honjo, T., Tamaki, K., & Yamamoto, Y. (2007). Quantum key distribution over a 40-dB channel loss using superconducting single-photon detectors. Nature Photonics, 1(6), 343-348.

[8] Gemmell, N. R., McCarthy, A., Liu, B., Tanner, M. G., Dorenbos, S. D., Zwiller, V., ... & Hadfield, R. H. (2013). Singlet oxygen luminescence detection with a fiber-coupled superconducting nanowire single-photon detector. Optics express, 21(4), 5005-5013.

[9] Dyer, S. D., Tanner, M. G., Baek, B., Hadfield, R. H., & Nam, S. W. (2012). Analysis of a distributed fiber-optic temperature sensor using single-photon detectors. Optics Express, 20(4), 3456-3466.

[10] Marsili, F., Verma, V. B., Stern, J. A., Harrington, S., Lita, A. E., Gerrits, T., ... & Nam, S. W. (2013). Detecting single infrared photons with 93% system efficiency. Nature Photonics, 7(3), 210-214.

Chapter 2 – Background review

This chapter introduces the principles of single photon detection, gives an overview of the state-of-the-art in photon counting technologies and introduces important advanced photon counting applications.

2.1 Principle of single-photon detection

An ideal single-photon detector may be defined as a device that converts the energy of every impinging single photon into an immediately generated electrical pulse (photo-electric effect) or into a thermal variation (photo-thermal effect). It is even expected for such detectors to be able to register photons over a wide range of energies. Recalling the remarks in the previous chapter, these energies (E) are inversely proportional to the wavelength (λ) or directly proportional to the frequency (v) of a photon ($E = h\cdot c/\lambda = h\cdot v$). In the real world, practical sensors cannot provide those performances all together, and trade -offs are necessary. Some parameters have been introduced to evaluate single-photon sensors and then determine for which applications they are employable.

2.1.1 Single-photon detection figures of merit

Detection efficiency: A first metric that classifies the performance a single-photon device is the efficiency (η_{QE}). It is a dimensionless quantity counting the number of photons recorded over the total amount of sent photons (i.e. $0 < \eta_{QE} < 1$). It can be viewed as the probability of single-photon detection. Indeed, when a detector is exposed to a photon flux only a fraction of photons is detected due to some independent factors:

- Reflections and scattering effects at the surface of the detector or photo-transmission through the detection layer are frequent. This is mainly due to the structural design of the detector. The remaining fraction of photons represents the absorption efficiency ($\eta_{absorption}$). It should be observed that even $\eta_{absorption}$ is typically related to the material of the detection layer and the wavelength of the source.

- There is a registering efficiency ($\eta_{registering}$) because part of the absorbed photons could not produce an absorption event [1]. In a photoelectric system, the electron-hole pair generated can at times recombine before an avalanche is triggered.
- There is a coupling efficiency ($\eta_{coupling}$) to consider and it does not depend on the properties of the device but on the optical arrangement for a given detector. When the spot size of the photon beam from the light-source is larger than the active area of the detector, only a fraction of photons impinges on the detector surface due to non-ideal optical coupling. While, the previous efficiencies cannot be changed after the fabrication of the device, the coupling efficiency may be usually tuned to a value ≈1 during the test-phase.

In conclusion, a **system detection efficiency** (*SDE*) can be expressed as follows:

$$SDE = \eta_{coupling} \times \eta_{registering} \times \eta_{absorption} \qquad \text{(Eq. 1).}$$

Spectral range: Following on from the above discussion of detection efficiency, it should be taken into consideration that altering the operative wavelength can substantially modify some of the factors determining the *SDE*. To keep the Signal-to-Noise ratio (*SNR*) as high as possible and to satisfy the specifications of a specific photon-counting experiment, it is desirable to maximise the *SDE* at the wavelength of the application itself (Fig. 2.1). It is possible to act on the $\eta_{absorption}$ by placing anti-reflection coatings and optical cavities for a specific wavelength between the substrate and the sensitive area [2].

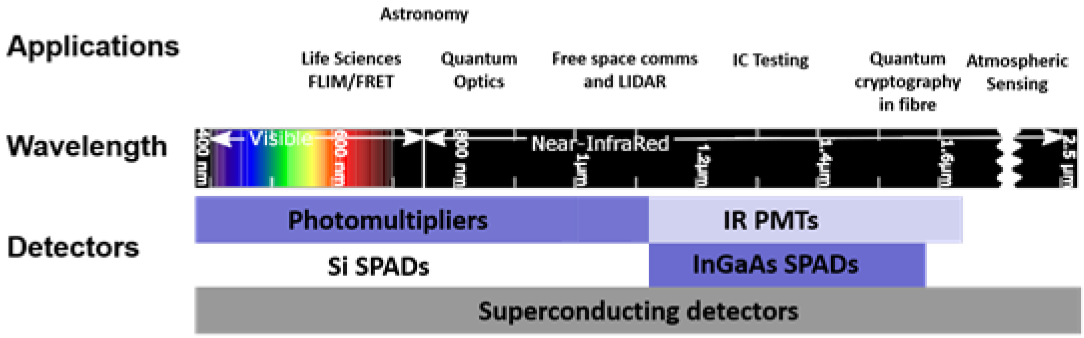

Fig. 2.1: An illustration of single-photon technologies related to the electromagnetic spectrum from visible to mid infrared range and relevant applications.

Dark count rate: A detection event not produced from an impinging single-photon is a form of noise called dark counts. In fact, both thermal and electric noise sources may induce a detector to auto-trigger. External noise sources are cosmic rays, stray light or fluctuations in the readout electronic circuits. Internal noise may be more easily controlled with a cooling of the device that lowers the creation rate of the electron-hole pairs due to thermal processes. However, equipment for the reduction of temperature is ineffective against the tunnelling processes. Additionally, the cooling equipment may generate perceptible electric noise (like ground shifts [3]) that affects other tools in the optical readout. Commonly, dark counts are specified for a 1 second timescale. Thus, a Dark Count Rate (DCR, measured in Hz) is defined.

As this background signal is generated without absorption of photons, DCR may be considered the lower threshold for a detector in sensitivity because there is no way to continuously measure an optical power generating an amount of photons per second lower than the DCR. A manual regulation of the DCR can be achieved by gating the detector or time stamping the detection events.

Timing jitter: In a triggering-event, a conversion-time from the instantaneous optical absorption event to the electrical response can be defined. It is called timing jitter. Neglecting narrow statistical variations, it is a fixed metric of the detector, although certain bias-conditions for the device could have a slight influence.

The jitter is typically computed by measuring the Full Width at Half Maximum (FWHM) from the plot of statistical distribution of time delay between a photon hitting the detector and the observation of an electrical signal output from the detector.

Dead time: After the generation of a pulse, the detection area of a device is insensitive, for a time t_0, to further photon arriving onto it and its detection efficiency is still reduced for an additional time t_{RE}. The sum of these two delays is the dead time, or recovery time, because it is indeed a delay that allows the detector to be as operative as it was before the interaction with an impinging photon. Dead times vary depending on the materials and the technology of the sensor. the jitter sets the minimum clock rate for a single-photon counting experiment without errors caused by inter-symbol interference [4]. Such interference happens if single-photon counts, from different clock cycles, are captured together (i.e. in time domain the adjacent data symbols begin to overlap with each other).

Photon number resolution: A Photon Number Resolving (PNR) device can resolve the number of photons arriving onto the detector in a prefixed time-interval [5]. Largest kind of SPDs can reveal only zero/non-zero photons. PNR features could be emulated through spatial multiplexing using a broadly illuminated array of pixels in simultaneous trigger [6], or time multiplexing as a periodic switch on the input to the same detector [7]. However, the target of next generation detectors is to intrinsically count photon by photon because Quantum Information protocols require single-photon states that are easier to achieve in detection rather than transmission due to the Poissonian statistics governing typical light sources (e.g. lasers).

2.2 From single pixels to arrays

An array of detectors means that identical detectors are replicated with a fixed spatial periodicity. For light detection, a single element in an array is called pixel[1]. The target is to share a resource (namely the readout scheme), expensive in financial, computational or experimental terms. The need for arrays is today demanded by the large amount of data acquisition in modern applications. This is a reason for growing complexity in readout schemes. It is then preferred for such arrays to share one or more readout channels without distorting the pixel data. Several procedures may be adopted:

- **Space-division multiplexing** (SDM): it is the oldest technique and it is a pure separation of the transmission means. In wired communications (e.g. acoustic systems) and wireless ones (e.g. Bluetooth) several channels respect the same data-protocol but deliver different signals from a single transmitter to multiple receivers or from multiples transmitters to a single receiver. The main downside for SDM is the limited manifold of data transmitted and its space occupancy.
- **Time-division multiplexing** (TDM): it is a direct evolution of the space-division multiplexing. It consists in the assignation of a precise time slot for each channel (Fig. 2.2). During a given time, all the signals are recorded in

---

[1] Contracture for “picture element”

series (i.e. data-frame) over a communication channel with a certain order on behalf of electromechanical switches. The composition of the data-frame is shared with the receiver(s). Examples of TDM are cabled telephone protocols and Ethernet. A serious limitation for TDM is that every pixel is totally blind while another is read out. In case of many detectors, it means that all the timing properties are extended by a factor *N*, where *N* is the number of pixels. This is a negative trade-off for detectors with fast responses.

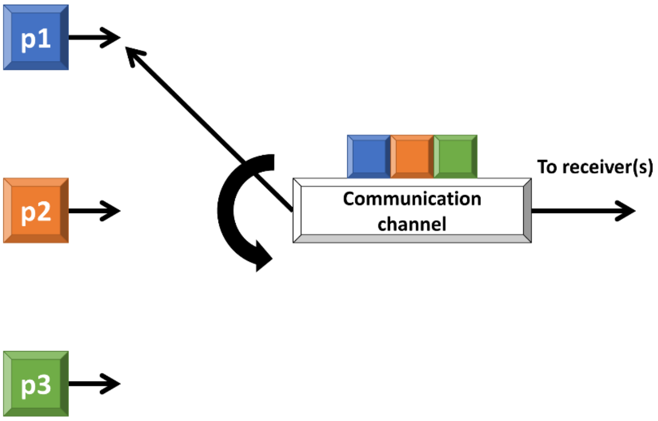

Fig. 2.2: Graphic description of a TDM readout. Three pixels (p1, p2, p3) share the same communication channel in different times, regulated by a switch. The data-frame will be properly interpreted by one or more receivers.

- **Frequency-division multiplexing** (FDM): It is a combination of several signals sent at distinct frequencies over a single medium. To do that, signals from different pixels are modulated by a different carrier and then summed (Fig. 2.3). FM-Radio broadcasting is a clear example of FDM. In optical communication FDM is more often called wavelength-division multiplexing. The main drawback for FDM relies in its intrinsically analogue nature.

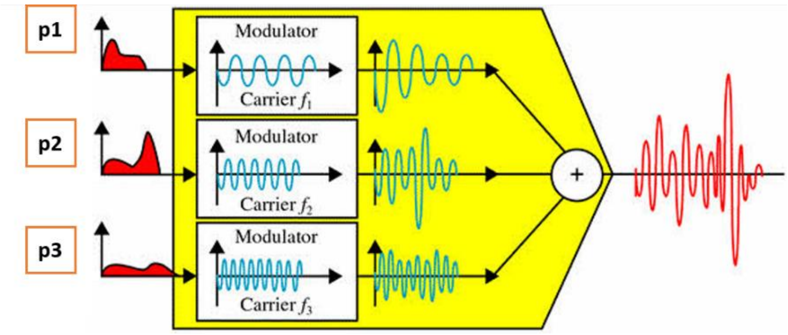

Fig. 2.3: Graphic description of a FDM readout. Three signals from different pixels (p1, p2, p3) are modulated by three carriers (f_1, f_2, f_3). The signals are later added and sent to a single communication channel.

Digital signals shall pass through Digital-to-Analog converters. In some cases, this could introduce too many extra circuits, sacrificing the simplification obtained by a single channel readout.

- **Polarization-division multiplexing** (PDM): The polarization of electromagnetic radiation to separate orthogonal channels at the same frequency can be an alternative multiplexing scheme. It is in practical use in both radio and optical communications. PDM however can only double the available bandwidth into the so-called horizontal and vertical frequencies (Fig. 2.4). In real-world applications, like satellite television broadcasting, PDM is always employed jointly with FDM.

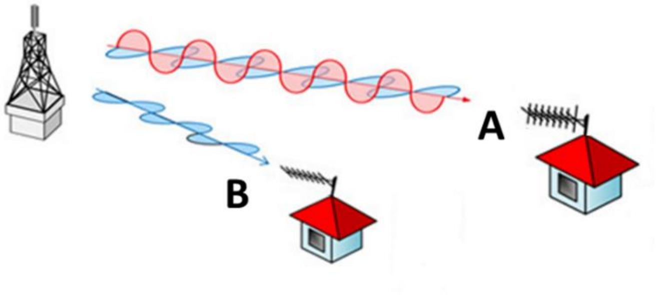

Fig. 2.4: Graphic description of a PDM signal (A) versus a FDM signal (B). The antenna A may receive two signals per frequency while the antenna B receive only one.

- **Code-division multiplexing** (CDM): it is a spread-spectrum technique. Simply put, the bandwidth of the data is spread uniformly for the same transmitted power. Then, each signal is associated to a different digital code, usually in amplitude (Fig. 2.5).

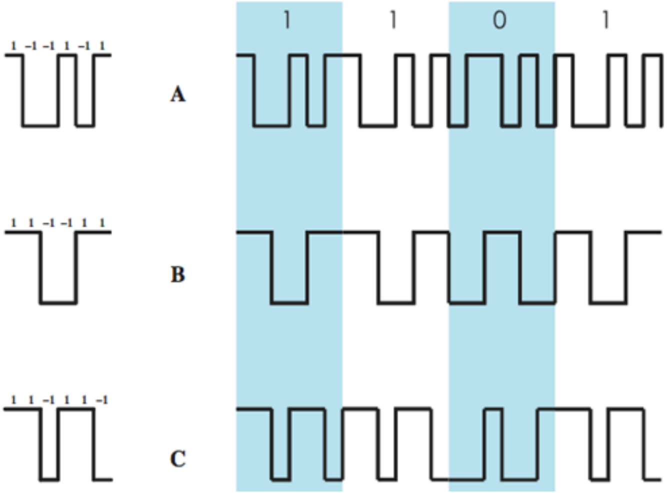

Fig. 2.5: Graphic description of a CDM scheme. The same signal (Message "1101") has a unique association with each channel (A, B, C).

CDM can be considered a digital FDM. Hence analogue signals shall pass through Analogue-to-Digital converters, sharing similar circuitry-issues from FDM.

It is important to remark that multiplexing can be modular. Some detectors can be grouped and processed at a lower level with a given multiplexing technique and then processed again, at an upper level, with a different scheme.

2.3 Semiconductor based single-photon detectors

2.3.1 Photomultiplier tubes

The first ever photodetector demonstrating the ability to record single-photons is the photomultiplier tube (PMT), in 1949 [8]. The main idea had arisen in 1902 after the observation of secondary emissive surfaces. Indeed, PMTs make use of a repetitive phenomenon of photoelectric emissions. A basic PMT comprises of a vacuum tube with a photocathode (in GaAsP usually) for light absorption.

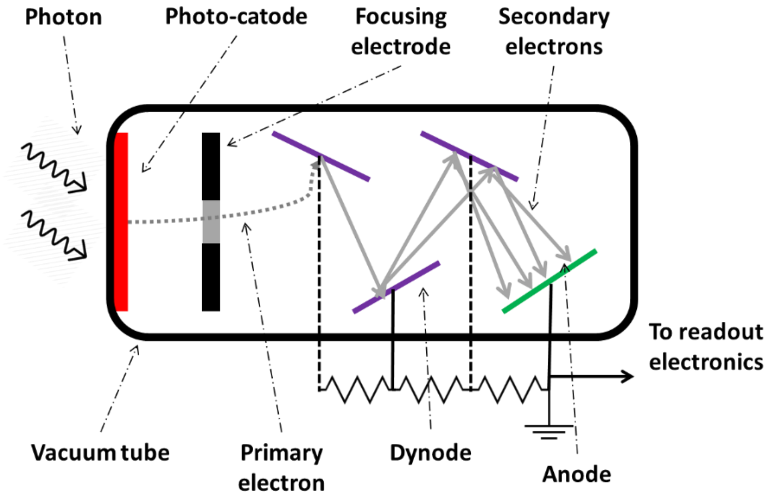

Fig. 2.6: The photomultiplier tube operating principle: the absorbed photons are converted into electrons by a photo-emissive cathode. A focusing electrode converges the photoelectrons towards the first dynode. Next dynodes, biased at higher voltages, emit several secondary electrons for each photoelectron absorbed achieving amplification. The anode collects enough electrons from the final dynode for external readout.

When a photon has an energy higher than the work function of the photocathode material, electrons are emitted from the photocathode (the so called photoelectric effect) into the vacuum tube, passing through a focusing electrode. This few-electron photocurrent is hence multiplied by a cascade of secondary electron-emissions from dynodes (a chain of electrodes, each one biased at a positive voltage higher than the previous one) producing a current pulse of >10^6 electrons (Fig. 2.6). At the end of the process, the multiplied electrons are absorbed by the anode and magnitude of the current measured at the anode is proportional to the intensity of light [9]. Performances of such devices depend strongly on the operation wavelength. Thickness and work function of the photocathode material affect the spectral range of the PMTs sensitivity. Optimized compounds boost magnitude and width of the spectral response. In the middle of the visible region of the electromagnetic spectrum (~540 nm, associated with the green colour from the human eye) the *SDE* can be around 40% with a DCR around 100 Hz [10] whereas in the infrared (~1550 nm) *SDE* is ~2% and DCR is 200 kHz [11]. Moreover, for both cases the best time jitter is ~300 ps and the maximum count rate about 10 MHz.

Dark pulses in PMTs are proportional to the applied voltage because they originate from thermionic emission and ohmic leakage from electrodes. After-pulses can be observed in PMTs due to elastic scattering of electrons in the first dynode. Ionization of internal residual gases is another reason for after-pulses. To overcome the last situation, hybrid photodetectors (a photocathode with a low-capacitance avalanche photodiode) were designed just to have a bias of ~400 V and few improvements in terms of DCR (1 kHz) and timing jitter (61 ps) [12]. Another modern upgrade in this technology is the realization of micro-channel plate PMTs (Fig. 2.7), where glass capillaries are fused in parallel and coated with a secondary electron-emitting material to achieve a single continuous dynode under a bias voltage [13]. In this way, timing jitter can be reduced to as low as ~20 ps.

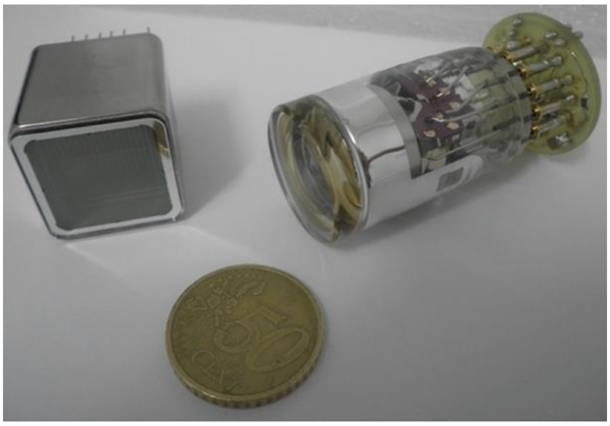

Fig. 2.7: Photomultiplier tubes compared with a 0.5 € coin.

The multichannel extension for the first ever single-photon technology arrived in 1969 [14]. The original scope was to reduce the integration time for star-sky spectrometers using 16 PMTs. The readout was based on solid-state amplifier discriminators, that receive the output signals from each PMT, all in series with a dual-pulse counter that switches between its two states with a prefixed period. For the reasons previously explained (see § **2.2**), this multichannel device cannot be defined as a proper array. Two years later Beaver and McIlwain proposed a linear array of PMTs [15]. A series of voltage rings is placed between a cathode and 38 p-n junctions, each one connected to an external amplifier, discriminator and digital accumulator for detection of photoelectron arrivals. As a light-beam hits the p-n junctions, a signal count rate as a function of the position of slit on the array can be measured.

Price and the difficulty of obtaining micro-channels covering large areas combined with mechanical fragility, restricted the commercial success for PMTs array until mid-80s. Companies like Philips and Hamamatsu developed 64 channel PMTs based on optimized secondary electron emission [16]. Multiplexing in position and intensity of the light source derives from the value of the current measured on the anode pin on behalf of a voltage divider (*RC* grids) [17]. The key downsides for such PMT architecture are the uniformity (mainly in terms of gain) of the channels and a destructive cross-talk. Performances were improved [18] but even with minor upgrades (like pad matrix anode layout [19]) the general readout for PMTs array is still based on charge division *RC* circuits [20].

2.3.2 Single photon avalanche diodes

Avalanche breakdown is a phenomenon observed in both insulating and semiconducting materials. It is a form of electric current multiplication that can allow very large currents within materials which are normally good insulators. The presence of an electric field, deriving from a voltage applied across the device, accelerates carriers in the depletion region. When carriers acquire energies sufficient to create mobile or free electron-hole pairs via collisions with bound electrons (Fig. 2.8), an electron avalanche process occurs.

Avalanche photodiodes convert the absorption of an incident photon into an electric pulse exploiting the photon-triggered avalanche current of a reverse-biased p-n junction. In reverse bias, the p region is connected to the negative terminal of the voltage source while the n region is connected to the positive terminal. The way to detect the energy of single-photons (single-photon avalanche diodes, SPADs) is to apply such a bias slightly above the avalanche breakdown voltage, with no current flowing.

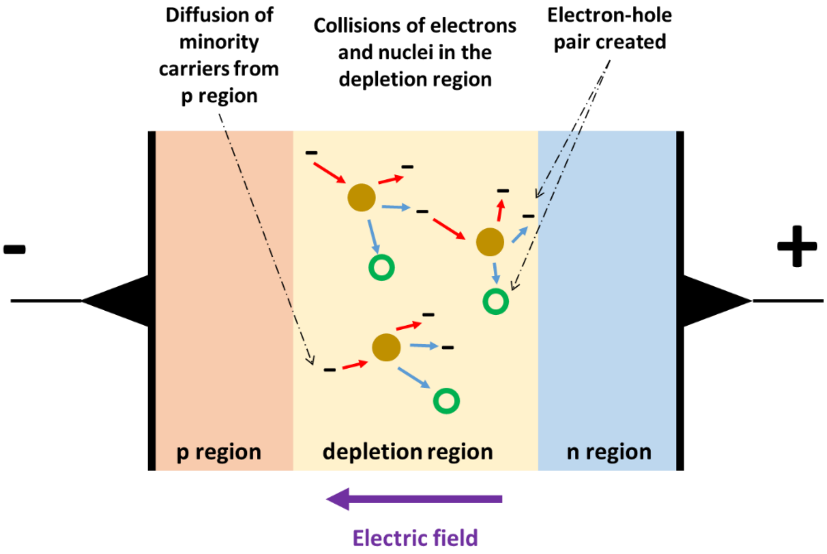

Fig. 2.8: Illustration of the basic multiplication process in an avalanche photodiode. The p-doped region is populated by positive charges (holes) and the n-doped region is populated by negative charges (electrons).

This kind of operation is also called Geiger mode in literature, as opposed to linear mode in a conventional photodiode (Fig. 2.9). Under such conditions, the avalanche created by the absorption of a single-photon generates a macroscopic current. Once a photon gets detected, the avalanche may be left to dissipate [21, 22] or be actively arrested by bringing down the bias voltage below the breakdown threshold. At this point, the SPAD is ready for a new photo-detection event [23].

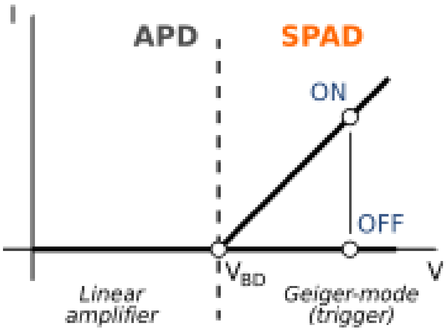

Fig. 2.9: *I-V* characteristics for conventional avalanche photodiode (APD, Linear amplifier) and a single photon one (SPAD, Geiger mode). (V_{BD}: Voltage breakdown).

The energy gap between the valence band and the conduction band of the material of the diode affects which operating wavelength range the device can support. Silicon (Si) has a bandgap of 1.1 eV, hence Si SPADs can operate from visible to near-infrared wavelength, with a cut-off wavelength around 1.13 µm Si SPADs with 65% efficiency [24] in the visible/NIR (650 nm) or 20 ps jitter were demonstrated [25]. Without incident light, small currents may still flow across a Si SPAD, generating dark counts. Electron-hole pairs over the device could be generated by thermal energies rather than photons; tunnelling effects would also create a current.

For telecommunication (abbr. telecom) wavelengths (1310 nm – 1550 nm) Si SPADs are ineffective due to the 1.13 µm cut-off. A key advance in SPAD architecture was the separation of absorption and multiplication layers to improve distinctly electron-hole pair generation and avalanche multiplication [26]. A heavily doped thin region (InP), sustains the very high electric field necessary for avalanche multiplication, while a lightly doped thick region supports the electron-hole pairs generation, favouring absorption of single-photons. This method has made InGaAs/InP SPADs, whose cut-off is around 1.7 µm, suitable for telecom applications.

The integration of resonant optical cavities and SPADs can improve the detection efficiency at telecom wavelengths [27]. State-of-the-art InGaAs SPADs have ~66% efficiency at 1572nm [28]. On the other hand, InGaAs/InP SPADs intrinsically have high DCR, mainly originating from after-pulses. The high probability of after-pulsing depends on minority carriers trapped in sub-levels of the energy bandgap, created by the InGaAs and InP interface (Fig 2.10). Minority free-carriers escape from traps after a variable time window and re-trigger avalanche multiplication. In order to prevent these pulses, the number of free carriers existing in interface sub-levels should be minimized. This is possible by reducing the bias well below the breakdown voltage as soon as the avalanche is observed.

In other words, SPADs work in gated mode by repeatedly biasing above the breakdown voltage only for a short amount of time (∼200 ps).

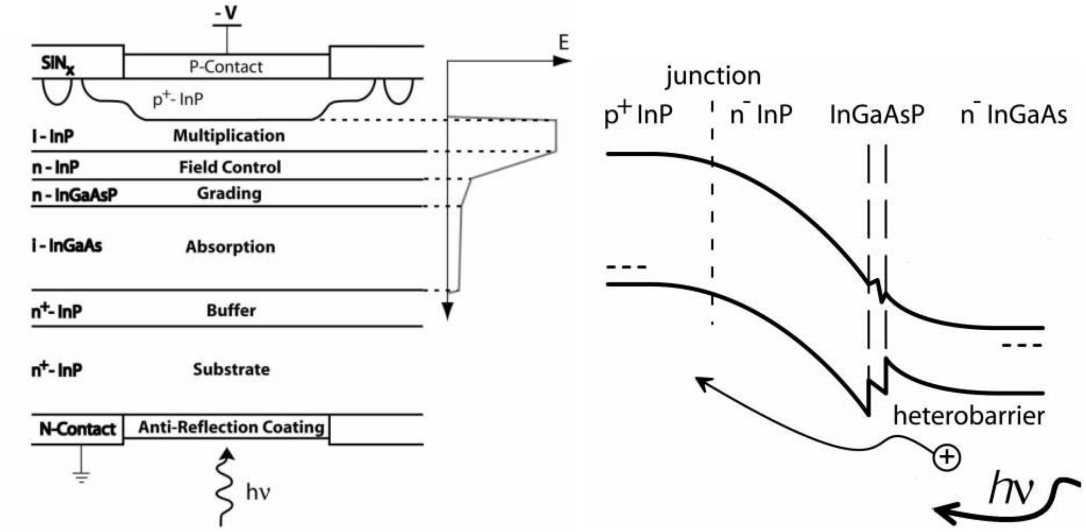

Fig. 2.10: InGaAs/InP SPAD structure. On the left, schematic cross-section of a separate absorption and multiplication. On the right, band diagram shows the trap energy levels at the InGaAs/InP interface. Reproduced from [22].

Rochas *et al*. reported firstly an integrated array of 32 Si-SPADs [29]. The readout electronics divide the array in 4 groups of 8 pixels, all biased with the same high negative voltage V_{OP}, singularly combined with a quenching resistor placed in series between the SPAD cathode and the voltage supply line V_{DD} while a diode placed between the gate and V_{OP}. The internal multiplexing in each group is obtained by a switch-circuit externally controlled by a 3-bit selection address. Summarizing, the array integrates 4 independent readout terminals, individually operating an 8-pixel TDM interrogation.

The number of pixels has increased rapidly, also supported by semiconductor technology progress. Zappa *et al*. fabricated 240-pixel silicon array [30] composed by 60 quad-cells whose SPADs present different diameters. All the 60 cells may operate in parallel thanks to its own set of bonding pad but only one detector per cell can be active.

Niclass *et al*. designed an event-drive readout architecture on a 4 x 112-pixel silicon array [31]. In the event-driven approach, a column is transformed into a digital bus. Briefly, a pulse propagates from the pixel who had detected a photon to the end of its column, recorded by a multichannel Time-correlated single photon (TCSPC) module. The time of arrival and the TCSPC channel on which the pulse is collected provides complete pixel identification. In recent years, both single-pixels and schemes have been optimized [32, 33] but the multiplexing mechanisms is not changed. For what concerns InGaAs SPAD arrays, a state-of-the-art camera was recently released on the market. The 4096-pixels array performance (per pixel) at 1064 nm is ~40% efficiency at ~2 kHz DCR, while at 1550 nm the efficiency is ~30% with ~6 kHz DCR [34].

2.4 Superconducting single-photon detectors

2.4.1 Introduction to superconductivity

Superconducting materials show two specific properties when cooled below a certain temperature T_c, called critical temperature:

- Electrical resistance equal to zero.
- Perfect diamagnetism ($\boldsymbol{H} = 0$).

At higher temperatures, they are normal metals and not necessary good conductors. For instance, lead and tantalum are superconductors; conversely the noble metals gold and silver are not. The first superconducting property implies a perfect electrical conductivity. This was firstly noticed in 1911 by H. K. Onnes who observed the electrical resistance of mercury (Hg) dropped to exactly zero at 4.2 K [35]. It can be formalized as a transition from a normal to a superconducting state (Fig. 2.11).

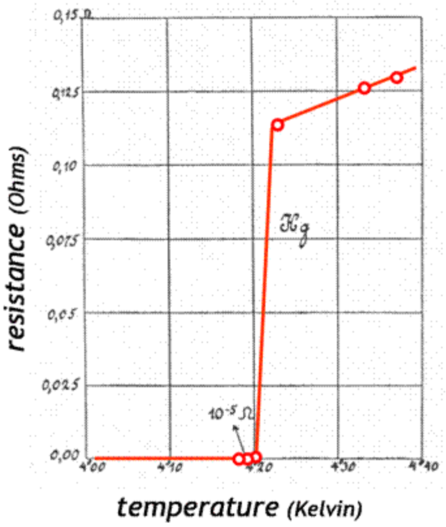

Fig. 2.11: Resistive behaviour of Hg in the interval 4-4.4 K.

Although the theoretical transition from the normal to the superconducting state is very sharp, experimentally it may be gradual or abrupt. Nonetheless, the sharpness of the drop to zero resistance is an index of purity and homogeneity. The onset of superconductivity is important in physics because it suggests that superconducting regions are being formed. On the other side, the zero point in resistance is important in electronics because it means the material can carry a super-current up to a certain critical current density $\boldsymbol{J_c}$ [36]. Such supercurrent can be observed as a transport current density, until a critical value, that will induce a critical field $\boldsymbol{H_c}$ at the surface and brings the superconductor to its normal state. As the Earth's magnetic field is around 10^{-9} T, practically always below $\boldsymbol{H_c}$, a superconductor requires the application of a sufficiently strong magnetic field that turns its resistance to switch to the normal state value.

Summarising, the superconducting state can only exist below three critical parameters (current, temperature and magnetic field) simultaneously satisfied, which can be plotted in a 3-dimensional space to visualize a superconducting critical surface (Fig. 2.12).

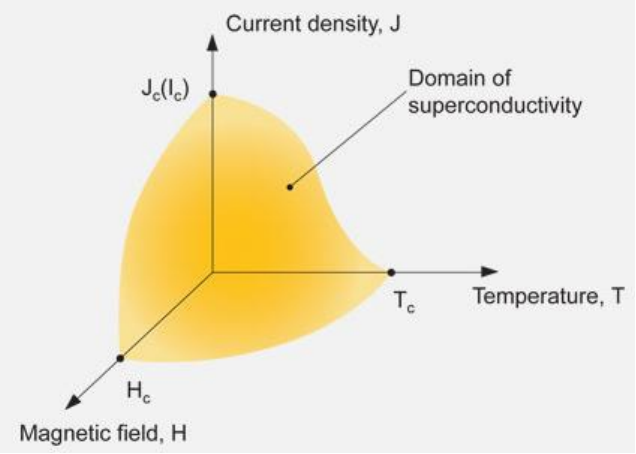

Fig. 2.12: Example of critical surface for a superconductor. Temperature must be below the critical temperature $\boldsymbol{T_c}$ as magnetic field below the critical field $\boldsymbol{H_c}$ and current density lower than the critical current density $\boldsymbol{J_c}$.

Those observations, however, do not explain why, in such circumstances, the laws of the ordinary conduction are not respected. In classical physics, electrical conduction consists in a flow of electrons moving through a lattice. This flow gives rise to a continuous series of collisions, between the electrons and the ions in the lattice, transforming part of the internal kinetic energy into dissipated heat (Joule effect) and this creates an electric potential difference (Ohm's Law). Here, temperatures close to the thermodynamic absolute zero should block this flow. Indeed, superconductivity can be justified only by quantum mechanics.

In 1950, Ginzburg and Landau developed a phenomenological theory for the superconducting transition phase, whose mathematics match the macroscopic properties for the so-called Type I superconductors[2]. In brief, the free energy of a superconductor near the transition can be described by a complex order parameter which is nonzero below a phase transition into a superconducting state and is also a function of a superfluid comprised of electrons contributing to the superconducting state [36].

The first model to microscopically describe Type I superconductivity was the BCS theory [37], named after its inventors: J. Bardeen, L. N. Cooper, and J. R. Schrieffer. BCS theory assumes there is energy gap Δ at the Fermi level. The band gap suggests a phase transition in which there is a condensation of charge carriers, like a Bose-Einstein condensation, but electrons alone cannot condense into the same energy level (Pauli exclusion principle). Hence, if current flows across a superconductor, a drastic change in conductivity demands a drastic change in electron behaviour. Therefore, at the ground state (0 K), the Fermi level is occupied by bosons, the so-called Cooper pairs, coupled pairs of quasiparticles with antiparallel spin. As the temperature approaches T_c, the thermal excitation breaks up an increasing number of Cooper pairs. The dissociation of a Cooper pair yields two quasiparticles: excited electrons surrounded by holes in a lattice. The interactions among electrons are governed by phonon vibrations (oscillations in the lattice of the superconductor caused by thermal agitation). An electron moving through the lattice attracts the closest positive charges (ions), locally deforming the lattice. In response, another electron is forced to move toward this more ionized spot (Fig. 2.13). The bandgap Δ is indeed the binding energy of two quasiparticles; when higher than the kinetic energy due to the thermal fluctuations of the atoms in the spot, two quasiparticles respond as an aggregate. Their distance is called superconducting coherence length and may be considered a size of a Copper pair. Written v_f as the Fermi velocity, the superconducting coherence length can be computed as follows:

$$\xi = {}^{h \cdot v_f}\!/_{\pi^2 \Delta} \qquad \text{(Eq. 2).}$$

At 0 K, the energy gap Δ is 1.76 $k_B T_c$; for a temperature $T \cong T_c$ the bandgap ratio can be written as:

---

[2] Type I superconductors never allow a magnetic field internally. Conversely, there are Type II superconductors allowing magnetic fields in some circumstances.

$$\frac{\Delta(T)}{\Delta(0)} = 1.76\sqrt{1-\frac{T}{T_c}} \qquad \text{(Eq. 3).}$$

The equation states that the energy gap rises progressively from 0 (at $T = T_c$) to 1.76 $k_B T_c$ (at 0 K) [35].

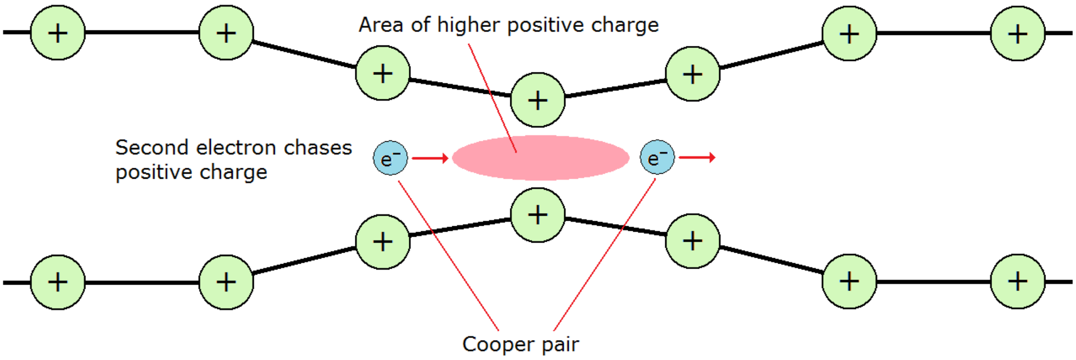

Fig. 2.13: Illustration of Cooper pairs. The ions in the lattice are represented as green circles with a positive electric charge.

Further peculiarity in superconductors is the kinetic inductance. Every charge carrier, owing a mass m and moving with a speed v, possesses a kinetic energy:

$$E_k = \frac{1}{2}mv^2 \qquad \text{(Eq. 4).}$$

The loss of energy due to Joule heating in ordinary conduction is orders of magnitude higher than the accumulated kinetic energy. In superconducting materials, below T_c, there is practically no Joule effect and Cooper pairs mass and charge are twice the electrons mass and charge. Be l and S the length and the cross-section of a superconductor, be q the electron charge, and be ρ_{cp} the Cooper pair volume density, then (according to the Drude model) the current generated in a superconductor is:

$$I = S \cdot \rho_{cp} \cdot v \cdot 2q \qquad \text{(Eq. 5).}$$

Combining Eq. 4 and Eq. 5 and considering the amount of charge carriers in a superconductor ($S \cdot \rho_{cp} \cdot l$), it is possible to define [38]:

$$E_k = \frac{1}{2}(2m)\left(\frac{I}{S \cdot \rho_{cp} \cdot 2q}\right)^2 \cdot \left(S \cdot \rho_{cp} \cdot l\right) = \frac{1}{2}L_k I^2 \qquad \text{(Eq. 6).}$$

Dimensionally, is an inductance but it stores energy in the form of kinetic energy of the charge carriers and therefore it is called kinetic inductance.

2.4.2 Superconducting tunnel junctions

In superconducting tunnel junctions (STJs), two superconductors are coupled by a thin insulating layer (typically Al_2O_3 between Al, Nb or Ta). Single-photon detection is possible because as a photon hits the superconducting layer, Cooper pairs at the ground state get broken, generating a number of quasiparticles proportional to the energy absorbed in the metal (Fig. 2.14). These charges tunnel across the thin barrier layer resulting in a temporary measurable current (namely the Josephson effect). Such current includes a component, namely the Josephson current, due to part of the Cooper pairs crossing the insulating barrier. To eliminate the Josephson current, a magnetic field around 5 mT shall be applied laterally across the junction. Another issue is represented by the operational temperature, usually below 1 K, in reason of the critical temperatures of the materials employed. Additionally, the STJ responsivity is poor because only quasiparticles near the barrier contribute to photodetection.

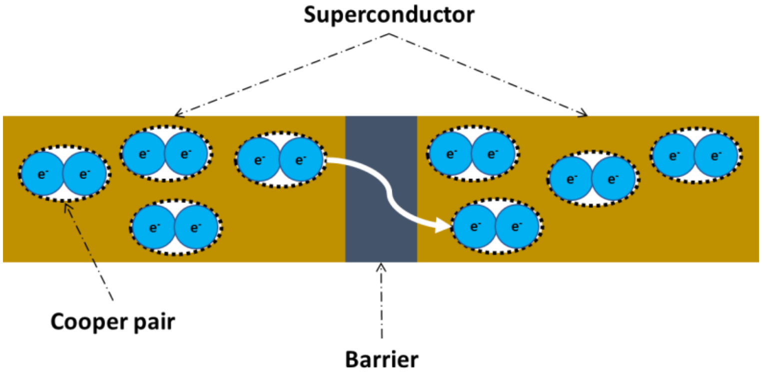

Fig. 2.14: Diagram of a superconducting tunnel junction. Only Cooper pairs close to the barrier are involved in the photodetection process.

Scalability to large-area arrays introduces further issues; STJs are typically read out by room-temperature charge-sensitive amplifiers. The connecting wires running to the detector need to be shielded, which always remains a challenge as thermal decoupling between cooling stages still needs to be ensured. In addition, the wires need to be mechanically affixed. Some vibrations, in fact, may lead to meaningful charge displacements.

But STJs arrays were frequently investigated and applied in several fields. In 1979, Rudner and Claeson presented a 40-pixel linear array of Pb-O-Pb STJs [39]. The configuration was designed as a low-noise 9 GHz mixer. A 115 GHz mixer was achieved with a similar setup [40]. Array of STJs were also successfully tested in absolute thermometry [41]. From the current passing through the junction, the tunnel rate is calculated and that is proportional to the temperature.

In recent times, terahertz imaging was performed with Nb STJs. The detector is composed of 100 linearly distributed junctions placed on a superconducting micro-strip line and is integrated on two wings of a log-periodic antenna [42]. In terms of number of pixels, the largest STJs array is the S-CAM [43], a cryogenic camera for ground-based optical astronomy: 10 x 12 pixels sensing the interval of wavelengths 330 - 750 nm. The pixels are electrically divided into four groups of 30 STJs. Each pixel in a group has its own electronic readout chain at room temperature collected by an FPGA[3] module, performing time-domain multiplexing over the group.

State-of-the-art STJs have ~50% efficiency in the visible region of the electromagnetic spectrum and such technology is still employed in astronomy and low-temperature applications because of a good energy resolution: for photon energies between 1 eV and 1 keV, Nb STJs show resolution between 0.13 eV and 4.3 eV FWHM [44].

2.4.3 Superconducting quantum interference devices

A Superconducting quantum interference device (SQUID, [45]) is a detector that measures minimal variations in magnetic flux. Like STJs, SQUIDs are based on the Josephson effect.

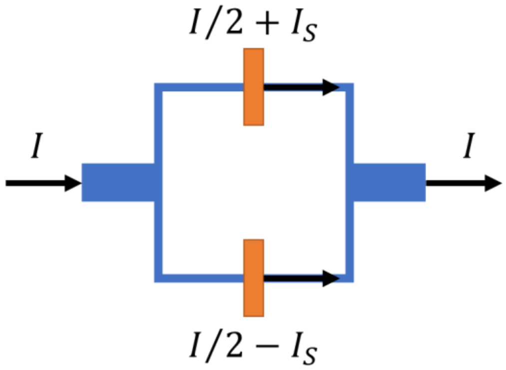

Fig. 2.15: Graphic illustration of the operating principle of a superconducting quantum interference device. An external magnetic field is balanced by a screening current I_S. When the total current in one of the branches (Josephson junctions) of the ring exceeds the critical value, a voltage is measurable across the junction and it is proportional to the magnetic field applied.

---

[3] Field Programmable Gate Array

Invented in 1964 [46], SQUID (Fig. 2.15) is a superconducting ring where two small insulating layers have been inserted (Josephson junctions, [47]). If the external magnetic field is nihil, the input current I is equally divided between the two junctions. But when the external magnetic field perturbs the device, a screening current I_S circulates over the ring, deleting the applied flux. As the output current is equal to the input one, I_S is present on both the junctions with opposite sign ($I/2 \pm I_S$). As soon as the current in one of the junctions overcome the critical value, a voltage can be measured across the junction and it is proportional to the magnetic perturbation.

2.4.4 Superconducting transition-edge sensors

Superconducting transition-edge sensors (STESs) are a type of cryogenic energy/particle sensor making use of the temperature-dependent resistance when a superconductor switches between the normal and superconducting states [48]. After that, a thermal variation is observed by the thermometer and recorded as a single-photon detection event (Fig. 2.16).

STESs operating at the visible or IR wavelengths usually have a tungsten (W) absorber layer, around 20 nm thick, whose temperature increases to a value depending on the energy of the absorbed photon. The absorber lies on a Si substrate maintained at 40 mK in an adiabatic demagnetisation refrigerator acting as the heat sink. The thermal equilibrium is indeed restored by dissipating heat into the heat sink via a thermal weak link represented by the low electron-phonon coupling in the absorber that switches from superconducting to normal state with a transition width below 1 mK (T_c ~178 mK). The detector is voltage-biased to maintain the W film at the midpoint of the superconducting-to-normal transition by negative electro-thermal feedback [49]. When a photon is absorbed by the tungsten film, the generated photoelectron heats the tungsten electron system. As the temperature increases, the resistance becomes higher and therefore the current decreases. The small change in current is detected via a highly sensitive superconducting quantum interference device readout [50]. The sensor recovers subsequently due to reduction in Joule heating. The energy of the photon can be computed by the total sum of the product of current variation (time-dependant) and a constant bias voltage.

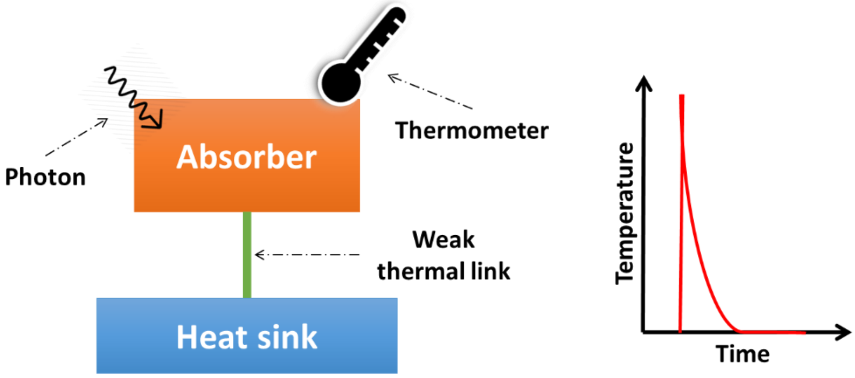

Fig. 2.16: Graphic illustration of the operating principle of a superconducting transition-edge sensor. Photo-absorption increases the temperature of an absorber, whose heat is progressively dissipated to a heat sink via a weak thermal link.

STESs have high detection efficiency at visible and near infra-red wavelengths. The best efficiency in literature is 95% at 1556 nm was demonstrated by integrating the W absorber within an optical cavity designed to enhance the absorption for that wavelength [49]. Also, STESs were able to enumerate 7 photons per pulse [52] and energy resolutions of ~0.3 eV, allowing PNR experiments. DCR in STESs is generally low (less than 0.1 Hz). The disadvantages of this technology are represented by a recovery time of ~100 ns and the need for sophisticated cryostats (≈300 mK) to operate as they are susceptible to triggering by background black body radiation.

The first smart solution for large area TES arrays arrived from Chervenak *et al*. [53]. The scheme derives from a single cell readout where the inductive coil of the sensor provides a signal flux for a SQUID. To achieve a complete readout, four pairs of wires are required:

I. For the input sensor
II. For the feedback flux
III. For the SQUID bias current
IV. For the output voltage

Among all such pairs, only the first one cannot be shared when scaled to large arrays. Therefore, the outputs of many SQUIDs may be connected in series (column of SQUIDs). Turning on the SQUIDs sequentially to time division multiplex the input signals drives to just two wires per column dedicated to the output voltage and two wires per column for the feedback flux. The initial 2*N* bias current wires are reduced to N+1. Furthermore, in an M-columns parallel, those N+1 wires may resolve the entire scheme. Some slight variations to the schematic were studied [54, 55]. In conclusion, 2M+N+1 leads to room temperature are required for M x N arrays.

Multiplexing is even obtainable using a single SQUID. Each sensor is biased with an alternating current at a distinct frequency significantly above the roll-off frequency of the sensor and all the signals are inductively coupled to a superconducting summing loop. Assuming all sensor transformers have the same sensor-side inductance, summing loop-side inductance and mutual inductance, the SQUID measures the current in the summing loop via a conventional coupling coil. Feedback from the SQUID-output is used to null the total current in the summing loop. The absence of any net current flowing in the summing loop eliminates direct crosstalk between channels.

2.4.5 Microwave kinetic inductance detectors

Microwave Kinetic Inductance Detectors (MKIDs) are low-temperature detectors in which the formation of quasiparticles, due to the incident radiation, is detected as a change in the surface impedance of a strip of superconductor integrated in a microwave resonator.

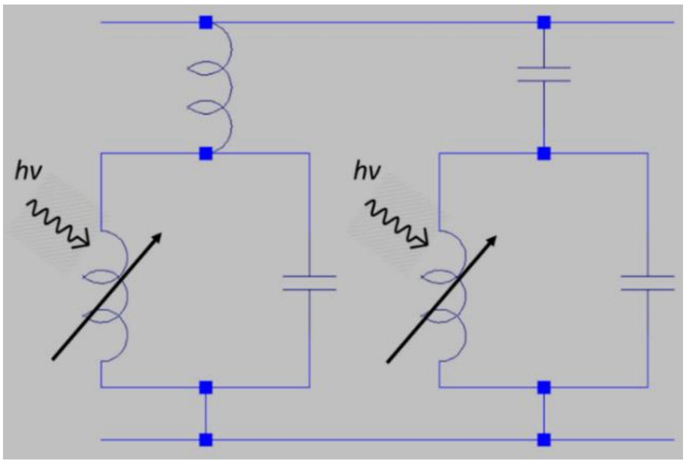

Fig. 2.17: MKID equivalent electrical schematic. A variable inductor is in parallel with a capacitor. The connection with the readout electronics can be implemented by employing a second inductor (left) or a second capacitor (right).

The equivalent circuit for an MKID is an LC resonator with a further capacitor or inductor coupling the device to the readout electronics (Fig. 2.17). The variation of the surface impedance sequentially changes the resonance frequency and quality factor of the resonator (Fig. 2.18), affecting the phase of a microwave signal transmitted through the resonator.

MKIDs suffer some major downsides. The principal noise source of MKIDs is related to fluctuations in the kinetic inductance due to the random generation and recombination of thermal quasiparticles in the superconductor. Secondly, the sensitivity at millimetre wavelengths is generally lower than other superconducting technologies. That is due to factors such as sky-noise, the black body emission of the atmosphere. Lastly, the fastest recovery time achieved by an MKID is around few microseconds [56], much higher than other technology.

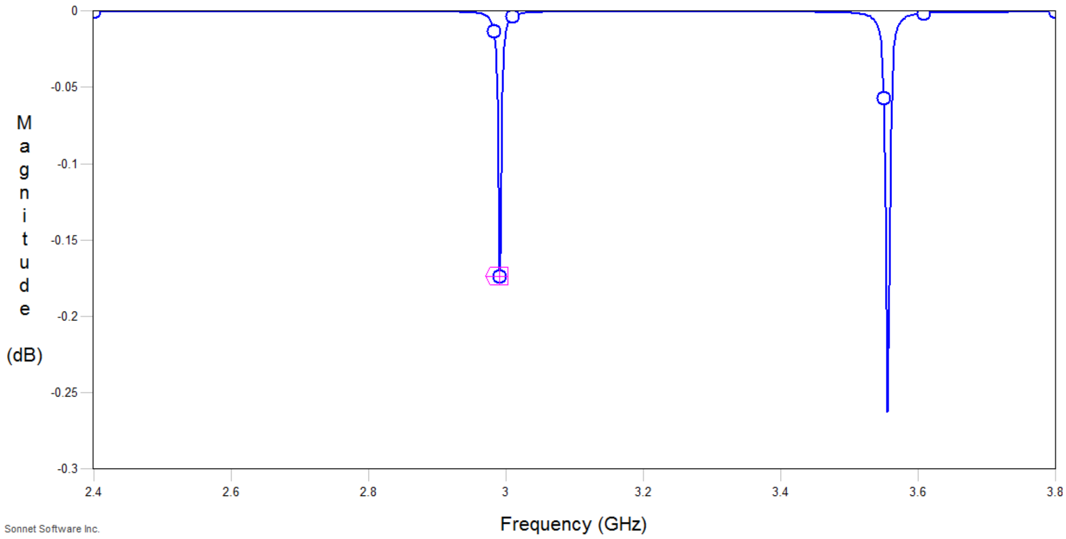

Fig. 2.18: Simulated response of two different MKIDs. As expected, the resonant frequency and the quality factor changes.

Due to the property of detecting via resonances separated in the frequency domain, a huge number of superconducting KIDs can be fabricated embedded in a single microwave waveguide on a single chip or wafer. Non-overlapping resonances can be simultaneously read out by measuring the complex outcoming signal of a superposition of harmonics. Only two coaxial cables are therefore necessary between the cryogenic device and room temperature.

This technology was powered by the development of a cryogenic microwave amplifier called High Electron-Mobility Transistor (HEMT, [57]).

Maloney *et al*. [58] reported a 576-pixel camera, resolved in four wavelengths (850, 1100, 1300 and 2000 µm) and tested at 4 K. The array is divided in eight tiles of 6 x 12 pixels and every pixel contains four resonators (one per wavelength). The readout scheme adopted in each tile is the following: each pixel is excited by a ~3 GHz AC bias traveling over a coplanar waveguide (CPW, [59]); the outcoming signal, passed through HEMT and low-noise amplification, is collected by an FPGA, in order to measure phases and amplitudes of the readout harmonics [60].

McHugh *et al*. [61] presented a denser array (32 x 32 pixels) tested at 100 mK multiplexed in the same way but compressing the bandwidth of resonances within ~2 GHz.

2.4.6 Superconducting nanowire single-photon detectors

Superconducting nanowire single photon detectors (SNSPDs) are the principal emerging photon counting technology studied in this thesis. Gregory Gol'tsman first demonstrated this technology (now known as the SSPD or SNSPD) in 2001 [62]. The first SNSPD device is a thin superconducting strip, around 10 nm thick and 200 nm wide and a few micrometres long. The strips are patterned by electron beam lithography and etched in an ultrathin superconducting film. The film for the initial devices were made of NbN on a sapphire substrate with a further MgO layer [63, 64]. GaAs [65], quartz [66] and $LiNbO_3$ [67] were later demonstrated as valid substrates. Although outstanding in terms of photo-responsive properties [68], NbN films suffer a meaningful limitation for having a crystalline lattice. This may give rise to constrictions in fabrication during the film deposition over substrates with different lattices or encapsulation with further layers for similar mismatch issues, generally lowering the critical current of the device. For this reason, NbTiN, which is a poly-crystalline material, shows better compatibility with a wider range of substrates. Like NbN, NbTiN is mechanically robust against repeated/gradual temperature variations and is chemically inert to materials used in conventional electron-beam lithography. The bulk critical temperature of NbTiN films is around 14 K. The gap voltage is about 5.2 meV [69], at least two orders of magnitude lower than typical photon energies, which makes it sensitive over a wide range of wavelengths of the electromagnetic spectrum, from visible to mid-IR. Other amorphous superconducting materials are successfully used for sensing. WSi SNSPDs achieved a 93% SDE due to the low energy gap of its material [70]. MoSi [71], MoGe [72] are also emerging as promising alternatives. Such compounds are all amorphous materials hence superconducting at temperatures lower than NbN and NbTiN due to their bandgap (see Eq. 3).

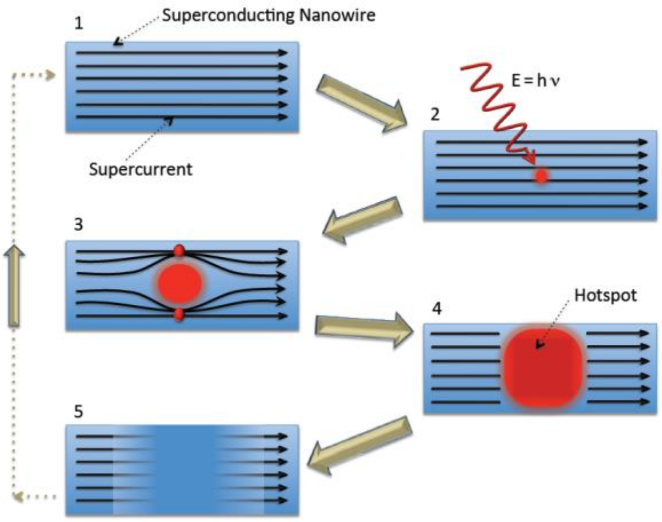

Fig. 2.19: Schematic of the operating principle of the SNSPD: (1) the nanowire is maintained in its superconducting state (blue), below its critical temperature and DC biased just below its critical current. (2) When a photon is absorbed by the nanowire, the photon generates a hotspot (red) causing the nanowire to lose the superconducting state in that region, (3) which in turn forces the supercurrent to bypass the hotspot. Since the nanowires are narrow, the local current density around the hotspot increases exceeding the superconducting critical current density. (4) This results in a resistive barrier across the width of the nanowire. Joule heating aids the growth of large normal region and thus a measurable output voltage pulse. (5) The current flow is interrupted, reducing the heating while the hotspot reaches a thermal equilibrium with the substrate and the nanowire recovers its superconducting state.

Photo-detection is achieved after cooling down the SNSPD below its critical temperature. At the same time, a DC bias lower than the critical current is applied to the nanowire (Fig. 2.19/1). As a single photon gets absorbed in one of the nanowires (Fig 2.19/2), its energy is transferred to the Coopers pairs. A proportion of the Cooper pairs are broken up into quasi-particles forming a growing spot (Fig 2.19/3), called resistive region, that covers the entire cross-sectional area of the nanowire (Fig 2.19/4). The presence of the resistive region in the nanowire diverts the bias current to an external impedance load, generating an electric photo-response. The reduction in current flow reduces the Joule heating in the SNSPD (Fig 2.19/5) supported by the substrate that works as a heat sink; on cooling, the superconducting state is restored and current comes back to flow in the SNSPD (Fig 2.19/1), now ready for another single photon detection.

In practice, an SNSPD is realized as a meander structure because optical beams from infrared light-sources cannot be focused onto a 100 nm-wide nanowire.

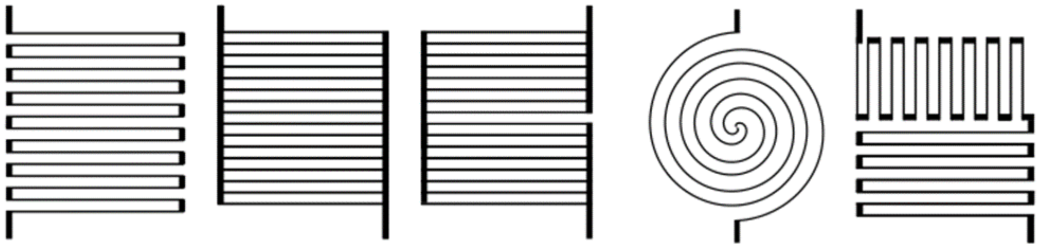

Fig. 2.20: SNSPD nanowire patterns. From left to right: meander [24], parallel nanowire [73], parallel nanowires in series [74], spiral and perpendicular meander SNSPDs [75].

Different patterning techniques are reported in literature to overcome the problem (Fig. 2.20). The goal is an extension of the sensitive area[4], in order to improve the optical coupling.

As the nanowire length increases, fabrication yield statistically decreases. Such constrictions in the nanowire do not permit high bias for the SNSPDs whose efficiency is therefore limited [76]. Shorter nanowires possess better intrinsic quantum efficiency due to their superior uniformity. Moreover, shorter nanowires have low kinetic inductance L_k, offering a shorter dead time. This makes shorter nanowires suitable for applications in which high-speed is more important than high efficiency. SNSPDs intrinsically have significant inductance due to their geometry. The inductance consists of a magnetic part and a kinetic part. The former is caused by the magnetic energy stored due to the magnetic field in the dielectric and depends only on the geometry of the sample (see Eq. 6). The load impedance can also be increased to obtain low dead times. However, as the dead time is reduced below a certain threshold, the returning current in the nanowire does not allow the hotspot to disappear completely due to Joule heating. This results in a self-heating hotspot [62]. The consequences after such self-heating is a nanowire switched into a locked normal state, forbidding further detection of photons.

As for lumped elements, the parallel network of two inductors is electrically equal to a single smaller inductor, parallel nanowires configurations can reduce the L_k. In practice, the design of an array of SNSPDs is an intrinsic requirement for such detectors. Apart from applications involving a huge number of pixels, it is always convenient to divide the active area into few independent pixels rather than having a

---

[4] Usually up to 30 x 30 μm^2 with a 50% filling factor.

single large-area but slow detector; in this way, a setup may still sense photons while part of the sensor is recovering from another detection.

An immediate way to enhance the optical performances of a detector is the SNSPD-integration with optical layers [2] (Fig. 2.21). Anti-reflection coatings can consistently reduce losses due to photo-reflection at the interface between the light source and the substrate. Optical cavities, instead, re-direct photons losses in transmission toward the sensitive area of the detector. In few words, an optical cavity is formed by an insulator (whose thickness is typically a quarter-wavelength of the testing light-source [77]) surrounding the nanowires with a metal mirror on top.

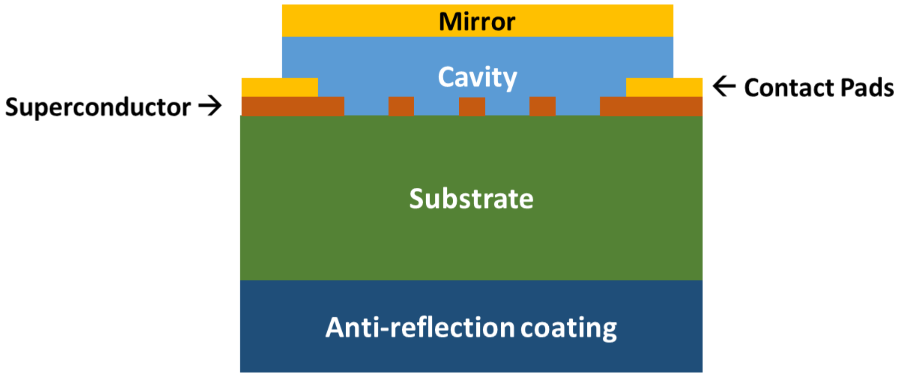

Fig. 2.21: Graphic illustration of an SNSPD integrated among an anti-reflection coating and an optical cavity.

A different approach in SNSPDs fabrication consists in the integration of a nanowire with a waveguide [78]. Such solution overcome scalability issues if different SNSPD-geometries are in the same photonic system [79]. In this design (Fig. 2.22), photons are absorbed by evanescent coupling to the superconducting nanowire fabricated on top of an optical waveguide. The implementation of a grating coupler can also maximize the photon flux generated from the light source toward the waveguide [80].

An interesting architecture was proposed and developed by Sahin *et al.* [81]: integrated on top of a GaAs waveguide, a NbN meander is transformed into a 4-element SNSPD in series, by placing four 38 Ω resistors in parallel with each SNSPD. Such devices exhibited PNR properties.

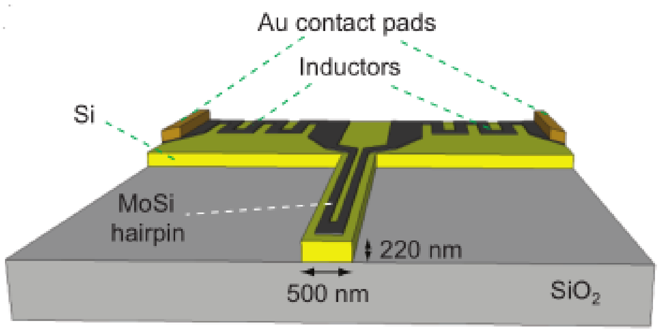

Fig. 2.22: Sketch of a single-mode Si-waveguide integrated (with a MoSi SNSPD on top) and complementary circuitry (Au contact pads, inductors). Courtesy of Dr. Robert Kirkwood.

2.4.7 Multiplexing schemes for SNSPDs

Only in recent times multiplexed SNSPDs arrays emerged. Most of the configurations adopted in other superconducting detectors cannot be adopted in SNSPD multiplexing. For instance, the response time of SQUID signals is much longer than the original response time of the SNSPD pulses [82] and coupling between transmission lines and SNSPDs are still under investigation. SNSPDs do not detect photons via resonances hence implementing an AC bias like MKIDs needs a careful setup.

Zhao *et al*. [83] proposed a multiplexing scheme for 4 pixels, with an active area of 2.6 x 3.0 μm^2, based on a double output. If one pixel triggers, the current biased through that pixel is split to the two outputs addressed to a differential amplifier. Sign and amplitude of the resulting signal uniquely indicate the fired pixel.

Verma *et al*. [84] investigated a scalable readout scheme for an array of SNSPDs that yields both temporal and spatial information about the detection event. For an *N* x *N* array, the scheme requires:

- 2*N* coaxial cables
- A resistor in series with each SNSPD
- *N* readout resistors (one per row)
- *N* bias sources + *N* bias-tees (one per column)

The multiplexer was demonstrated for 4 pixels, considered as a matrix of 2 rows and 2 columns. If a pixel is involved in a photo-detection, its column and its row switch to an open-circuit condition. The current coming from the bias is therefore diverted to the readout resistor of the row, producing a pulse. Such pulse will be observed only on the voltage outputs for the column and the row of the triggered pixel, providing a full spatial identification.

Yamashita *et al*. [85] reported a linear 4-pixel array multiplexed by single-flux quantum (SFQ) logic electronics [86]. The main advantage consists in a reduced number of coaxial cables, meaning a reduction of the associated heat load. In brief, the SNSPDs output currents are converted into quantized and picosecond-long pulses, i.e. SFQ signals. The array is time-resolved on behalf of different cable-lengths between pixels and SFQ circuits.

Hofherr *et al*. [73] presented a time-tagged linear array, in order to recover the origin of pulse events. A patterned superconducting delay line is placed between the elements of an SNSPDs chain. This concept enables a low cryogenic system complexity and a single bias line to supply all detector elements, because of their sequenced order. Moreover, only one readout line is required in this scheme. The principle of operation is derived from the basic detection mechanism model. As the hot-spot resistance is significantly larger than the impedance of the readout line, the bias current collapses in the detector path and increases in the parallel readout path producing a voltage pulse at the impedance of the readout. The pulse events generated by the detector elements are individually delayed on the readout line. To evaluate the time signature of each detector, a TCSPC module is used, meaning that time-tagged concept only works for applications where the temporal width of the effect under investigation is shorter than the detector delay.

In *Chapter 4*, two alternative readout schemes will be investigated.

2.5 Single-photon sensing applications

2.5.1 Applications for infrared photon counting arrays

Ground-to-space communications: The demand for high data rate transmissions from space-borne observation platforms progressively extended the distance of terminals in free-space optical communications [87]. Indeed, an optical link offers several advantages compared to traditional radio-frequency (RF) setups. Diffraction losses in RF links are much higher[5] than diffraction losses in optical setup, because optical wavelengths are three/four orders of magnitude shorter than RF

---

[5] At least six orders of magnitude

wavelengths. Thus, for a given data-rate, optical terminals can be smaller and require less power than RF terminals.

The high-directivity of optical signals also minimizes interferences between transmitters, in contrast to the well-known band consumption in RF systems. A ground-to-space communication experiment (Fig. 2.23) involves at least one ground station, containing an optical receiver, a satellite, containing an optical transceiver, and a satellite remote control station (on earth). The reason why the receiver is sent into space is related to a more efficient temperature control in an environment where temperature is sensibly lower than Earth [88]. In this way, relevant wavelength-drifts of the laser source can be avoided. The communication is a mono-directional transmission of laser pulses, while the sensing setup is often SPD based. The transmitted signal from space is strongly attenuated during its path and the arrival intensities are so low that a photon counting receiver is required.

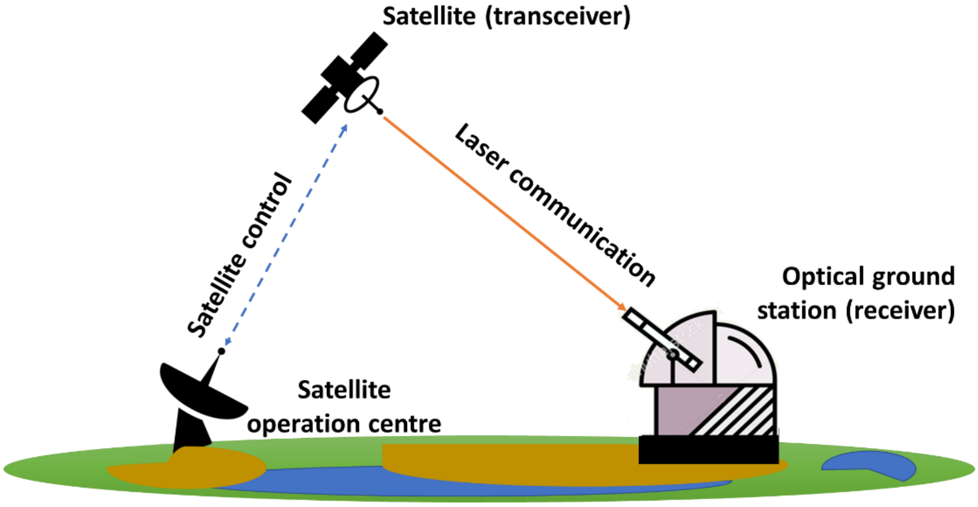

Fig. 2.23: Graphic illustration of a ground to space communication setup. A satellite is remotely controlled on earth and sends a light beam toward an optical ground station.

A milestone in ground-to-space communications is represented by the “Lunar Laser Communication Demonstration” [89], a NASA project able to operate a 622 Mbps data rate between a space terminal on the lunar atmosphere and an Earth ground station, separated by ~360.000 km. The successor to this project is DSOC (Deep Space Optical Communications). The goal is to transmit data back from a probe sent to an asteroid in the Kuiper belt.

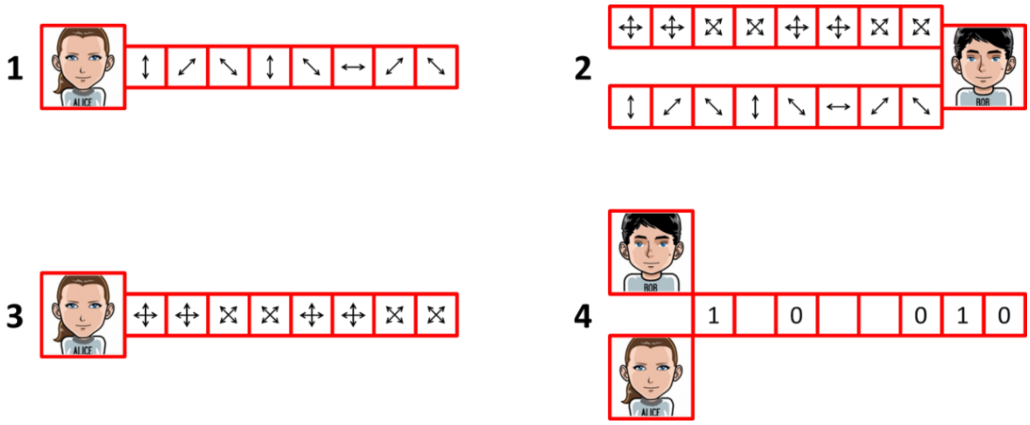

Fig. 2.24: Quantum Key Distribution phases. 1) The secure communication starts when Alice sends a random bit (0 or 1) to Bob in the form of polarised photons over a quantum channel from the four chosen states {45°, 90°, 135° and 180°}. 2) Bob randomly uses a rectilinear {180°, 90°} or diagonal {45°, 135°} polarizing filters to detect the polarization of the photons. 3) Over a classical and unsecured channel, Alice repeats Bob's choice of polarization filters used for different photons. 4) Both apply a sifting procedure, discarding the information related to Bob's wrong choice of polarisation filters (50% of the information, on average). The remaining photons are translated into the binary code (0/1) based on the predefined logic. Then, Bob and Alice reveal the actual information content for a set of bits, to attest the security of the quantum channel.

In recent times, ground-to-space experiments were performed adopting a quantum communication protocol called Quantum Key Distribution (QKD). It is an advanced method of cryptography [90, 91], in which quantum states (quantum bits) are utilized to create an encoding/decoding key. An information sender and a receiver (historically called Alice and Bob, respectively) follow the protocol (Fig. 2.24) using photons supported by a first quantum channel to distribute keys and a second classical channel to verify security and subsequently exchange encrypted data. Polarization or phase of the photons can be used to represent each conjugate state of the quantum system. Unfortunately, technology for single-photon sources is not so advanced, affecting communication distance, clock rate and security related to multi-photon states. Therefore, some corrections to the original protocol were investigated [92-95].

The performance of free-space QKD systems have been already optimized to achieve secure communications over large distances [96]. A telescope in a Low-Earth-Orbit satellite, located 1600 km far from the ground, acted as a source of entangled photons, transmitting the two beams to two separated ground based receivers.

A very recent experiment proved QKD inter-satellite communications using entangled photons [97].

Single-photon LIDAR: it is a remote sensing technique (Light Detection And Ranging), among the first applications after the invention of the laser [98]. The main benefit in LIDAR systems is they can map a wide range of materials independently from the used light source (i.e. UV, visible or IR) with high spatial resolution. Indeed, LIDAR systems monitored agriculture and flora health, archaeological sites, transport vehicles and spaceflight, meteorology, mines and soils, ecosystems and biosphere.

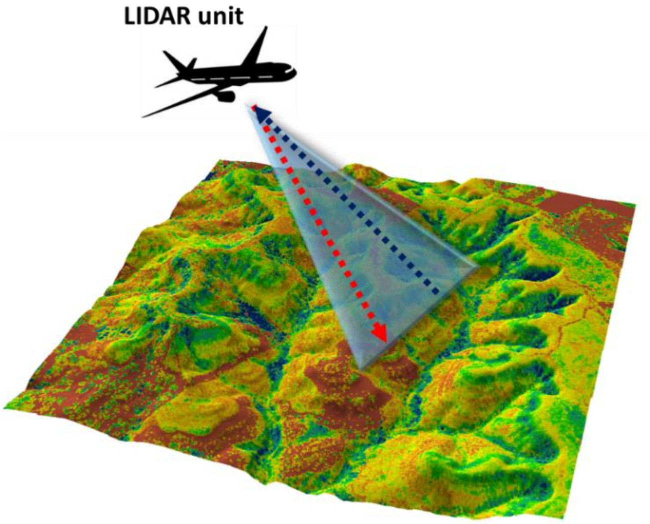

Fig. 2.25: Graphic illustration of LIDAR scanning. A LIDAR transceiver unit illuminates a surface under investigation and collects the returning photons.

In the technical literature, LIDAR systems are classified as active systems because they emit pulses of light (i.e. the laser beams) and detect the reflected light. The basic idea is a simple measurement, in time and intensity, of a laser pulse striking an object and returning to a sensor (LIDAR unit) whose position is known (the so-called time-of-flight). A scan that uses pulses send at different angles, can provide a map of the surface under test (Fig 2.25). Generally, the time data indicates the elevation of the target while the intensity data indicates of the composition of the target. Of course, the narrower the laser beam, the higher the lateral spatial resolution of the map.

Single-photon detectors and TCSPC electronics may provide a remarkable advantage for LIDAR: the system can work until there is one photon return-event per pulse, extending the distance of the targets under test, for a prefixed laser repetition rate

(RR). In order to get position information on the photon detected, it is required that only one laser pulse may return at once. For l the maximum distance of the surface under test, n the effective refractive index of the medium and c the speed of the light, the relationship is thus the following [99]:

$$l = \frac{c}{RR \cdot 2n} \quad \text{(Eq. 7).}$$

Compared to other LIDAR techniques (employing CCD/CMOS[6] cameras, for instance), single-photon LIDAR has the disadvantage of performing only 2-dimensional maps: for a given scanning angle, the backscattering due to the closest object is the only one detected by the single-photon sensor. Conversely, multiple return systems can capture up to five returns per pulse (Fig. 2.26) and it increases the ability to look at the 3-dimensional structure of the features above the ground surface.

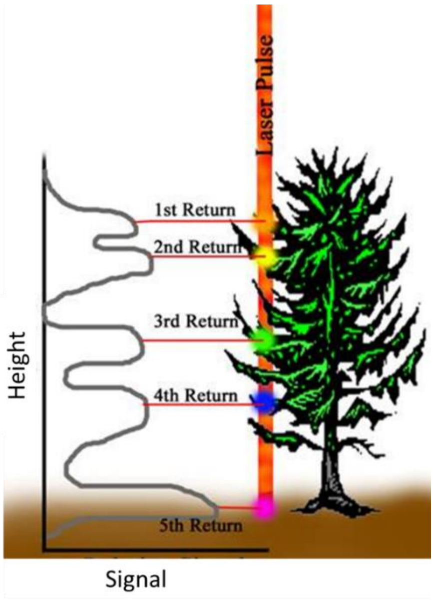

Fig. 2.26: Multiple return signals in LIDAR. A Laser pulse crosses few items and is backscattered at different heights, resulting in a more detailed mapping.

In literature, for a target distance of ~300 m, millimetric depth resolution was achieved by different single-photon systems in which the laser pulse-width was less than 100 ps [100].

An important emerging market for LIDAR systems are the autonomous driving vehicles [101].

---

[6] CCD: Charge-coupled device; CMOS: Complementary metal-oxide semiconductor

2.5.2 Single-photon spectroscopy

Spectroscopy is the study of the interaction between photons and matter. Every single type of atom and molecule have unique spectra. Hence, these spectra can be used to collect information about the matter under test. Spectroscopic analysis is also frequent in astronomy and remote sensing on earth. Most research telescopes have optical spectrometers, scientific instruments that sense light's intensity and polarization over a specific region of the electromagnetic spectrum. The measured spectra are used to determine the chemical composition and physical properties of astronomical objects (e.g. temperature and velocity).

A spectrometer including a single-photon source and an SPD would have the finest resolution. On the detection side, the isolation of an ultra-weak signal, compared to residual background fluorescence and detector noise was already overcome [102]. On the emission side, the lack of reliable single-photon sources, combined with the difficulty to achieve very efficient emitter-photon interfaces [103], made the investigations challenging. Moreover, spectrographic measurements demand a tuning of the frequency of the single-photon source with respect to the transition in the matter under test.

In a state-of-the-art free-space single-photon spectrometer [104], based on APDs, some features get adopted to solve the issue. When the ratio of the spectral linewidths before and after the transition is close to unity, the extinction cross section[7] of a single 2-level emitter can approximated as $\lambda^2/2$, where λ is the wavelength of the source. $\lambda^2/2$ is comparable to the area of a focused beam in high numerical aperture collection optics. A continuous wave (CW) tuneable dye laser generates a beam that hits a dichroic mirror. Passing through a combination of aspheric and solid-immersion lenses for achieving a high numerical aperture in collection and excitation, the output is driven toward the source sample. Such sample is tuned in frequency by a voltage applied via interdigitated micro-electrodes. The outcoming beam and a second CW dye laser-beam are coupled via a beam combiner. The transmitted optical signal is divided across a Hanbury Brown–

---

[7] Area that, when multiplied by the irradiance of electromagnetic waves incident on an object, gives the total radiant flux scattered and absorbed by the object.

Twiss correlator[8] and to a polarization-maintaining single-mode fibre-coupled beam splitter which is connected on one port to a third APD, to probe the light in the fibre. On the other port, the last splitter is connected to a half-wave plate that aligns the polarization of the single-photon stream with the transition dipole moment of the target molecule. A gold mirror deposited on the back of the target sample reflects the extinction of the incident beam, which is recorded by a forth APD.

Another approach [105] to single-photon spectroscopy involves the use of group velocity dispersion (GVD) in optical fibre [106]. This parameter is much higher (in absolute value) in dispersion compensating fibres (DCFs) to stretch ultrafast pulses. In this way, a single detector collects all possible arrival times associated to different spectral components. The light source of the setup generates photon pairs at 1544 nm (signal) and 1517 nm (idler), guided and coupled (with 25% efficiency) into the DCF which is not polarization-maintaining. To recover the polarization, the outcoming beam travels through a quarter- waveplate, a half-waveplate and finally a polarization beam splitter, separating signal and idler which are detected by two APDs. The GVD computation derives from the collection of the time delay between the laser trigger and the electronic response from the APD with a time-to-digital converter. The technique is affected by a couple of downsides. First, a calibration setup is required; a reference spectrometer must be employed to acquire the travel time through the DCF for a set of wavelengths. By relating the peaks from the reference spectrum with the temporal peaks from the time measurement, a calibration curve is obtained to reconstruct the entire set of spectra. Moreover, the polarization rotation caused by the DCF is wavelength dependent. It means an imperfect reconstruction of the original linear polarization and thus, for the entire spectrum, the signal/idler split have an intrinsic uncertainty (quantified, by the authors, in an 80% polarization contrast for both signal and idler beams).

2.5.3 Fibre optic sensing: moving into the single photon regime

A distributed fibre-optic sensor is expected to reveal temperature, strain and vibration information from a set of points along an optical fibre through light scattering. In industrial applications, they are an attractive alternative to multiplexed

---

[8] An intensity interferometer that uses two detectors to measure the correlation of a light source after a beam splitter.

point sensors, because a single fibre-optic cable can potentially replace thousands of individual sensors, dramatically simplifying sensor installation and readout, reducing as well infrastructure costs.

When a light-wave is launched into an optical fibre, photons will be redistributed by various phenomena. If one of the above-mentioned parameters (i.e. temperature, strain and vibration) changes along the fibre, the scattered signal will be altered by Raman, Rayleigh scattering and Brillouin scattering mechanisms. Distributed fibre sensors can be developed based on monitoring the changes on the modulated signal. Such changes may be collected measuring, for a given wavelength, the time of flight of the amount photons from different portions of fibre (Optical Time-Domain Reflectometry, OTDR); its first application was to check attenuation in fibres, for cable diagnostic in telecom systems [107]. The other technique involves a tuneable laser scanning the fibre under test over a range of frequencies $\Delta\nu$ (Optical Frequency-Domain Reflectometry, OFDR) later converted through Fourier Transform. OFDR systems are appreciated for their spatial resolution SR = ${}^{c}/_{\Delta\nu \cdot 2n}$ that may reach a sub-millimetre order by increasing the frequency scanning range. However, the maximum length monitored is limited by the coherence length of the laser sources and the different state of polarization along the fibre [108]. In practice, OFDR systems are not reliable after few dozens of metres. In OTDR systems, the SR for a given fibre is basically proportional to the pulse width τ of the light source (i.e.: $c \cdot \tau/2n$).

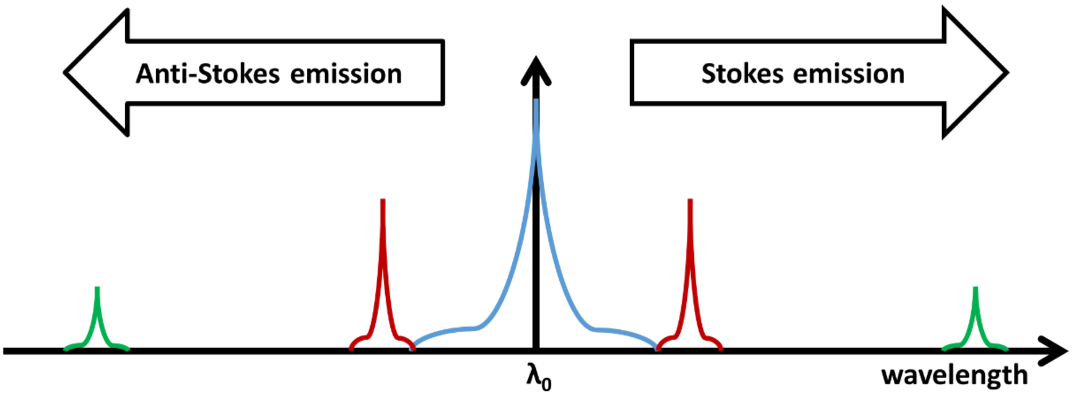

Fig. 2.27: Graphic examples of Rayleigh (blue line), Brillouin (red line), and Raman (green line) scattering peaks relative to the wavelength of the input light signal λ_0.

OTDR sensors may be based on Rayleigh [109], Brillouin [110] and Raman [111] scattering (Fig. 2.27). In all the cases, the energy of the incident light-wave is supposed to be lower than the interatomic bonds of the propagation medium, i.e. the fibre-core.

Rayleigh scattering: The most dominant interaction between light and molecule produces elastic scattering of photons and therefore no change happens on the molecular energy state. The energy of an incident photon is absorbed by the molecule and produces random thermal fluctuations due to density, composition and orientation of molecules within the transmitting medium. However, the lack of energy to reach an equilibrium at higher energy states produces a reemission of the entire incoming energy, i.e. a photon at the same frequency, whereas the molecule return to its original energy state, the so-called ground state.

Even if Rayleigh-scattering based detectors could measure temperatures, they are not common in real world applications for several reasons. The Rayleigh signal is quite weak and usually needs for high-power lasers and long acquisition times. In fact, good temperature sensitivity (± 1 K) with a spatial resolution of 1 m along a 100 m fibre under test was achieved only in liquid-core fibres[9] [112]. In fibres, the backscattered signal decays exponentially. Nonuniformities of the attenuation coefficient in the fibre produce Rayleigh scattering losses and locally deviate the signal from the exponential curve. In silica fibres, temperature and strains do not significantly modify the thermo-optic properties of the core, resulting in a constant attenuation coefficient and low temperature dependence. Hence, the quality of the measurements relies almost entirely in a temperature dependent core. In liquid-core fibres, the scattering loss coefficient of the liquid depends on the density fluctuations caused by thermodynamic molecular motion. Similarly, in doped glass fibres, variations in the attenuation coefficient are enhanced respectively by transitions between electronic levels in the dopant that are temperature dependant. The best results achieved are a 1 K uncertainty and a 3.5 m spatial resolution over a 200 m fibre under test Ho-doped.

---

[9] A silica glass tube filled with a higher-refractive index low absorption liquid.

Advanced schemes for Rayleigh OTDR were proposed in the last decades. Using a broadband laser to create a polarized pulse of light, Polarization OTDR exploits the possibility to read at the same time, along single-mode fibres, the backscattered wave in terms of intensity and polarization information [113]. This double profiling on the fibre gives a qualitative indication of the perturbations on the fibre[10]. Although Polarization OTDR allows Rayleigh-based setups to sense strains [114], polarization changes are induced by several factors, some of them not under control. That results in very noisy measurements.

Coherent Rayleigh scattering detection is less affected by DC noise than Polarization OTDR Rayleigh scattering. Coherent detection means that a reference signal (the light source, typically) and the backscattered signal get optically correlated.

Brillouin scattering: At the macroscopic level, the matter is neutral; positive and negative charges have a continuous equilibrium. Conversely, at the microscopic level there is an electronic cloud shared by neighbouring molecules in a perpetual cycle; then, a prefixed intermolecular distance preserves the global stability. A mismatch for such distance implies an energy redistribution represented by a wave of quasiparticles like phonons, polarons (in dielectrics) and magnons (in magnetic materials). A Brillouin based fibre sensor measures the light scattered from the collective phonon oscillations in silica fibres. More properly, it is a form of Stimulated Brillouin Scattering because a laser pump provides a light beam at a wavelength resonating with an acoustic wave in the fibre-core. Such resonance produced outcoming photons shifted of the order of hundreds of MHz with respect to the pump. Brillouin systems were demonstrated both for temperature extraction [115] and strain evaluation [116]. Combined OTDR sensors were proposed [117], achieving accuracy of 4 K and spatial resolution of 40 m over a 1200 m long fibre under test in an acquisition time of the order of one hour. The main downside in Brillouin based setups is that a change in the strain distribution is indistinguishable from a change in the temperature distribution. This cross-sensitivity could be in part corrected if the spontaneous emission and Brillouin frequency shift are measured simultaneously [118]. Hybrid systems, like the Landau–Placzek ratio-based technique [119] were

---

[10] E.g. a temperature variation mostly affects the intensity while a pressure on the fibre affects intensity and polarization of the backscattered photons.

experimentally demonstrated. Here, a laser pulse is sent through an optical fibre; both the backscattered spontaneous Brillouin and Rayleigh signals are extracted from the fibre under test, spectrally separated by an optical filter, photo-detected and processed. The Landau-Placzek ratio relates the heat capacity ratio[11] (γ) with the integrated Rayleigh (I_R) and Brillouin (I_B) intensities:

$$\frac{I_R}{2I_B} = \gamma - 1 \qquad \text{(Eq. 8).}$$

The Rayleigh backscattering fluctuations act like a noise (Coherent Rayleigh Noise) for the Brillouin signal. It depends on interference between several photons backscattered at different positions in the fibre causing phase-intensity noise conversion. As it is not related to the physical state of the fibre nor the light source, Coherent Rayleigh Noise cannot be reduced by signal averaging or longer acquisition times. The impact of the noise on the signal was formally studied [120] and it is proportional to the square root of a factor computed dividing the pulse width by the refractive index of the fibre and the laser bandwidth. To give an idea, such setups can show temperature and spatial resolution of 10 K and tens of metres, respectively. The main reason is the weakness of the spontaneous Brillouin emission. Although SPDs may offer an adequate solution to pure Brillouin backscattering, the simultaneous presence of Coherent Rayleigh Noise generates a too high *SNR*.

Fibre Bragg gratings: A distributed Bragg reflector is a multi-layer structure in which the effective refractive index shows a periodic variation in the fibre. In optical fibres, such feature is possible by modifying with a certain periodicity sections in the fibre-core, to achieve a variation in refractive index. As result, Fibre Bragg Gratings (FBGs) behave like optical notches/dielectric mirrors: a set of wavelengths are reflected while the remaining spectrum can propagate. Several grating types were proposed in literature [121]. Additionally, it is possible to demonstrate how temperature and strain variations [122] shift the Bragg grating centre. Simultaneous detections were also performed [123]. The wavelength shift $\Delta\lambda$ is proportional to the central reflected wavelength λ_r, the temperature shift ΔT and the sum of the thermal expansion coefficient α_Λ and thermo-optic coefficient α_n [124]:

---

[11] It is the heat capacity at constant pressure divided by heat capacity at constant volume

$$\Delta\lambda = \lambda_r(\alpha_\Lambda + \alpha_n)\Delta T \qquad \text{(Eq. 9).}$$

Unfortunately, like the Brillouin effect-based setups, a clear separation between temperature and strain influences is not possible because both shift λ_B. Various arrangements aimed at separating such interference were offered. These include the use of a second grating element contained within a different material and placed in series with the first grating element [125] and the use of a pair of fibre gratings surface-mounted on opposite surfaces of a bent mechanical structure [126]. Nevertheless, the previous techniques have limitations when it is required to interrogate the wavelength of a large amount of fibre gratings. Other methods consist in measuring two different wavelengths, two different optical or grating modes [127]. In another scheme (Fig. 2.28), two superimposed gratings with different λ_r (850 nm and 1300 nm) were used to extract simultaneously strain and temperature (Fig). A two-wavelength shift leads to a matrix relationship:

$$\begin{bmatrix} \Delta\lambda_{r1} \\ \Delta\lambda_{r2} \end{bmatrix} = \begin{bmatrix} \Psi_{1\epsilon} & \Psi_{1T} \\ \Psi_{2\varepsilon} & \Psi_{2T} \end{bmatrix} \begin{bmatrix} \Delta\varepsilon \\ \Delta T \end{bmatrix} \qquad \text{(Eq. 10).}$$

Known the permittivity mismatch $\Delta\varepsilon$, the elements of the Ψ matrix can be determined experimentally via a separate calibration of the λ_r changes with strain and temperature. Once known, strain and temperature information can be extracted by inverting the Ψ matrix.

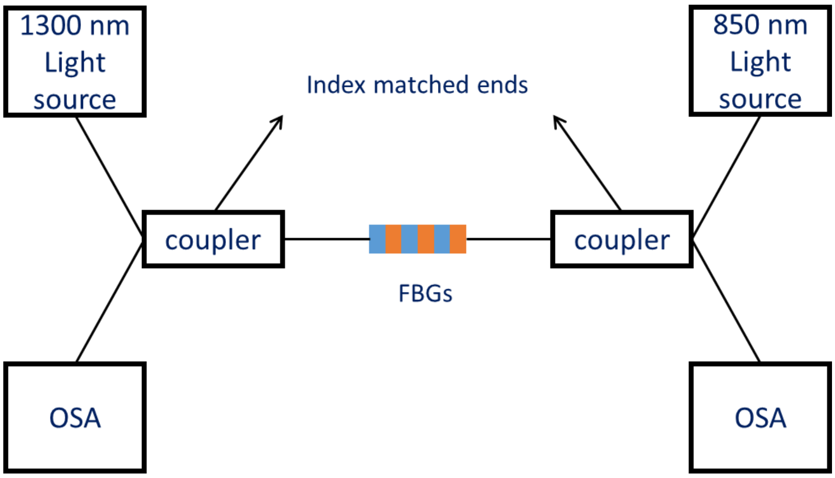

Fig. 2.28: Scheme for simultaneous measurements of strain and temperature using Fibre Bragg Gratings (FBGs). OSA: Optical Spectrum Analyzer.

In no case, anyway, FBGs can perform absolute thermometry. The reason should be obvious comparing FBGs with the technologies above mentioned. In FBGs there is no ratio of two signals generated by the same phenomenon. Therefore, precise knowledge of the setup parameters is essential. Finally, the readout terminals for FBGs are Optical Spectrum Analysers (OSA). Commercially available OSAs are based on traditional photodiodes hence single-photon experiments are not compatible with FBGs.

Raman effect: Although predicted theoretically by Adolf Smekal in 1923, the inelastic scattering of light was first experimentally demonstrated five years later by C.V. Raman and K.S. Krishnan, who were awarded the Nobel prize in 1930.

In the case of inelastic scattering, the interaction of a photon with molecules produce molecular vibrations in first-order neighbouring atoms and a frequency shift between the incoming and returning photon. A molecular vibration is a periodic motion of the atoms in a molecule while the same molecule, seen as a closed system, has a constant roto-translational motion. Before the arrival of any photon, the molecule is supposed to stay in its ground state. The energy of an absorbed photon lets the molecule reach higher virtual energy states (virtual because not observable and due to short lifetime). At these higher states, three scenarios are possible:

- As previously mentioned, the first (dominant) effect is the elastic (Rayleigh) scattering.
- The second effect (approximatively 1 in 10 million photons) occurs when the molecule relaxes on an excited vibrational state, higher than the equilibrium state, and therefore releases a photon whose energy is lower than the incoming one (Stokes[12] scattering).
- The third effect, with a lower probability than Stokes scattering, is the anti-Stokes scattering. Here, the molecule relaxes on an energy state lower than the equilibrium state and consequently emits a photon at higher energy than the incoming one.

---

[12] In honour to G. Stokes, who showed in 1852 that fluorescence is due to light emission at longer wavelength than the absorbed incident light.

Stokes and anti-Stokes shifts are of the order of THz and their intensities are a fourth order function of their wavelength [128]:

$$\frac{I_{AS}}{I_S} = \left(\frac{\lambda_S}{\lambda_{AS}}\right)^4 e^{-\hbar\omega/k_B T} \qquad \text{(Eq. 11).}$$

Raman scattering appears like a form of fluorescence, but they are distinct phenomena. In fluorescence, a photon gets absorbed only if its energy is resonant with real molecular transitions after the ionization of the atomic electrons. In Raman scattering, photons perturb phonon modes, whatever is the frequency.

Nonetheless, fluorescence has characteristic lifetime of nanoseconds whereas Raman effect is a scattering, i.e. instantaneous. Raman effect also differs from Brillouin scattering only for the order of magnitude of the shift. But Raman scattering is a local effect while in Brillouin scattering emitted photons derive from a large scale and low frequency phonon vibrations and no transition in atomic bonds occurs.

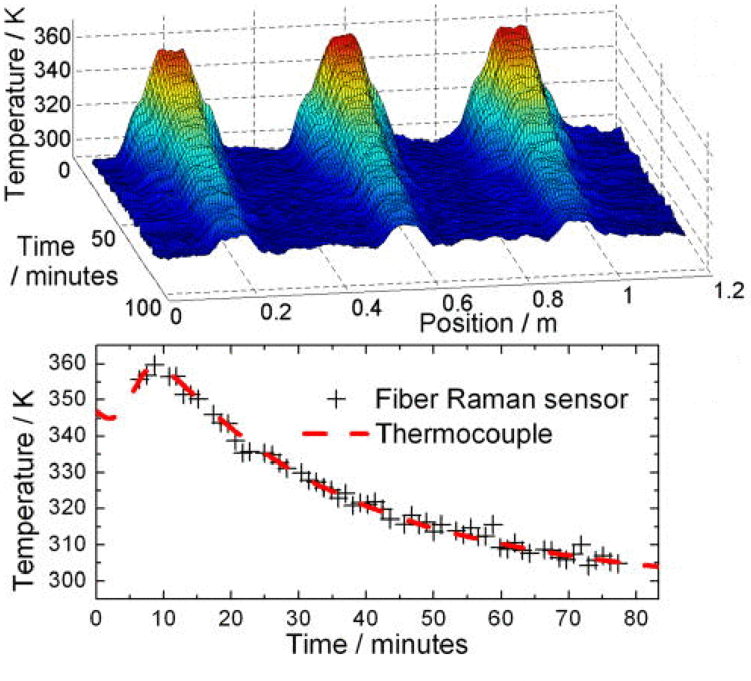

Fig. 2.29: Plots of the measured temperature as function of the time and the position in a fibre (upper), later compared with a reference thermometer (lower). Reproduced from [131].

To date, the Raman-based sensor is the most commercially successful fibre-temperature technology[13]. Combined with SNSPD technology, OTDR systems have

---

[13] York Sensors Ltd, DTS 800 system

already accomplished long-distance (200 km) and high-resolution (0.1 km) performances [129].

Non-gated up-conversion APDs were also successfully employed for OTDR testbeds [130]. Stokes and anti-Stokes emissions, measured on the single-photon level may be used to achieve a calibration-free thermometer (Fig. 2.29). Experimental demonstrations were performed employing different single-photon technologies like PMTs [128], and SNSPDs using different kinds of fibres, such as silica fibre [131] and chalcogenide fibre [132].

The intensity of the emission for each band can be approximated as follows [133]:

$$I_u = \eta_u \Delta f_u P_o l \left| g_{R,u} \right| N(\omega_{u\_p}) D_c - B_u \qquad \text{(Eq.12).}$$

The subscript u is either S or a for Stokes or AS anti-Stokes, I is the back-scattered photon flux per second, η is the global efficiency of the optical path, Δf_u is the bandwidth of the Stokes or anti-Stokes filters, P_o is the peak pump power, l is fibre length, g_R is the Raman gain factor, D_c is the duty cycle of the pump signal, ω_{u_p} is the radial frequency detuning between the pump and the mean Stokes or anti-Stokes wavelengths, B represents the backscattered dark pulses and N is the phonons population as follows:

$$N = \begin{cases} \dfrac{1}{\exp\left(\hbar\left|\omega_{S\_p}\right| / k_B T\right) - 1}, & \omega_{u\_p} < 0 \\ \dfrac{1}{\exp\left(\hbar\left|\omega_{AS\_p}\right| / k_B T\right) - 1} + 1, & \omega_{u\_p} \geq 0 \end{cases} \qquad \text{(Eq. 13).}$$

Detuning ω_{u_p} as constant over the filter bandwidths and assuming $\omega_{S\_p} \approx \omega_{AS\_p}$, the ratio of Stokes to anti-Stokes is given by:

$$\frac{I_S(x) - B_S}{I_{AS}(x) - B_{AS}} = \frac{\eta_S \Delta f_S \left| g_{R,S} \right|}{\eta_{AS} \Delta f_{AS} \left| g_{R,AS} \right|} e^{\hbar\left|\omega_{AS\_p}\right| / k_B T(x)} \qquad \text{(Eq. 14).}$$

Rewriting the detuning shift in frequency (F) rather in its radial value, grouping all the constants in c and applying the natural logarithm, an explicit relationship between temperatures and photo-intensities is finally established:

$$k_B T(x) = h\left|F_{AS\_p}\right| \Big/ ln\left(\frac{I_S(x) - B_S}{c\left[I_{AS}(x) - B_{AS}\right]}\right) \qquad \text{(Eq. 15).}$$

2.5.4 Fibre temperature sensing for geothermal applications

Geothermal energy [134] is considered a high-risk engineering project. Costs for the exploration of boreholes and maintenance of geothermal plants are extremely high. Risk mitigation is therefore crucial, considering the uncertainty of the amount of recoverable reserves and production capabilities nearby to be drilled. Geo-thermometric surveys indicate the level of resources in a borehole.

Two major techniques are well established in geo-thermometry. The first one consists in the extraction of geothermal brine (a mixture of saline water and vapours) later examined in chemical laboratories [135, 136]. This method is very expensive because the collection of multiple brine samples requires several drills. Furthermore, laboratory tests on brine may have a time-scale of days or even weeks. The second method is *in situ* temperature logging: an electronic thermocouple is placed at the end of a cable, progressively sensing the temperature at various depths of the borehole. Such setup, however, needs repeated calibration as a function of the explored depth. Nonetheless, if the temperatures in oil and gas wells do not compromise the integrity of the sensor, temperatures in high enthalpy geothermal boreholes can be of the order of 450 K. The most advanced logging setup for geothermal energy computation, at the time of writing, can perform a unique measurement up to 8 hours.

Fibre optic temperature sensors can play a strategic role in such risk mitigation. Indeed, owing to their flexibility and simplicity, distributed fibre optic temperature setups attracted a niche of civil engineers, in academia and in the geothermal industry; applications in hydrogeology, oil and gas surveys [137] and geothermal energy [138] have already emerged. In fact, an ideal fibre optic distributed thermometer, combined with the weakest signal sensitivity of SPDs, could sense dozens of points across hundreds of meters or even few kilometres in single measurement over an acquisition time comparable or quicker than the logging techniques.

2.5.5 Summary

While the most successful single photon technologies were developed for specific applications and the associated operational wavelengths, the SNSPDs offer broadband sensitivity and free-running operation, in order to characterize any photon-counting experiment operating across a broad spectrum.

This major advantage is balanced by a difficult scalability to large area and high pixel-density, due to the ultra-fast timing of the technology and the cryogenic setups required to readout the detectors. Anyway, a limited number of pixels is sufficient for several applications, historically performed with non-single photon sensors.

References

[1] Anant, V., Kerman, A. J., Dauler, E. A., Yang, J. K., Rosfjord, K. M., & Berggren, K. K. (2008). Optical properties of superconducting nanowire single-photon detectors. *Optics Express*, *16*(14), 10750-10761.

[2] Rosfjord, K. M., Yang, J. K., Dauler, E. A., Kerman, A. J., Anant, V., Voronov, B. M. *et al.* & Berggren, K. K. (2006). Nanowire single-photon detector with an integrated optical cavity and anti-reflection coating. *Optics express*, *14*(2), 527-534.

[3] Gerster, J., Kaiser, G., Reißig, L., Thürk, M., & Seidel, P. (1998). Low noise cold head of a four-valve pulse tube refrigerator. In Advances in Cryogenic engineering (pp. 2077-2084). Springer US.

[4] Haykin S., Communication systems, 4th ed. (J. Wiley and Sons, 2001).

[5] Silberhorn, C. (2007). Detecting quantum light. *Contemporary Physics*, *48*(3), 143-156.

[6] Divochiy, A., Marsili, F., Bitauld, D., Gaggero, A., Leoni, R., Mattioli, F. *et al.* & Gol'Tsman, G. (2008). Superconducting nanowire photon-number-resolving detector at telecommunication wavelengths. *Nature Photonics*, *2*(5), 302-306.

[7] Achilles, D., Silberhorn, C., Śliwa, C., Banaszek, K., & Walmsley, I. A. (2003). Fiber-assisted detection with photon number resolution. *Optics letters*, *28*(23), 2387-2389.

[8] Morton, G. A. (1949). Photomultipliers for scintillation counting. *RCA Rev.*, *10*.

[9] Hamamatsu Photonics, K. K. (2007). Photomultiplier tubes: Basics and applications. Edition 3a, 310.

[10] Hadfield, R. H. (2009). Single-photon detectors for optical quantum information applications. *Nature photonics*, *3*(12), 696-705.

[11] http://jp.hamamatsu.com/resources/products/etd/pdf/NIR-PMT_APPLI_TPMO1040E02.pdf

[12] Fukasawa, A., Haba, J., Kageyama, A., Nakazawa, H., & Suyama, M. (2008). High speed HPD for photon counting. *IEEE Transactions On Nuclear Science*, *55*(2), 758-762.

[13] Kume, H., Koyama, K., Nakatsugawa, K., Suzuki, S., & Fatlowitz, D. (1988). Ultrafast microchannel plate photomultipliers. *Applied optics*, *27*(6), 1170-1178.

[14] Oke, J. B. (1969). A Multi-Channel Photoelectric Spectrometer. Publications of the Astronomical Society of the Pacific, 11-22

[15] Beaver, E. A., & McIlwain, C. E. (1971). A digital multichannel photometer. Review of Scientific Instruments, 42(9), 1321-1324

[16] Washington, D., Guest, A. J., & Knapp, A. G. (1986). A Large-Area Electron Image Multiplier. Advances in Electronics and Electron Physics, 64, 101-110

[17] Comby, G., & Meunier, R. (1988). Test of a new 64-channel PMT for imaging. Nuclear Instruments and Methods in Physics Research Section A: Accelerators, Spectrometers, Detectors and Associated Equipment, 269(1), 246-260

[18] Shao, Y., Cherry, S. R., Siegel, S., Silverman, R. W., & Majewski, S. (1997). Evaluation of multi-channel PMTs for readout of scintillator arrays. Nuclear Instruments and Methods in Physics Research Section A: Accelerators, Spectrometers, Detectors and Associated Equipment, 390(1-2), 209-218.

[19] Popov, V., Majewski, S., & Welch, B. L. (2006). A novel readout concept for multianode photomultiplier tubes with pad matrix anode layout. Nuclear Instruments and Methods in Physics Research Section A: Accelerators, Spectrometers, Detectors and Associated Equipment, 567(1), 319-322

[20] Siegel, S., Silverman, R. W., Shao, Y., & Cherry, S. R. (1996). Simple charge division readouts for imaging scintillator arrays using a multi-channel PMT. IEEE Transactions on Nuclear Science, 43(3), 1634-164].

[21] Ribordy, G., Gautier, J. D., Zbinden, H., & Gisin, N. (1998). Performance of InGaAs/InP avalanche photodiodes as gated-mode photon counters. *Applied Optics*, *37*(12), 2272-2277.

[22] Rarity, J. G., Wall, T. E., Ridley, K. D., Owens, P. C., & Tapster, P. R. (2000). Single-photon counting for the 1300–1600-nm range by use of Peltier-cooled and passively quenched InGaAs avalanche photodiodes. *Applied Optics*, *39*(36), 6746-6753.

[23] Cova, S., Ghioni, M., Lotito, A., Rech, I., & Zappa, F. (2004). Evolution and prospects for single-photon avalanche diodes and quenching circuits. *Journal of modern optics*, *51*(9-10), 1267-1288.

[24] Brown, R. G., Jones, R., Rarity, J. G., & Ridley, K. D. (1987). Characterization of silicon avalanche photodiodes for photon correlation measurements. 2: Active quenching. *Applied Optics*, *26*(12), 2383-2389.

[25] Verevkin, A., Zhang, J., Sobolewski, R., Lipatov, A., Okunev, O., Chulkova, G. *et al.* & Semenov, A. (2002). Detection efficiency of large-active-area NbN single-photon superconducting detectors in the ultraviolet to near-infrared range. *Applied Physics Letters*, *80*(25), 4687-4689.

[26] Campbell, J. C., Dentai, A. G., Holden, W. S., & Kasper, B. L. (1983). High-performance avalanche photodiode with separate absorption 'grading'and multiplication regions. Electronics Letters, 19(20), 818-820.

[27] Sidhu, R., Chen, H., Duan, N., Karve, G. V., Campbell, J. C., & Holmes, A. L. (2004). GaAsSb resonant-cavity enhanced avalanche photodiode operating at 1.06 µm. *Electronics Letters*, *40*(20), 1296-1297.

[28] Kimukin, I., Biyikli, N., Butun, B., Aytur, O., Unlu, S. M., & Ozbay, E. (2002). InGaAs-based high-performance pin photodiodes. *IEEE Photonics Technology Letters*, *14*(3), 366-368.

[29] Rochas, A., Gosch, M., Serov, A., Besse, P. A., Popovic, R. S., Lasser, T., & Rigler, R. (2003). First fully integrated 2-D array of single-photon detectors in standard CMOS technology. IEEE Photonics Technology Letters, 15(7), 963-965

[30] Zappa, F., Tisa, S., Tosi, A., & Cova, S. (2007). Principles and features of single-photon avalanche diode arrays. Sensors and Actuators A: Physical, 140(1), 103-112

[31] Niclass, C., Sergio, M., & Charbon, E. (2006, October). A single photon avalanche diode array fabricated in 0.35-µm CMOS and based on an event-driven readout for TCSPC experiments. In Optics East 2006 (pp. 63720S-63720S). International Society for Optics and Photonics

[32] Zheng, L., Hu, H., Weng, Z., Yao, Q., Wu, J., & Sun, W. (2017). Compact Active Quenching Circuit for Single Photon Avalanche Diodes Arrays. Journal of Circuits, Systems and Computers, 1750149.

[33] Cominellia, A., Acconciaa, G., Peronioa, P., Recha, I., & Ghionia, M. (2017, January). Highly efficient readout integrated circuit for dense arrays of SPAD detectors in time-correlated measurements. In Proc. of SPIE Vol (Vol. 10111, pp. 101112N-1).

[34] https://www.princetonlightwave.com/wp-content/uploads/2017/03/PLI-Falcon-Updated.pdf

[34] Onnes, H. K. (1911). The superconductivity of mercury. *Comm. Phys. Lab. Univ. Leiden*, *122*, 124.

[35] Poole, C. K., Farach, H. A., & Creswick, R. J. (1999). *Handbook of superconductivity*. Academic press.

[36] Ginzburg, V. L. (2004). Nobel Lecture: On superconductivity and superfluidity (what I have and have not managed to do) as well as on the “physical minimum” at the beginning of the XXI century. *Reviews of Modern Physics*, *76*(3), 981.

[37] Bardeen, J., Cooper, L. N., & Schrieffer, J. R. (1957). Microscopic theory of superconductivity. *Physical Review*, *106*(1), 162.

[38] Meservey, R., & Tedrow, P. M. (1969). Measurements of the kinetic inductance of superconducting linear structures. *Journal of Applied Physics*, *40*(5), 2028-2034.

[39] Rudner, S., & Claeson, T. (1979). Arrays of superconducting tunnel junctions as low-noise 10-GHz mixers. Applied Physics Letters, 34(10), 711-713.

[40] Dolan, G. J., Phillips, T. G., & Woody, D. P. (1979). Low-noise 115-GHz mixing in superconducting oxide-barrier tunnel junctions. Applied Physics Letters, 34(5), 347-349

[41] Pekola, J. P., Hirvi, K. P., Kauppinen, J. P., & Paalanen, M. A. (1994). Thermometry by arrays of tunnel junctions. Physical review letters, 73(21), 2903

[42] Ariyoshi, S., Otani, C., Dobroiu, A., Sato, H., Kawase, K., Shimizu, H. M. *et al.* & Matsuo, H. (2006). Terahertz imaging with a direct detector based on superconducting tunnel junctions. Applied physics letters, 88(20), 203503.

[43] Verhoeve, P., Martin, D. D. E., Hijmering, R. A., Verveer, J., van Dordrecht, A., Sirbi, G., *et al.* & Peacock, A. (2006). S-Cam 3: Optical astronomy with a STJ-based imaging spectrophotometer. Nuclear Instruments and Methods in Physics Research Section A: Accelerators, Spectrometers, Detectors and Associated Equipment, 559(2), 598-601.

[44] Friedrich, S. (2008). Superconducting tunnel junction photon detectors: Theory and applications. *Journal of Low Temperature Physics*, *151*(1), 277-286.

[45] Fagaly, R. L. (2006). Superconducting quantum interference device instruments and applications. Review of scientific instruments, 77(10), 101101.

[46] Jaklevic, R. C., Lambe, J., Silver, A. H., & Mercereau, J. E. (1964). Quantum interference effects in Josephson tunneling. Physical Review Letters, 12(7), 159.

[47] Stewart, W. C. (1968). Current-voltage characteristics of Josephson junctions. Applied Physics Letters, 12(8), 277-280.

[48] Cabrera, B., Clarke, R. M., Colling, P., Miller, A. J., Nam, S., & Romani, R. W. (1998). Detection of single infrared, optical, and ultraviolet photons using superconducting transition edge sensors. *Applied Physics Letters*, *73*(6), 735-737.

[49] Kerman, A. J., Yang, J. K., Molnar, R. J., Dauler, E. A., & Berggren, K. K. (2009). Electrothermal feedback in superconducting nanowire single-photon detectors. *Physical review B*, *79*(10), 100509.

[50] Tsujino, K., Fukuda, D., Fujii, G., Inoue, S., Fujiwara, M., Takeoka, M., & Sasaki, M. (2010). Sub-shot-noise-limit discrimination of on-off keyed coherent signals via a quantum receiver with a superconducting transition edge sensor. *Optics express*, *18*(8), 8107-8114.

[51] Yoon, J., Clarke, J., Gildemeister, J. M., Lee, A. T., Myers, M. J., Richards, P. L., & Skidmore, J. T. (2001). Single superconducting quantum interference device multiplexer for arrays of low-temperature sensors. Applied Physics Letters, 78(3), 371-373.

[52] Miller, A. J., Nam, S. W., Martinis, J. M., & Sergienko, A. V. (2003). Demonstration of a low-noise near-infrared photon counter with multiphoton discrimination. *Applied Physics Letters*, *83*(4), 791-793.

[53] Chervenak, J. A., Irwin, K. D., Grossman, E. N., Martinis, J. M., Reintsema, C. D., & Huber, M. E. (1999). Superconducting multiplexer for arrays of transition edge sensors. Applied Physics Letters, 74(26), 4043-4045.

[54] de Korte, P. A., Beyer, J., Deiker, S., Hilton, G. C., Irwin, K. D., MacIntosh, M. *et al.* & Huber, M. E. (2003). Time-division superconducting quantum interference device multiplexer for transition-edge sensors. Review of Scientific Instruments, 74(8), 3807-3815.

[55] Reintsema, C. D., Beyer, J., Nam, S. W., Deiker, S., Hilton, G. C., Irwin, K. *et al.* & MacIntosh, M. (2003). Prototype system for superconducting quantum interference device multiplexing of large-format transition-edge sensor arrays. Review of Scientific Instruments, 74(10), 4500-4508.

[56] Gao, J., Vissers, M. R., Sandberg, M. O., Da Silva, F. C. S., Nam, S. W., Pappas, D. P., *et al.* & Leduc, H. G. (2012). A titanium-nitride near-infrared kinetic inductance photon-counting detector and its anomalous electrodynamics. Applied Physics Letters, 101(14), 142602.

[57] Asif Khan, M., Bhattarai, A., Kuznia, J. N., & Olson, D. T. (1993). High electron mobility transistor based on a GaN-Al x Ga1− x N heterojunction. *Applied Physics Letters*, *63*(9), 1214-1215.

[58] Maloney, P. R., Czakon, N. G., Day, P. K., Downes, T. P., Duan, R., Gao, J. *et al.* & Mazin, B. A. (2010, July). MUSIC for sub/millimeter astrophysics. In *SPIE Astronomical Telescopes+ Instrumentation* (pp. 77410F-77410F). International Society for Optics and Photonics.

[59] Wen, C. P. (1969). Coplanar waveguide: A surface strip transmission line suitable for nonreciprocal gyromagnetic device applications. *IEEE Transactions on Microwave Theory and Techniques*, *17*(12), 1087-1090.

[60] Duan, R., McHugh, S., Serfass, B., Mazin, B. A., Merrill, A., Golwala, S. R. *et al.* & Glenn, J. (2010). An open-source readout for MKIDs. *Millimeter, Submillimeter, and Far-Infrared Detectors and Instrumentation for Astronomy V*, *7741*, 77411V.

[61] McHugh, S., Mazin, B. A., Serfass, B., Meeker, S., O'Brien, K., Duan, R. *et al.* & Werthimer, D. (2012). A readout for large arrays of microwave kinetic inductance detectors. *Review of Scientific Instruments*, *83*(4), 044702.

[62] Gol'tsman, G. N., Okunev, O., Chulkova, G., Lipatov, A., Semenov, A., Smirnov, K., *et al.* & Sobolewski, R. (2001). Picosecond superconducting single-photon optical detector. *Applied Physics Letters*, *79*(6), 705-707.

[63] Miki, S., Fujiwara, M., Sasaki, M., Baek, B., Miller, A. J., Hadfield, R. H. *et al.* & Wang, Z. (2008). Large sensitive-area NbN nanowire superconducting single-photon detectors fabricated on single-crystal MgO substrates. *Applied Physics Letters*, *92*(6), 061116.

[64] Marsili, F., Bitauld, D., Fiore, A., Gaggero, A., Mattioli, F., Leoni, R. *et al.* & Lévy, F. (2008). High efficiency NbN nanowire superconducting single photon detectors fabricated on MgO substrates from a low temperature process. *Optics express*, *16*(5), 3191-3196.

[65] Marsili, F., Gaggero, A., Li, L. H., Surrente, A., Leoni, R., Lévy, F., & Fiore, A. (2009). High quality superconducting NbN thin films on GaAs. *Superconductor Science and Technology*, *22*(9), 095013.

[66] Stern, J. A., & Farr, W. H. (2007). Fabrication and characterization of superconducting NbN nanowire single photon detectors. *IEEE Transactions on Applied Superconductivity*, *17*(2), 306-309.

[67] Tanner, M. G., Alvarez, L. S. E., Jiang, W., Warburton, R. J., Barber, Z. H., & Hadfield, R. H. (2012). A superconducting nanowire single photon detector on lithium niobate. *Nanotechnology*, *23*(50), 505201.

[68] Il'in, K. S., Lindgren, M., Currie, M., Semenov, A. D., Gol'tsman, G. N., Sobolewski, R., *et al.* & Gershenzon, E. M. (2000). Picosecond hot-electron energy relaxation in NbN superconducting photodetectors. *Applied Physics Letters*, *76*(19), 2752-2754.

[69] Kooi, J. W., Stern, J. A., Chattopadhyay, G., LeDuc, H. G., Bumble, B., & Zmuidzinas, J. (1998). Low-loss NbTiN films for THz SIS mixer tuning circuits. *International journal of infrared and millimeter waves*, *19*(3), 373-383.

[70] Marsili, F., Verma, V. B., Stern, J. A., Harrington, S., Lita, A. E., Gerrits, T. *et al.* & Nam, S. W. (2013). Detecting single infrared photons with 93% system efficiency. *Nature Photonics*, *7*(3), 210-214.

[71] Li, J., Kirkwood, R. A., Baker, L. J., Bosworth, D., Erotokritou, K., Banerjee, A. *et al.* & Hadfield, R. H. (2016). Nano-optical single-photon response mapping of waveguide integrated molybdenum silicide (MoSi) superconducting nanowires. *Optics express*, *24*(13), 13931-13938.

[72] Verma, V. B., Lita, A. E., Vissers, M. R., Marsili, F., Pappas, D. P., Mirin, R. P., & Nam, S. W. (2014). Superconducting nanowire single photon detectors fabricated from an amorphous Mo0. 75Ge0. 25 thin film. *Applied Physics Letters*, *105*(2), 022602.

[73] Hofherr, M., Arndt, M., Il'in, K., Henrich, D., Siegel, M., Toussaint, J. *et al.* & Meyer, H. G. (2013). Time-tagged multiplexing of serially biased superconducting nanowire single-photon detectors. *IEEE Transactions on Applied Superconductivity*, *23*(3), 2501205-2501205.

[74] Ejrnaes, M., Casaburi, A., Cristiano, R., Quaranta, O., Marchetti, S., & Pagano, S. (2009). Maximum count rate of large area superconducting single photon detectors. *Journal of Modern Optics*, *56*(2-3), 390-394.

[75] Dorenbos, S. N., Reiger, E. M., Akopian, N., Perinetti, U., Zwiller, V., Zijlstra, T., & Klapwijk, T. M. (2008). Superconducting single photon detectors with minimized polarization dependence. *Applied Physics Letters*, *93*(16), 161102.

[76] Kerman, A. J., Dauler, E. A., Yang, J. K., Rosfjord, K. M., Anant, V., Berggren, K. K., *et al.* & Voronov, B. M. (2007). Constriction-limited detection efficiency of superconducting nanowire single-photon detectors. *Applied Physics Letters*, *90*(10), 101110.

[77] Pozar, D. M. (2009). Microwave engineering. John Wiley & Sons.

[78] Hu, X., Holzwarth, C. W., Masciarelli, D., Dauler, E. A., & Berggren, K. K. (2009). Efficiently coupling light to superconducting nanowire single-photon detectors. IEEE Transactions on Applied Superconductivity, 19(3), 336-340.

[79] Kahl, O., Ferrari, S., Kovalyuk, V., Goltsman, G. N., Korneev, A., & Pernice, W. H. (2015). Waveguide integrated superconducting single-photon detectors with high internal quantum efficiency at telecom wavelengths. Scientific reports, 5, 10941.

[80] Pernice, W. H., Schuck, C., Minaeva, O., Li, M., Goltsman, G. N., Sergienko, A. V., & Tang, H. X. (2012). High-speed and high-efficiency travelling wave single-photon detectors embedded in nanophotonic circuits. Nature communications, 3, 1325.

[81] Sahin, D., Gaggero, A., Zhou, Z., Jahanmirinejad, S., Mattioli, F., Leoni, R. *et al.* & Fiore, A. (2013). Waveguide photon-number-resolving detectors for quantum photonic integrated circuits. Applied Physics Letters, 103(11), 111116.

[82] Semenov, A. D., Haas, P., Günther, B., Hübers, H. W., Il'in, K., Siegel, M. *et al.* & Smirnov, A. (2007). An energy-resolving superconducting nanowire photon counter. Superconductor Science and Technology, 20(10), 919.

[83] Zhao, Q., 赵清源, McCaughan, A., Bellei, F., Najafi, F., De Fazio, D. *et al.* & Berggren, K. K. (2013). Superconducting-nanowire single-photon-detector linear array. Applied Physics Letters, 103(14), 142602.

[84] Verma, V. B., Horansky, R., Marsili, F., Stern, J. A., Shaw, M. D., Lita, A. E. *et al.* & Nam, S. W. (2014). A four-pixel single-photon pulse-position array fabricated from WSi superconducting nanowire single-photon detectors. Applied Physics Letters, 104(5), 051115.

[85] Yamashita, T., Miki, S., Terai, H., Makise, K., & Wang, Z. (2012). Crosstalk-free operation of multielement superconducting nanowire single-photon detector array integrated with single-flux-quantum circuit in a 0.1 W Gifford–McMahon cryocooler. Optics letters, 37(14), 2982-2984.

[86] Likharev, K. K. (1993). Rapid single-flux-quantum logic. In *The New Superconducting Electronics* (pp. 423-452). Springer Netherlands.

[87] Chan, V. W. (2003). Optical satellite networks. *Journal of Lightwave Technology*, *21*(11), 2811.

[88] Nordholt, J. E., Hughes, R. J., Morgan, G. L., Peterson, C. G., & Wipf, C. C. (2002, April). Present and future free-space quantum key distribution. In *High-Power Lasers and Applications* (pp. 116-126). International Society for Optics and Photonics.

[89] Boroson, D. M., Robinson, B. S., Murphy, D. V., Burianek, D. A., Khatri, F., Kovalik, J. M., *et al.* & Cornwell, D. M. (2014, March). Overview and results of the lunar laser communication demonstration. In SPIE LASE (pp. 89710S-89710S). International Society for Optics and Photonics.

[90] Gisin, N., Ribordy, G., Tittel, W., & Zbinden, H. (2002). Quantum cryptography. *Reviews of modern physics*, *74*(1), 145.

[91] Gisin, N., & Thew, R. (2007). Quantum communication. *Nature photonics*, *1*(3), 165-171.

[92] Zhao, Y., Qi, B., Ma, X., Lo, H. K., & Qian, L. (2006). Experimental quantum key distribution with decoy states. *Physical review letters*, *96*(7), 070502.

[93] Scarani, V., Acin, A., Ribordy, G., & Gisin, N. (2004). Quantum cryptography protocols robust against photon number splitting attacks for weak laser pulse implementations. *Physical review letters*, *92*(5), 057901.

[94] Ling, A., Peloso, M., Marcikic, I., Lamas-Linares, A., & Kurtsiefer, C. (2008, February). Experimental E91 quantum key distribution. In *Integrated Optoelectronic Devices 2008* (pp. 69030U-69030U). International Society for Optics and Photonics.

[95] Mu, Y., Seberry, J., & Zheng, Y. (1996). Shared cryptographic bits via quantized quadrature phase amplitudes of light. *Optics communications*, *123*(1), 344-352.

[96] Ursin, R., Tiefenbacher, F., Jennewein, T., & Zeilinger, A. (2007). Applications of quantum communication protocols in real world scenarios toward space. *e & i Elektrotechnik und Informationstechnik*, *124*(5), 149-153.

[97] Liao, S. K., Yong, H. L., Liu, C., Shentu, G. L., Li, D. D., Lin, J., *et al.* & Chen, W. (2017). Long-distance free-space quantum key distribution in daylight towards inter-satellite communication. Nature Photonics, 11(8), 509-513.

[98] Northend, C. A., R. C. Honey, and W. E. Evans. "Laser radar (lidar) for meteorological observation.

[99] Gold, M. (1985). Design of a long-range single-mode OTDR. *Journal of lightwave technology*, *3*(1), 39-46.

[100] McCarthy, A., Collins, R. J., Krichel, N. J., Fernández, V., Wallace, A. M., & Buller, G. S. (2009). Long-range time-of-flight scanning sensor based on high-speed time-correlated single-photon counting. *Applied optics*, *48*(32), 6241-6251.

[101] Ibisch, A., Stümper, S., Altinger, H., Neuhausen, M., Tschentscher, M., Schlipsing, M. *et al.* & Knoll, A. (2013, June). Towards autonomous driving in a parking garage: Vehicle localization and tracking using environment-embedded lidar sensors. In Intelligent Vehicles Symposium (IV), 2013 IEEE (pp. 829-834). IEEE.

[102] Moerner, W. E., Orrit, M., Wild, U. P., & Basché, T. (Eds.). (2008). *Single-molecule optical detection, imaging and spectroscopy*. John Wiley & Sons.

[102] Lee, K. G., Chen, X. W., Eghlidi, H., Kukura, P., Lettow, R., Renn, A. *et al.* & Götzinger, S. (2011). A planar dielectric antenna for directional single-photon emission and near-unity collection efficiency. *Nature Photonics*, *5*(3), 166-169.

[103] Aharonovich, I., Englund, D., & Toth, M. (2016). Solid-state single-photon emitters. Nature Photonics, 10(10), 631-641.

[104] Rezus, Y. L. A., Walt, S. G., Lettow, R., Renn, A., Zumofen, G., Götzinger, S., & Sandoghdar, V. (2012). Single-photon spectroscopy of a single molecule. *Physical review letters*, *108*(9), 093601.

[105] Avenhaus, M., Eckstein, A., Mosley, P. J., & Silberhorn, C. (2009). Fiber-assisted single-photon spectrograph. *Optics letters*, *34*(18), 2873-2875.

[106] Brida, G., Chekhova, M. V., Genovese, M., Gramegna, M., & Krivitsky, L. A. (2006). Dispersion spreading of biphotons in optical fibers and two-photon interference. *Physical review letters*, *96*(14), 143601.

[107] Barnoski, M. K., & Jensen, S. M. (1976). Fiber waveguides: a novel technique for investigating attenuation characteristics. *Applied Optics*, *15*(9), 2112-2115.

[108] Farahani, M. A., & Gogolla, T. (1999). Spontaneous Raman scattering in optical fibers with modulated probe light for distributed temperature Raman remote sensing. Journal of Lightwave Technology, 17(8), 1379-1391.

[109] Barnoski, M., Rourke, M., Jensen, S. M., & Melville, R. T. (1977). Optical time domain reflectometer. Applied optics, 16(9), 2375-2379.

[110] Horiguchi, T., & Tateda, M. (1989). Optical-fiber-attenuation investigation using stimulated Brillouin scattering between a pulse and a continuous wave. Optics Letters, 14(8), 408-410.

[111] Dyer, S. D., Tanner, M. G., Baek, B., Hadfield, R. H., & Nam, S. W. (2012). Analysis of a distributed fiber-optic temperature sensor using single-photon detectors. *Optics express*, *20*(4), 3456-3466.

[112] Hartog, A. (1983). A distributed temperature sensor based on liquid-core optical fibers. Journal of Lightwave Technology, 1(3), 498-509.

[113] Rogers, A. J. (1980). Polarisation optical time domain reflectometry. Electronics Letters, 16(13), 489-490.

[114] Hartog, A. H., Payne, D. N., & Conduit, A. J. (1980). Polarisation optical-time-domain reflectometry: experimental results and application to loss and birefringence measurements in single-mode optical fibres.

[115] Culverhouse, D., Farahi, F., Pannell, C. N., & Jackson, D. A. (1989). Potential of stimulated Brillouin scattering as sensing mechanism for distributed temperature sensors. Electronics Letters, 25(14), 913-915.

[116] Horiguchi, T., Kurashima, T., & Tateda, M. (1989). Tensile strain dependence of Brillouin frequency shift in silica optical fibers. IEEE Photonics Technology Letters, 1(5), 107-108.

[117] Parker, T. R., Farhadiroushan, M., Handerek, V. A., & Roger, A. J. (1997). A fully distributed simultaneous strain and temperature sensor using spontaneous Brillouin backscatter. IEEE Photonics Technology Letters, 9(7), 979-981.

[118] Parker, T. R., Farhadiroushan, M., Handerek, V. A., & Rogers, A. J. (1997). Temperature and strain dependence of the power level and frequency of spontaneous Brillouin scattering in optical fibers. *Optics letters*, *22*(11), 787-789.

[119] Wait, P. C., & Newson, T. P. (1996). Landau Placzek ratio applied to distributed fibre sensing. *Optics Communications*, *122*(4-6), 141-146.

[120] Shimizu, K., Horiguchi, T., Koyamada, Y., & Kurashima, T. (1994). Coherent self-heterodyne Brillouin OTDR for measurement of Brillouin frequency shift distribution in optical fibers. *Journal of Lightwave Technology*, *12*(5), 730-736.

[121] Othonos, A., Kalli, K., Pureur, D., & Mugnier, A. (2006). Fibre bragg gratings. In Wavelength Filters in Fibre Optics (pp. 189-269. Springer Berlin Heidelberg

[122] Majumder, M., Gangopadhyay, T. K., Chakraborty, A. K., Dasgupta, K., & Bhattacharya, D. K. (2008). Fibre Bragg gratings in structural health monitoring—Present status and applications. *Sensors and Actuators A: Physical*, *147*(1), 150-164.

[123] James, S. W., Dockney, M. L., & Tatam, R. P. (1996). Simultaneous independent temperature and strain measurement using in-fibre Bragg grating sensors. *Electronics Letters*, *32*(12), 1133-1134.

[124] Meltz, G., & Morey, W. W. (1991, December). Bragg grating formation and germanosilicate fiber photosensitivity. In *International Workshop on Photoinduced Self-Organization Effects in Op* (pp. 185-199). International Society for Optics and Photonics.

[125] Morey, W. W., Meltz, G., & Weiss, J. M. (1992). Evaluation of a fiber Bragg grating hydrostatic pressure sensor. In *Proc. OFS* (Vol. 8).

[126] Xu, M. G., Archambault, J. L., Reekie, L., & Dakin, J. P. (1994). Thermally-compensated bending gauge using surface-mounted fibre gratings. *International Journal of Optoelectronics*, *9*(3), 281-284.

[127] Brady, G. P., Kalli, K., Webb, D. J., Jackson, D. A., Reekie, L., & Archambault, J. L. (1997). Simultaneous measurement of strain and temperature using the first-and second-order diffraction wavelengths of Bragg gratings. *IEE Proceedings-Optoelectronics*, *144*(3), 156-161.

[128] Saxena, M. K., Raju, S. D. V. S. J., Arya, R., Pachori, R. B., Ravindranath, S. V. G., Kher, S., & Oak, S. M. (2015). Raman optical fiber distributed temperature sensor using wavelet transform based simplified signal processing of Raman backscattered signals. *Optics & Laser Technology*, *65*, 14-24.

[129] Zhao, Q., Xia, L., Wan, C., Hu, J., Jia, T., Gu, M., *et al.* & Wu, P. (2015). Long-haul and high-resolution optical time domain reflectometry using superconducting nanowire single-photon detectors. Scientific reports, 5, 10441.

[130] Diamanti, E., Langrock, C., Fejer, M. M., Yamamoto, Y., & Takesue, H. (2006). 1.5 µm photon-counting optical time-domain reflectometry with a single-photon detector based on upconversion in a periodically poled lithium niobate waveguide. *Optics letters*, *31*(6), 727-729.

[131] Tanner, M. G., Dyer, S. D., Baek, B., Hadfield, R. H., & Woo Nam, S. (2011). High-resolution single-mode fiber-optic distributed Raman sensor for absolute temperature measurement using superconducting nanowire single-photon detectors a. Applied Physics Letters, 99(20), 201110.

[132] Vo, T. D., He, J., Magi, E., Collins, M. J., Clark, A. S., Ferguson, B. G., *et al.* & Eggleton, B. J. (2014). Chalcogenide fiber-based distributed temperature sensor with sub-centimeter spatial resolution and enhanced accuracy. *Optics express*, *22*(2), 1560-1568.

[133] Lin, Q., Yaman, F., & Agrawal, G. P. (2007). Photon-pair generation in optical fibers through four-wave mixing: Role of Raman scattering and pump polarization. *Physical Review A*, *75*(2), 023803.

[134] Lund, J. W., & Boyd, T. L. (2016). Direct utilization of geothermal energy 2015 worldwide review. *Geothermics*, *60*, 66-93.

[135] Simmons, S. F. (2013). Fluid-mineral equilibria in great basin geothermal systems: implications for chemical geothermometry. In Proceedings, 38th Workshop on Geothermal Reservoir Engineering, Stanford University, Stanford, California, 1 (Vol. 8).

[136] Wishart, D. N. (2013). Geothermometry and shallow circullation of a low enthalpy system: The Bath geothermal reservoir Jamaica. In *Thirty-Eighth Workshop on Geothermal Reservoir Engineering*, Stanford, California.

[137] Chen, K., Zhou, X., Yang, B., Peng, W., & Yu, Q. (2015). A hybrid fiber-optic sensing system for down-hole pressure and distributed temperature measurements. Optics & Laser Technology, 73, 82-87.

[138] Brown, G. (2008). Downhole temperatures from optical fiber. Oilfield Review, 2009(20), 4.

Chapter 3 – Experimental and analytical methods

This chapter explains the procedures behind the fabrication of superconducting nanowires single-photon detectors, from the film growth to the patterning, etching and complementary metal deposition. This chapter describes also testing techniques, and the setup of cryostat. Time–correlated single-photon counting techniques are discussed in detail, as these are used in detector timing jitter characterization and form the basis of fibre optic temperature sensing measurements.

3.1 Fabrication procedures

3.1.1 Film growth

There are several techniques for the deposition of layers (superconducting or not) on top of a substrate. This section will focus on two physical vapor deposition methods: sputtering [1] and electron beam evaporation [2]. Other methods like atomic layer deposition [3] or chemical vapour deposition [4], will not be discussed as they were not adopted for the fabrication flow of the devices in the thesis.

Sputtering is a method in which a material from a source (or target) mounted on a cathode is ejected onto a substrate mounted onto an anode (Fig. 3.1). Both are placed in a vacuum chamber where an inert gas is pumped into the chamber at a certain pressure, bombing the target in a prefixed time. Some atoms are hence released by the target and a fraction of them are ionised. A DC current applied between anode and cathode creates an electric field that ballistically drives the ions from the target toward the substrate (DC magnetron sputtering). The ions impacting with the vacuum chamber cause resputtering[1].

At higher gas pressures, the ions collide with the gas atoms that act as a moderator and move diffusively, reaching the substrate or vacuum chamber wall and condensing after undergoing a random walk. The entire range from high-energy

---

[1] Re-emission of the deposited material during the deposition process by ion or atom bombardment.

ballistic impact to low-energy thermalized motion is accessible by changing the background gas pressure. For efficient momentum transfer, the atomic weight of the sputtering gas should be close to the atomic weight of the target. Reactive gases can also be used to sputter compounds. The compound can be formed on the target surface, in-flight or on the substrate depending on the process parameters: in NbN sputtering there is a mix of the inert gas (Ar) and the reactive gas (N) while for MoSi, MoGe or NbTiN, two targets are simultaneously sputtered (co-sputtering process) at different currents.

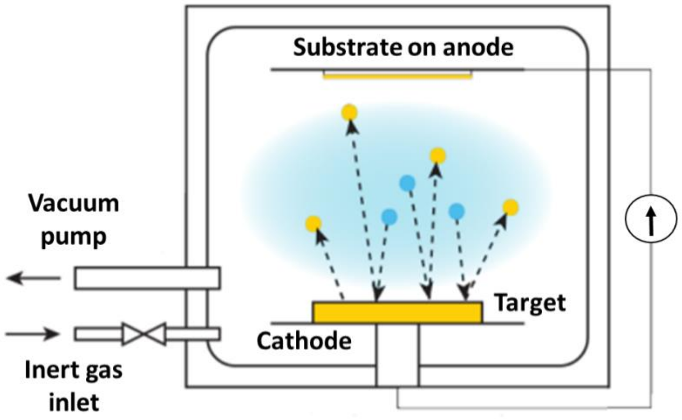

Fig. 3.1: Schematic illustration of a generic sputtering process. An inert gas (blue cloud/dots) is pumped into a vacuum chamber containing a substrate mounted on an anode and a target mounted on a cathode. The inert gas bombards the target and the released ions (yellow dots) are driven to the substrate by an electric field generated by a current applied between anode and cathode.

Electron beam evaporation is achieved via an electron beam emitted from a charged tungsten filament under high vacuum (Fig. 3.2). The directivity of the beam is regulated by an applied magnetic field generated by a deflecting magnet. The electron beam transforms the solid source (or crucible) into a gas of atoms that diffuses in the vacuum chamber and hits the sample, condensing into a layer. A shutter, located between the crucible and the sample, is opened and closed at given time intervals in order to regulate the thickness of the layer deposited.

The evaporation method is technically easier and cheaper than sputtering, offering also similar performances in terms of the quality of the films. However, the evaporation cannot deposit compounds but only a series of layers. It is a serious limitation for the superconducting compounds typically employed for SNSPDs.

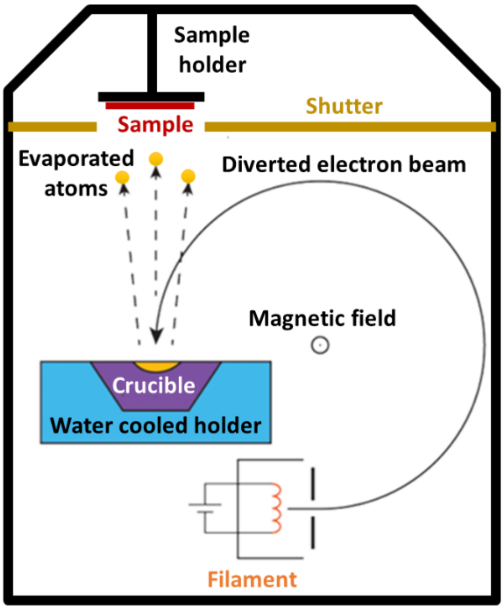

Fig. 3.2: Schematic illustration of an electron beam evaporation process. An electron beam is produced from a filament and diverted by a magnet toward a crucible in order to initiate the evaporations of its atoms (yellow dots). Such a gas diffuses onto the sample when the shutter is in the open state.

3.1.2 Electron beam lithography

In electronics, lithography is a process adopted in micro and nanofabrication to pattern parts of a thin film or the bulk of a substrate. Modern electronic devices must deliver with performance enhancements, such as low-power consumption and increased device density, that have spurred progress to miniaturized feature sizes. Hence, conventional optical or ultraviolet photolithography is becoming insufficient, although it is a rapid and relatively cheap technique: the transfer procedure consists in a single exposure, through a mask prepared separately, of a large area of the substrate; between the mask and the substrate, a corrective projection lens is placed.

Conversely, electron beam lithography (EBL) is characterized by an extremely high resolution and flexibility. It consists of the controlled movement of a collimated beam on the surface of the substrate to write a pattern, down to nanometric scales. Also, as no mask preparation is involved in the process, EBL is convenient when the pattern needs to be adjusted several times and the total area to be written is small.

An EBL system consists of an electron gun, a collimator, magnetic lenses, shutter and deflecting coils [5]. In the electron gun, electrons extracted from a filament are accelerated by an electric field. This stream of electrons is then focused by the collimator and magnetic lenses. The position of the focused electron beam can then be controlled using the deflecting coils. The wavelength of the electrons, given by De Broglie's relation $\lambda = h/p_e$ where p_e is the momentum of the electrons, can be made much smaller than optical wavelengths by controlling the acceleration voltage of the electron gun and therefore allows for the fabrication of features of the order of a few nanometers.

In practice, the desired pattern is initially drawn using a layout generation software. Afterward, on the EBL control software, the graphic file is completed by some parameters in order to assign specific features to the pattern. Firstly, an electron dose (expressed in $\mu C/cm^2$) gets associated to every pattern. The dose is a function of the resist (a radiation sensitive polymer film) and the material to be processed. Then, the file is processed through a software that fractures each area to be exposed in smaller ones called trapezia, which correspond to each position of exposure of the electron beam. Trapezia are situated over a square lattice grid, whose minimum distance between its points represents the resolution of the patterning. The beam scans the grid horizontally, exposing only dots separated by a fixed gap called "Beam Step Size" (BSS, i.e. an integer multiple of the resolution). Instead, the "Spot Size" (SS) defines the beam-width, which is finite and related to current and diameter of the aperture of the beam (Fig. 3.3). Of course, finer is the SS and longer is the exposure time, for a given pattern.

Substantially, a pattern is a matrix of exposed points, subdivided into blocks. Those blocks are associated to stage movements because the EBL tools have a limited writing field, beyond which electrons start to be deflected with distortion. The accuracy of stage positioning is a crucial parameter describing the quality of an EBL tools. Stage misalignments induce stitching errors at the borders of the writing field of the beam.

The resolution is mainly limited by the so-called proximity effect [6]. It is due to the scattering of electrons in the resist and underlying substrate. In other words, a region larger than the beam-incidence results exposed. The effect can strongly deform the designed pattern. The EBL equipment used for the fabrication of the devices presented in *Chapter 4* is a Vistec VB6 UHR EWF. It offers a self-correction that reduces the proximity effect by modulating the exposure dose depending on the density of the patterns but the feature was not utilized. Additionally, the VB6 management software runs in terms of variable resolution unit (VRU), computed dividing the beam step size by the resolution.

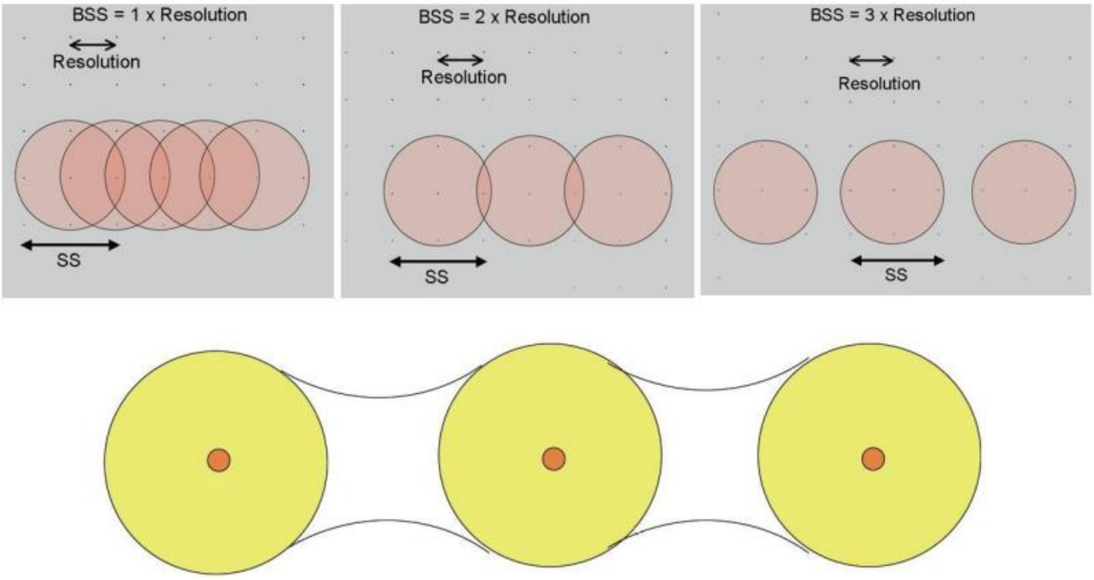

Fig. 3.3: Graphic explanation of the Beam Step Size. From the top left to top right it is linearly increased, until a threshold for which the line-edge roughness becomes a problem, as shown in the lower picture. Courtesy of Dr. S. Thoms.

3.1.3 Dry etching techniques

An etching process is required when the unmasked patterned region of the sample needs to be removed. In case of SNSPD fabrication, it is the step when the nanowire gets isolated from the whole superconducting film. Depending on whether the etchant agent is liquid or plasma, the process is named wet etching or dry etching, respectively. The dry technique is considered superior [7], in terms of selectivity and uniformity, due to a more precise etching time-control and a vertical etch-rate that massively exceeds the horizontal rate (anisotropic etching). This section will focus on a specific dry etching method called Reactive Ion Etching (RIE), as the devices proposed in the following chapter were etched in such manner. In RIE, the unmasked material is physically and chemically attacked by ions accelerated via an RF power applied to two parallel plates. Such power regulates, at the same time, the plasma generation; if increased after a certain threshold (related to the processed sample), the self-biasing voltage on the plate facing the mask can transfer to the ions an energy so high to reduce the etching selectivity (over-etching) or even to mechanically break the sample. In summary, the etching rate is a function of the plasma density which is itself a function of that RF power. The dry etching procedure can be described by four steps:

I. The reactive gases pumped into the chamber are transformed into active gas species, by electron collisional dissociation and ionization reaction.
II. Transport of the active species by diffusion from the bulk plasma of the discharge onto the surface of the sample.
III. Over the unmasked area of the sample, the reactive atoms are absorbed and progressively ablate the superficial electrons (chemical attack). Simultaneously, an ion-bombing break the bonds (physical attack).
IV. The outcoming volatile atoms are pumped out like chemical wastes.

The etching time depends on thickness and material to etch. An imprecise duration can originate over-etching issues (as an incorrect power applied). Under-etching issues are less frequent, due to the possibility to check the etching process with an interferometer.

3.2 Construction of a 2.4 K Gifford-McMahon cryostat

3.2.1 Introduction to cryogenic systems

The fastest way to reach temperatures compatible with the superconducting state is the immersion of the detector into liquid He. Such technical ease is counterbalanced by high costs and hazards of liquid He, that requires safety training for users [8]. Such a solution is therefore not attractive or practical for industrial and interdisciplinary research activities by non-physicists. The main other option is represented by closed-cycle cryocoolers [9] in which there is no contact between the cooling agent and the final user. The simplest method to refrigerate is based on the reverse Stirling cycle, from which subsequent technologies are derived, like the Gifford-McMahon (GM) cycle (Fig. 3.4), employed in a cryostat[2] assembled for the experiment illustrated in *Chapter 5*. The main elements are a compressor driving two pressure lines, a piston (usually called displacer), a regenerator (a porous body, usually cylindrical in shape, through which a gas passes back and forth in a cyclic motion) and a cold head. The SNSPD are attached on a stage of the cold head, which

---

[2] Original design: Natarajan, C. M. (2011). Superconducting nanowire single-photon detectors for advanced photon-counting applications (Doctoral dissertation, Heriot-Watt University).

is isolated from the environment by a closed canister. High pressure, high purity He circulates through the cold head, acting as heat transferring agent. According to the ideal gas equation, the temperature in the closed chamber is proportional to the product of pressure and volume that are artificially modified by a compressor through the cycle. The innovative element, compared with the Stirling cycle, is a rotary valve between the hot and cold sides of the system aimed to separate high and low pressure gas lines.

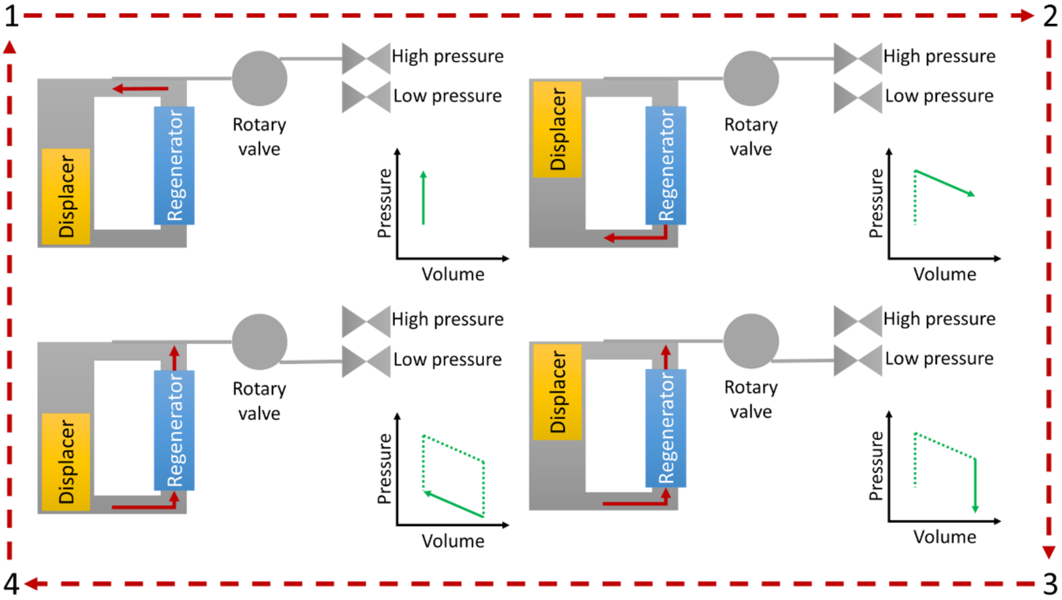

Fig. 3.4: Operation of the Gifford-McMahon (GM) cycle. 1) With the displacer at the bottom, the high pressure inlet is opened and the upper chamber is pressurized at a constant temperature. 2) The displacer is moved to the top, thus forcing out the gas from the top chamber through the regenerator to the lower chamber. This process cools the gas at a constant pressure. 3) The rotary valve switches the low pressure port. This process allows the gas in the lower chamber to expand and cool. This expansion displaces some gas out through the low pressure port doing some work. This is the main cooling step in the GM cycle for the gas. Due to the direct thermal contact, it will drive heat out of the sample space. 4) The cooled, low temperature gas is then forced out of the chamber with the displacer moving down. This process cools the regenerator, and thus the gas leaves the low pressure port near ambient temperature.

3.2.2 Assembling the setup

To reach temperatures of the order of 2.4 K, a multistage cryostat is required. The first stage operates at ~40 K while the second stage and the sample stage operates at ~2.4 K. A Sumitomo RDK101D cold head and a Sumitomo CNA-11C compressor unit were used to build the cryostat (Fig. 3.5) employed in *Chapter 5* experiment. This unit runs off a 13 A electrical outlet (with 1 kW power consumption) and requires only air cooling. The cold head was firstly fixed into a metal plane supported by four legs. Then, a hexagonal manifold was mounted at the base of the cold head. The manifold has six interfaces to be sealed by six flanges:

I. a flange hosts four SMA[3] connectors;
II. a flange hosts a 12-pin fisher connector as an interface between three[4] Lakeshore DT-670 calibrated Si-diode thermometers and a digital mainframe;
III. a flange hosts a plug and valve for the vacuum pumping action;
IV. a flange hosts an optical fibre feedthroughs;
V. last two flanges are blank.

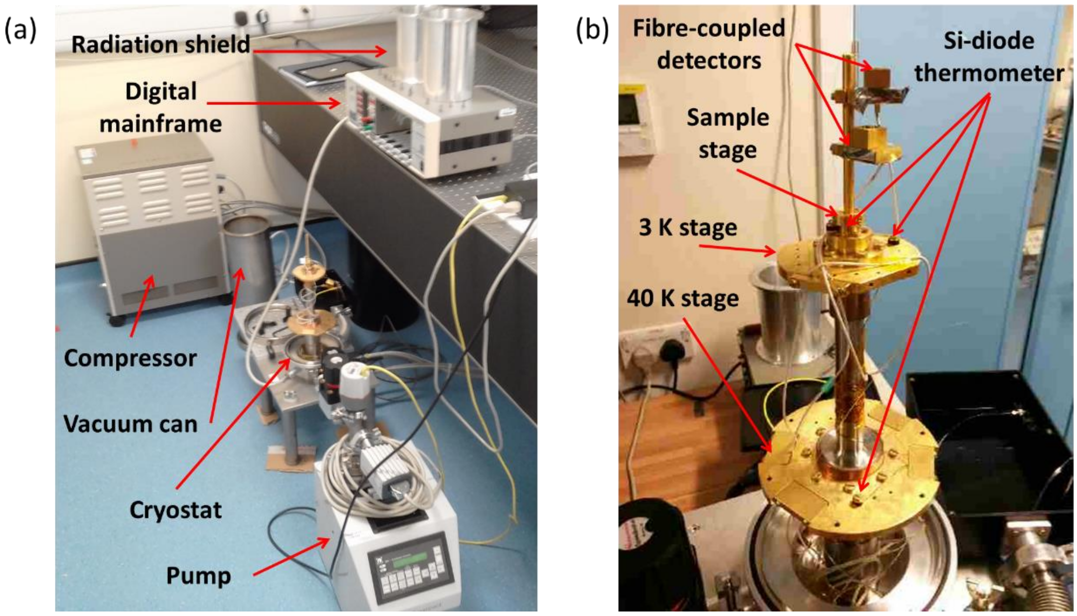

Fig. 3.5: (a) Photograph of a Gifford-McMahon cryogenic setup. (b) Zoom on the stages of the Sumitomo RDK-101D two-stage cold head.

An O-ring form an interface with the manifold and a stainless-steel vacuum can, that completely isolates the stages from the surrounding environment. Over the 40 K stage plate of the cryostat, a radiation shield was mounted for a full electromagnetic isolation of the samples to test. After the installation of all the components, the cryostat was leak-checked. Before turning-on the compressor, the system is pumped to a pressure of at least 10^{-5} mbar. Almost after 9 hours, the stages reach their final temperatures (Fig. 3.6).

---

[3] Sub-Miniature version A
[4] One per stage

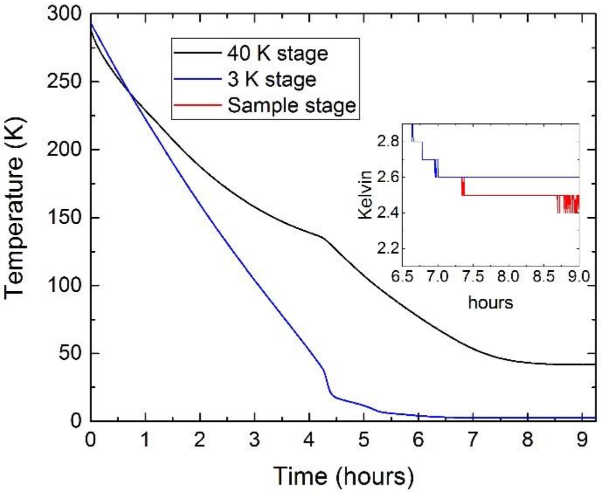

Fig. 3.6: Cooldown plot of the cryostat with a mounted SNSPD device. The cold head reaches base temperatures of ~2.4 K and 40 K in 9 hours. The inset shows the temperature variation between the 3 K stage and the sample stage. Data recorded with the temperature resolution of 0.1 K.

3.2.3 Packaging

The devices are attached to the cryostat using a sample mount (Fig. 3.7), consisting of a gold-coated oxygen-free, high-thermal conductivity copper base, four electrically isolated copper bond pads and a central adhesion spot, where a sample is attached using varnish.

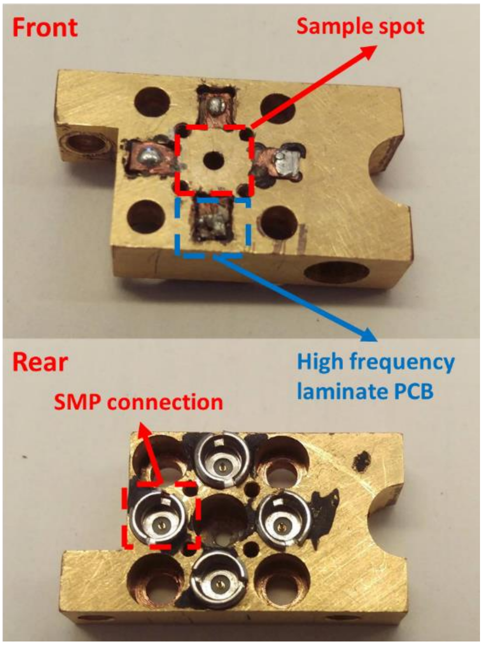

Fig. 3.7: Photographs of a sample mount for SNSPD. The electrical signals between the SNSPD and the cryostat are transmitted via SMP (Sub-Miniature Push-on) cables. The four SMP connectors on the rear of the sample mount are soldered to the copper bond-pads on-front (High-frequency laminate Printed Board Circuit), onto which the sample is wire-bonded.

The device is then wire-bonded using aluminium wire, connecting between the device's surface bond pads and the sample mount's bond pads, which are soldered to female SMP connectors. In case of fibre-coupling connection, there is also a cubic cap, screwed onto the front (frontside-coupling) or the rear (backside-coupling) of the sample mount in the middle of which a fibre ferrule is placed. An alignment procedure [11] is finally required to test the detector at its best.

3.3 Electro-optical analysis

3.3.1 Critical current measurement

A voltmeter and a variable current source are enough to measure the *I-V* characteristic and, therefore, the critical current I_C (explained in § ***2.4.1***) of an SNSPD (Fig. 3.8). The variable DC current generator is formed by an isolated voltage source module (SIM 928, Stanford Research System Inc.) in series with a load resistor R_L. The voltage source is hosted in a digital mainframe (SIM 900) with the voltmeter (SIM 970). A computer program sweeps the input voltage V by across a range of values in which $V/R_L > I_C$.

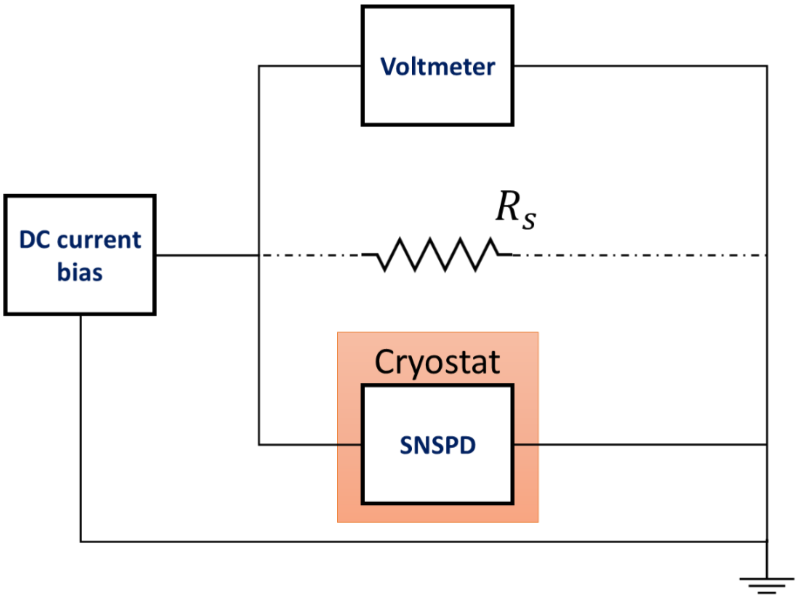

Fig. 3.8: Simplified schematic of the setup for *I-V* measurements. A voltmeter records the SNSPD input and output voltages. The *I-V* curves give an indication of the critical current of an SNSPD. An optional shunt resistor ($\boldsymbol{R_s}$) can be added to reduce the SNSPD dead time.

Optionally, in parallel with the SNSPD, a shunt resistor can be added. This component, typically 50 Ω (which is much lower than the resistance of a triggered device but higher if untriggered), shortens the dead time (explained in § ***2.1.5***) of the detector by collecting most the current flow. As the current is redirected, the heat on the detector is reduced. The use of a shunt resistor implies a slightly higher I_C (Fig. 3.9) which also implies a (fictional) higher detection efficiencies since some of the applied current is now going through the shunt.

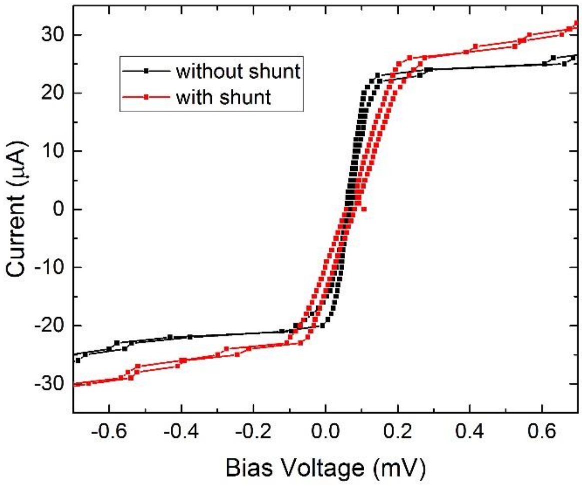

Fig. 3.9: Example of the effect of a 50 Ω shunt resistor on the *I-V* characteristic of the same SNSPD.

3.3.2 Kinetic inductance measurement

The kinetic inductance establishes the relaxation time of the output pulses in SNSPDs and could be also considered as an index of uniformity for a detector [19].

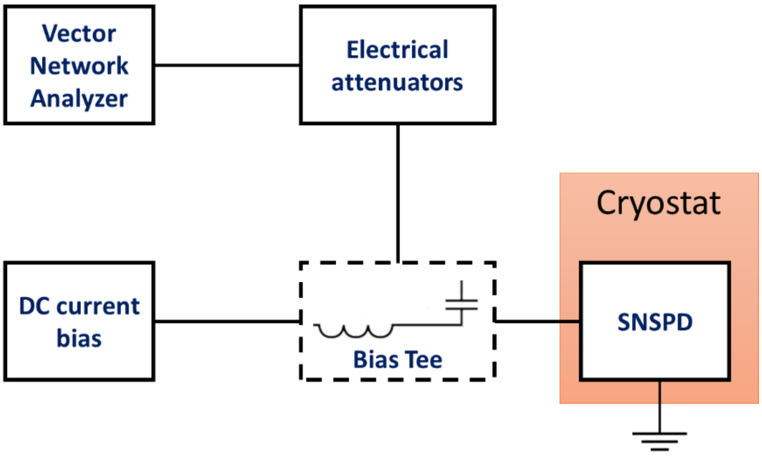

Fig. 3.10: Diagram of the setup for kinetic inductance measurements. A computer program sweeps a set of growing DC current bias over the SNSPD. In the meantime, from the inductive port of a bias tee, a vector network analyzer registers the associated induntances.

In practice, a one-port vector network analyser (VIA Bravo, AEA Technology Inc.), with frequencies from 0.1 MHz to 50 MHz, records the inductances as a function of a growing bias current (I_b) applied across the device. The *L-I* curves are later fitted by the following equation [12]:

$$L(T,I) = L_0\left[1 + \left({}^{2I}\!/_{3CI^*_c}\right)^2\right] \qquad \text{(Eq. 16).}$$

The parameter $C = I_c/I^*_c$, where I^*_c is the theoretical prediction of the I_c for nanowires with no constriction from the Ginzburg-Landau theory, was introduced by Kerman [13] to describe the effect of the nanowire's cross-section constriction on the I_c and on the kinetic inductance. Instead, L_0 represents the inductance of the single pixel for zero bias.

3.3.3 Detection efficiency measurement

Recalling the statements in § ***2.1.1***, the detection efficiency is computed by comparing the input optical power with the number of counts per second registering on the detector.

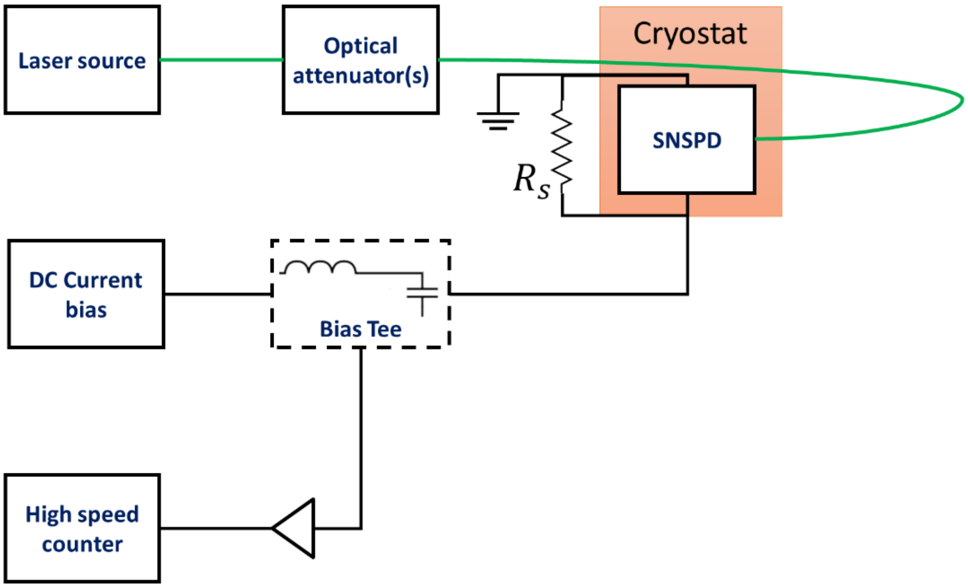

Fig. 3.11: Diagram of the setup for detection efficiency measurements. A laser pulse travels along the fibre feed-trough of the cryostat, from the source to the biased SNSPD and the high speed counter enumerates the detected photons. Black line: electrical connection. Green line: optical connection. $\boldsymbol{R_S}$: shunt resistor.

Experimentally, the input power is converted into a photon flux (Φ, i.e. the number of photons per second entering the cryostat). This value is obtained dividing the optical power read on a power meter (when no attenuation is applied) by the energy of a single photon *E* = *h·c/λ*, where *λ* is the central wavelength of the laser source.

For a complete characterization of the detector efficiency, the setup (Fig. 3.11) measures the recorded photons as a function of the bias (from $I_b \ll I_c$ to $I_b \cong I_c$) for several attenuations values (typically from 20dB to 120dB).

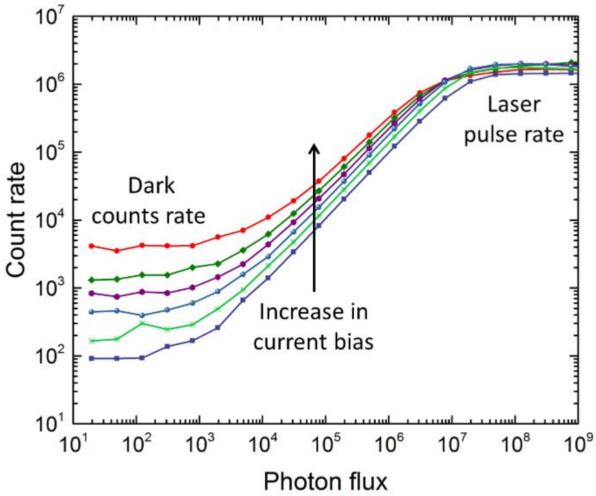

Fig. 3.12: Example of an SNSPD photon count rate (per second) plotted against the photon flux (per second) for a 1 MHz gain-switched diode laser.

From the outcoming curves, three regimes are usually observable (Fig. 3.12):

I. for a low photon fluxes, the count rate is relatively constant and the measurement is mainly an index of the dark count rate (DCR);

II. then, the detector switch into a regime where an increment of the photon flux increases the count rate;

III. finally, there is a saturation regime, in which an increment of the photon flux does not increase the count rate, now approaching the pulse rate of the laser.

Under the hypothesis that the first value recorded at any bias voltage is the number of dark pulses N_{dp} and taken the count rate N_c in the linear regime for every bias, an approximated detection efficiency SDE [14] is computed as follow:

$$SDE = \frac{N_c - N_{dp}}{\Phi} \qquad \text{(Eq. 17).}$$

3.3.4 Nano-optical mapping for SNSPDs

For the optical test of the arrays presented in *Chapter 4*, a fibre-coupled miniature confocal microscope (MCM) integrated in a closed-cycle pulse-tube cryostat [16] was used. Although not employed for confocal microscopy, this setup[5] (Fig. 3.13) provides a closely focused spot to spatially map the efficiency of an SNSPD and it permits scanning of multiple pixels in a single thermal cycle.

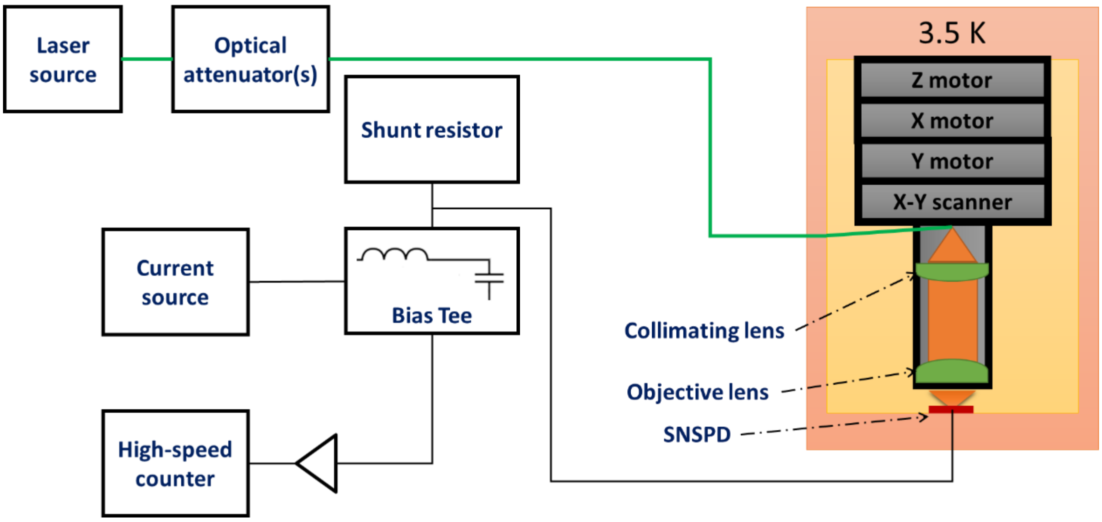

Fig. 3.13: Diagram of the confocal microscope configuration. Integrated in a 3.5 K cryostat, it maps the efficiency of an SNSPD over 40 x 40 μm^2 (at cryogenic temperatures). An attenuated laser source is sent to a collimating lens. The outcoming beam is focused toward by an objective lens. The three-dimensional beam directivity is controlled by piezoelectric motors, driving a X-Y scanner for sub-nanometre steps. Black line: electrical connection. Green line: optical connection.

A stack of two piezoelectric motors ANPx101 move the optical beam, providing high resolution and high stability positioning over 5 mm in X and Y. The Z movement is controlled by an ANPz101. This gives the ability to focus the light to a point that may be even translated across the device. An independent X-Y stage, an Attocube ANSxy100, also allows the MCM to scan a 40 x 40 μm^2 area[6] with sub-nanometre step size [18]. Light delivered by the fibre is collimated by an aspheric lens of numerical aperture (NA) equal to 0.15 [19] and then focused by a second aspheric lens with NA = 0.68 [20]. Both lenses have an anti-reflection coating suitable in the wavelengths interval 1050-1620 nm.

From an operational perspective, the MCM is scanned in a raster pattern of the Gaussian spot of light over a surface. The observed photo-response is a convolution between the geometrical response of the SNSPD under investigation and the Gaussian FWHM-spot. Though theoretically computable by means of an inverse Fast

---

[5] Built by Dr. Michael Tanner [17].

[6] At cryogenic temperatures. At room temperature, the maximum area is 70 x 70 μm^2.

Fourier Transform, the reconversion backward to the pure SNSPD geometry is essentially impossible due to optical and thermal noise.

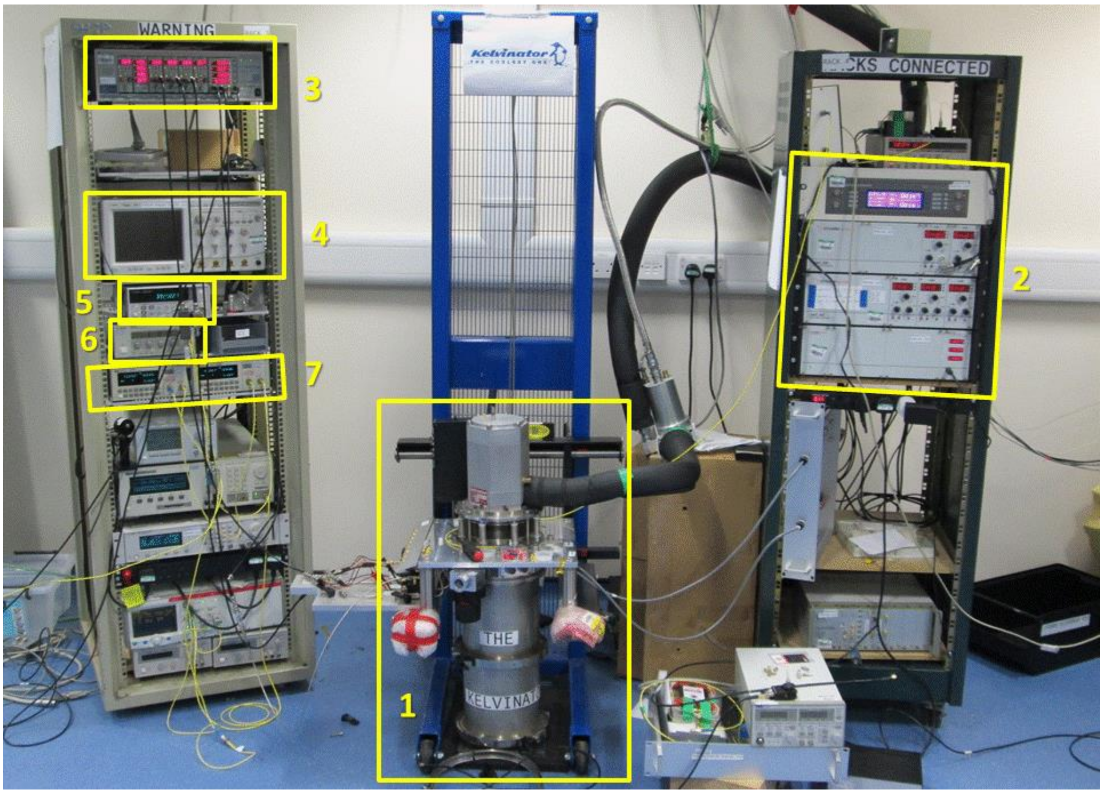

Fig. 3.14: Picture of the entire experimental setup for the characterization of an SNSPD array: 1) Cryocooler; 2) Attocube ANC150 housing including the ANC200 scanner controller and the ARC200 X-Y-Z motor positions reader; 3) SRS SIM900 digital mainframe including temperature monitor, isolated bias voltage sources and multimeters; 4) Agilent Infiniium DSO80804A oscilloscope; 5) Agilent 5313A universal counter; 6) Agilent 11896A polarization controller; 7) A series of two HP 8156A optical attenuator.

3.3.5 Time correlated single photon counting

Time correlated single photon counting (TCSPC) techniques [21] identify the temporal shape of the pulses from a SPD and therefore locate temporal events in an optical system.The timing of each event in detection, i.e. “Stop”, is recorded and compared to that of another signal, the “Start” event, descending from the light source. The relative timing between the Start and Stop signals is stored while the amplitude of each signal is irrelevant. For this reason, TCSPC techniques can be considered independent from gain-noise. The only source of internal noise affecting the system is due to the dark counts rate of the detector [22]. However, gain-noise can contribute to a timing error depending on pulse amplitude discriminator levels.

In an analogue TCSPC system, a start pulse is sent, generally through a timing discriminator[7], to a Time to Amplitude Converter (TAC), which typically initiates the charging of a capacitor, successively arrested by a pulse from the single photon detector. The TAC then releases a pulse whose amplitude is proportional to the charge on the capacitor and, therefore, the time difference between the start and stop signals. The TAC output pulse is sent through an analogue to digital converter and a count can be added to a data store in a bin corresponding to that timing interval.

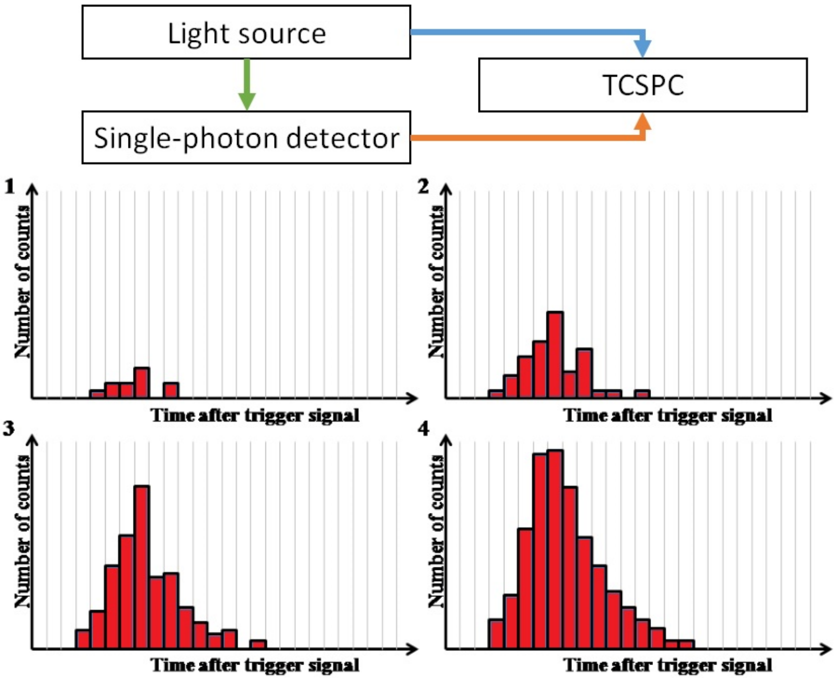

Fig. 3.15: Schematic illustration of a Time Correlated Single Photon Counting (TCSPC) measurement. A light source provides a photon flux to the detector (green line) and a Start timing signal (blue line) to the TCSPC. The single photon detector provides the stop (orange line). Relative timings are collected on histograms like (1-4), with increasing acquisition time. The longer the acquisition time (4), the better the profile accuracy of the timing reference.

In modern TCSPC hardware, a Time to Digital Converter (TDC) replaces the TAC. In its simplest version, the TDC acts as a clock attached to a counter; from the start signal clock cycles are counted until a stop signal is received and therefore a count can be stored in a bin corresponding to the number of clock cycles. A series of these operations form a histogram of the optical transient of the system (Fig. 3.15).

---

[7] An electronic signal processing device, designed to mimic the mathematical operation of finding a maximum of a pulse by finding the zero of its slope.

Whatever the hardware architecture, a single-photon regime must be guaranteed for every single time-gate. When this condition is not guaranteed, the so-called pile-up effect [23] occurs. Such effect involves photons lost at high photon count rates due to the combined dead time of the detector and TCSPC modules, usually below 100 ns.

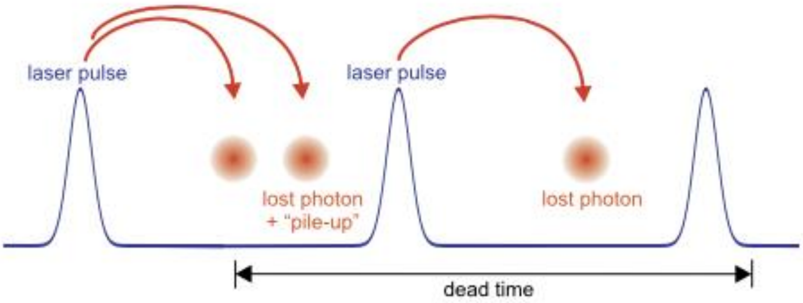

Fig. 3.16: Graphic description of the pile-up effect. The dead time forbids the detection of the second and third photon. Reproduced from [24]

Considering the dead time, single-photon detectors reveal only one photon after one laser shot. Pile-up describes the effects of photons lost at high photon count rates due to the dead time of the TCSPC devices (Fig. 3.16). In consequence, the average measured time becomes shorter.

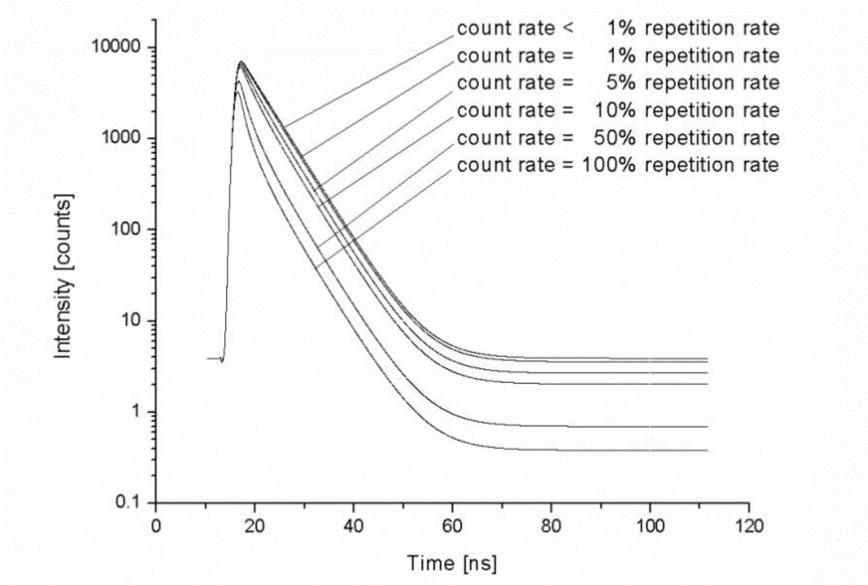

Fig. 3.17: Example of changed lifetime in a Time Correlated Single Photon Counting fluorescence measurement as function of the ratio between detection count rate and the laser repetition rate (Pile-up effect). Reproduced from [24].

A solution to the problem is a proper reduction of the detection rate. Although the measurements start to be substantially altered when the detection rate is around half of the laser rate (Fig. 3.17), most of the TCSPC modules give a warning to the user over a 5% ratio.

As stated in § ***2.1.5***, the dead times and timing delays within the electrical components permit to measurement of a maximum of only one photon, or one Stop per Start pulse. Assuming a Poissonian distribution of the measured data, two figures of merit can be computed on TCSPC histograms: the signal to background ratio (SBR) and the signal-to-noise ratio (SNR).

SBR is the ratio between the number of counts in the maximum bin from a TCSPC histogram (n_p) and the average number of background counts per bin (n_b). Background counts are detection events arising from experimental noise. They are uncorrelated with respect to the trigger signal of the system and are therefore distributed all over the histogram with an equal probability [25]:

$$SBR = {}^{n_p}\!/_{n_b} \qquad \text{(Eq. 18).}$$

Although SBR could be a qualitative indication for a histogram, it does not consider the improvement in response shape with respect to the total acquisition (or integration) time of the histogram [22]. To quantify the level of a signal over a background noise level, it is possible to use the SNR [25]:

$$SNR = {}^{n_p}\!\Big/_{\sqrt{n_b + n_p}} \qquad \text{(Eq. 19).}$$

From Eq. 18 and Eq. 19, it is clear how systems with similar SBR may show a significantly different SNR.

All the TCSPC measurements reported in the thesis were acquired using a multichannel module (Hydraharp 400, PicoQuant GmbH).

3.4 Summary

SNSPDs design, fabrication and testing involve the understanding of several tools and techniques. The results presented in the following chapters required a correct use of the electron beam lithography, dry etching and metal deposition facilities. At the same time, a 2.4 K GM cryostat was successfully assembled and setups for the electrical, optical and timing characterizations were employed, discussing also time-correlated single-photon counting technology in depth.

References

[1] Ohring, M. (2001). Materials science of thin films. Academic press.

[2] Lin, Y., & Chen, X. (Eds.). (2016). Advanced Nano Deposition Methods. John Wiley & Sons.

[3] George, S. M. (2010). Atomic layer deposition: an overview. Chem. Rev, 110(1), 111-131.

[4] Meyerson, B. S. (1986). Low-temperature silicon epitaxy by ultrahigh vacuum/chemical vapor deposition. Applied Physics Letters, 48(12), 797-799.

[5] Campbell, S. A. (1996). The science and engineering of microelectronic fabrication. Oxford University Press, USA.

[6] Chang, T. H. P. (1975). Proximity effect in electron-beam lithography. Journal of vacuum science and technology, 12(6), 1271-1275.

[7] Sugawara, M. (1998). Plasma etching: fundamentals and applications (Vol. 7). OUP Oxford.

[8] Flynn, T. (2004). Cryogenic engineering, revised and expanded. CRC Press.

[9] Radenbaugh, R. (2004). Refrigeration for superconductors. Proceedings of the IEEE, 92(10), 1719-1734.

[10] de Waele, A. T. (2011). Basic operation of cryocoolers and related thermal machines. Journal of Low Temperature Physics, 164(5), 179-236.

[11] Orgiazzi, J. L. F. X., & Majedi, A. H. (2009). Robust packaging technique and characterization of fiber-pigtailed superconducting NbN nanowire single photon detectors. IEEE Transactions on Applied Superconductivity, 19(3), 341-345.

[12] Kerman, A. J., Dauler, E. A., Keicher, W. E., Yang, J. K., Berggren, K. K., Gol'Tsman, G., & Voronov, B. (2006). Kinetic-inductance-limited reset time of superconducting nanowire photon counters. Applied physics letters, 88(11), 111116.

[13] Cho, S. (1997). Temperature and current dependence of inductance in a superconducting meander line. Journal of the Korean Physical Society, 31(2), 337-341.

[14] Kerman, A. J., Dauler, E. A., Yang, J. K., Rosfjord, K. M., Anant, V., Berggren, K. K., *et al.* & Voronov, B. M. (2007). Constriction-limited detection efficiency of superconducting nanowire single-photon detectors. Applied Physics Letters, 90(10), 101110.

[15] Hadfield, R. H. (2009). Single-photon detectors for optical quantum information applications. Nature photonics, 3(12), 696-705.

[16] Radebaugh, R. (2000). Development of the pulse tube refrigerator as an efficient and reliable cryocooler. Proceedings of Institute of Refrigeration, London, UK.

[17] Heath, R. M., Tanner, M. G., Casaburi, A., Webster, M. G., San Emeterio Alvarez, L., Jiang, W. *et al.* & Hadfield, R. H. (2014). Nano-optical observation of cascade switching in a parallel superconducting nanowire single photon detector. Applied physics letters, 104(6), 063503.

[18] http://www.attocube.com/nanoPOSITIONING/ANSxy100/Specifications_ANSxy100.pdf

[19] http://www.thorlabs.de/catalogpages/v21/731.pdf

[20] http://www.thorlabs.de/catalogpages/v21/720.pdf

[21] Vojnovic, B. (2006). Advanced Time-Correlated Single Photon Counting Techniques. Journal of Microscopy, 222(1), 65-66.

[22] Krichel, N. J., McCarthy, A., & Buller, G. S. (2010). Resolving range ambiguity in a photon counting depth imager operating at kilometer distances. Optics express, 18(9), 9192-9206.

[23] Arlt, J., Tyndall, D., Rae, B. R., Li, D. D. U., Richardson, J. A., & Henderson, R. K. (2013). A study of pile-up in integrated time-correlated single photon counting systems. Review of Scientific instruments, 84(10), 103105.

[24] http://www.tcspc.com/doku.php/glossary:pile-up_effect

[25] Pellegrini, S., Buller, G. S., Smith, J. M., Wallace, A. M., & Cova, S. (2000). Laser-based distance measurement using picosecond resolution time-correlated single-photon counting. Measurement Science and Technology, 11(6), 712.

Chapter 4 – Superconducting nanowires single-photon detectors arrays

This chapter illustrates results about fabrication and testing of two 4-pixels superconducting nanowires single-photon detectors arrays having sensitive area of 30 x 30 µm^2 and 60 x 60 µm^2, with an individual pixel bias and readout scheme[1]. Furthermore, a code-division multiplexing scheme based on the integration between the superconducting nanowires and on-chip palladium resistors was simulated.

4.1 Large area SNSPD-arrays design

The two arrays under investigation have the same design with a 2x2 matrix of independent pixels covering sensitive areas of 60 x 60 µm^2 and 30 x 30 µm^2. As the pixels are identical, the area of a single detector is 30 x 30 µm^2 and 15 x 15 µm^2, respectively. Coplanar waveguides (CPW), as thick as the nanowires are, act as transmission lines delivering signals from the chip to the external electronics (Fig 4.1).

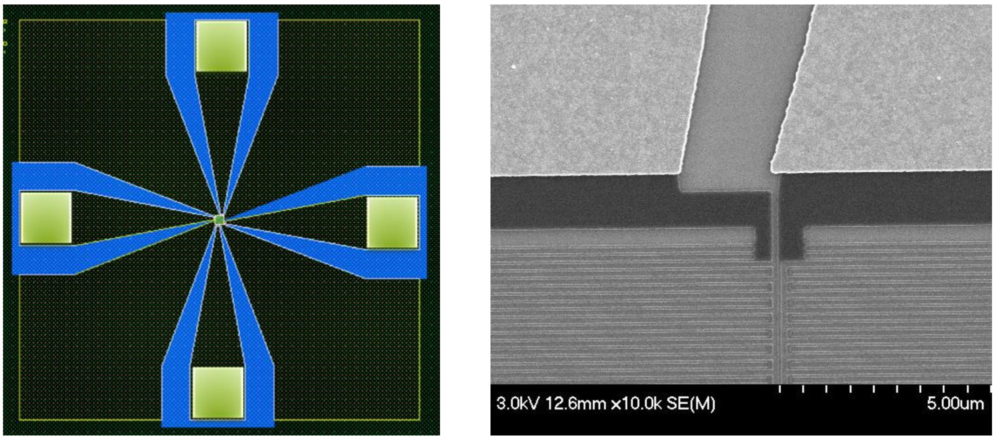

Fig 4.1: On the left, waveguides layout (in blue) around the 4 pixels for a positive resist. On the right, SEM image of a waveguide-chip connection.

The widths of the ground plane spacing in the CPW (Fig. 4.2) are a function of the thickness and the permittivity of the substrate, the frequency of the electrical signal (~2 GHz) to be carried, the trace width (typically as large as the size of the detector) and the connection impedance (50 Ω).

---

[1] Work carried out in collaboration with Dr. Alessandro Casaburi.

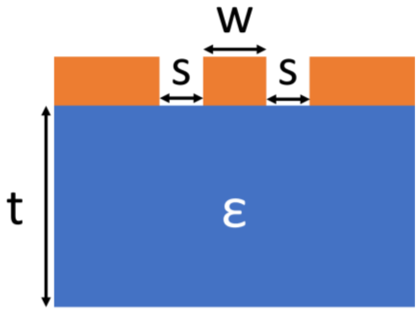

Fig 4.2: Main parameters for the computation of the coplanar waveguide ground plane spacing (s). The space is a function of the trace width (w), the substrate thickness (t) and permittivity (ε), the connection impedance (usually 50 Ω) and the frequency of the electric signal (~2 GHz).

With the help of an external tool[2], a trace width of ~8.5 µm was computed. The big square (400 µm x 400 µm) at the end of the guide (Fig. 4.1) is necessary for a comfortable wire-bonding between the chip and the sample mount. The presence of such bond-pads requires the computation of a a second trace width of ~215 µm, using the same tool. The mismatch between the different sizes at the beginning and at the end of the CPW gets tapered by a link of ~1.4 mm [1]. Such link is kept quite long to avoid fabrication issue related to small features that may result into a faulty (open circuit) CPW.

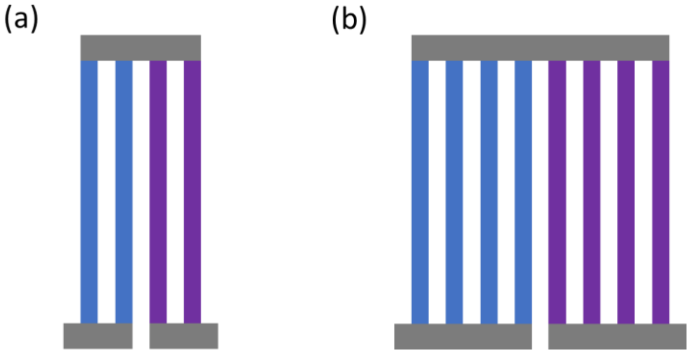

Fig 4.3: Parallel configuration used for the nanowires in each single pixel: 46 blocks connected in series each containing 2 parallel nanowires in the 30 x 30 µm^2 array (a) and 4 parallel nanowires in the 60 x 60 µm^2 array (b).

Both the arrays adopt a configuration of 46 blocks, connected in series. Each block contains a parallel of two nanowires, in the 30 x 30 µm^2 array (Fig. 4.3a), and a parallel of four nanowires, in the 60 x 60 µm^2 array (Fig. 4.3b). As reported in § ***2.4.5***, some reasons suggested to employ parallel nanowires rather than a meander: firstly, a single defect, in terms of fabrication, for a long meander can spoil the detection

---

[2] http://www1.sphere.ne.jp/i-lab/ilab/tool/cpw_e.htm

efficiency of the entire device; secondly, there is a linear decrease of the maximum photon counting rate, due to a dead time proportional to the kinetic inductance [2].

In the 30 x 30 µm^2 array, the nanowires are 60 nm wide and 90 nm spaced, patterned from an 8 nm NbTiN film (film growth: STARCryo, USA) deposited on a basic cavity layer of 400 nm SiO_2, while the wafer is made of Si (Fig. 4.4a). The refractive index mismatch at the Si/SiO_2 interface gives a strong reflection and the optical length[3] of the basic cavity is ~580 nm. Hence, consequently to the quarter-wave resonance, this substrate was optimized for incident wavelengths around 2.2 µm.

In the 60 x 60 µm^2 array, the nanowires are 70 nm wide and 90 nm spaced, patterned from a 6 nm NbTiN film (film growth: JWNC, University of Glasgow) deposited on a distributed Bragg reflector (DBR, layers growth: Helia Photonics Ltd) and a Si substrate. In details, 5 bi-layers of Si/SiO_2, whose thickness is 270 nm Si and 270 nm SiO_2 are deposited on top of the Si substrate (Fig. 4.4b). The top SiO_2 layer is a quarter-wave cavity with an optical length of ~391 nm and optimized for incident wavelengths in the interval 1.3-1.9 µm.

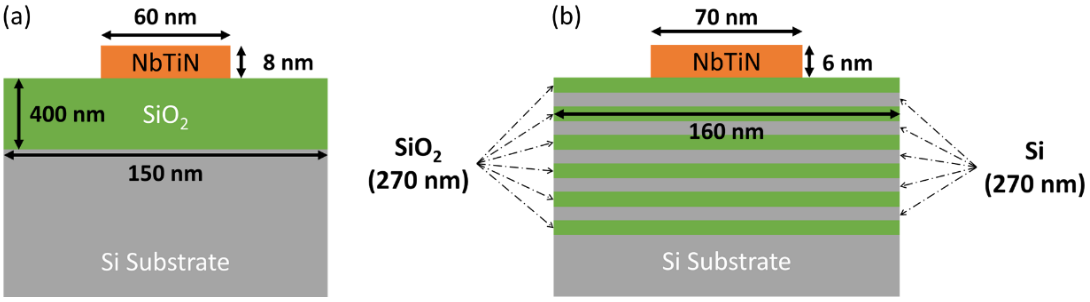

Fig 4.4: Structure, not to scale, of the detector in the 30 x 30 µm^2 array (a) and in the 60 x 60 µm^2 array (b).

4.2 Large area SNSPD-arrays fabrication

4.2.1 Markers

Initial and essential step of fabrication is the deposition of Titanium-Gold (Ti-Au) markers for the alignment of the VB6 machine (described in § ***3.1.2***). To do that, few drops of resist are pipetted onto the microchip after a cleaning with acetone, isopropanol (IPA) and a nitrogen gun. The resist used is the ZEP520A[4].

---

[3] Product of the thickness and the index of refraction of the medium through which photons at a specific wavelength propagate.

[4] The use of a positive tone resist influenced the layout design.

Afterward, the microchip runs in a spinner at 4000 rpm for 60 s, distributing the resist all over the surface of the sample which is then baked on a hotplate at 180 °C for about 4 minutes. It comes now the time for a first electron beam lithography (EBL) exposure. At these stage, the electron dose given is 220 µC/cm^2, the spot size is 45nm, the current of the electron beam is 100nA, the resolution is 1.25 nm and the variable resolution unit (VRU) is 43. The ZEP520A resist protects the unexposed areas of the chip, where the Ti-Au bi-layer will be deposited after the development of the samples. This is possible by putting the chip in a beaker with O-Xylene, used to develop the resist, for 60 s at 23 °C and soon after in another beaker with IPA at room temperature for 40 s that stops the action of the O-Xylene.

Then the sample is ready to be processed by a metal deposition machine. A thin Ti layer of 15 nm underneath is better in terms of adhesion than the sole 65 nm Au layer. Furthermore, the remaining resist and metal above gets removed by soaking the sample for several hours inside a beaker filled with Shipley 1165 remover solvent (also called “stripper”), placed in a thermal bath at ~50 °C. That beaker then goes into an ultrasonic bath and a new acetone/IPA wash will clean the unwanted features from the surface.

The number of markers depends on how many steps the fabrication requires. Every step needs a primary marker, a cross of 400 µm span, to locate the subdomain of the secondary markers: a group of four squares of 20 µm x 20 µm. Four markers alignment removes offset, scale, rotation and keystone errors (Fig 4.5).

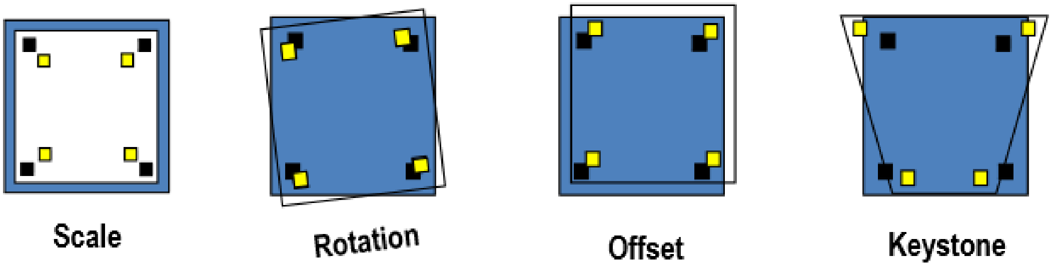

Fig 4.5: Errors related to markers misalignment in nanofabrication. Courtesy of Dr. S. Thoms.

4.2.2 Patterning and etching

Once the sample contains markers, it is possible to the pattern the nanowire. The required settings for the EBL tool are sensibly different. The dose for NbTiN patterning is 200 µC/cm^2. The spot size is 4nm with an electron beam current of 1nA (the finest available) and the VRU is 3.

Once this lithographic mask is completed, the sample is ready to be dry-etched (see § ***3.1.3***). The utilized gas is CF$_4$. The parameters needed to etch the NbTiN film are:

- gas flow (50 sccm);
- RF power (80 mW);
- gas pressure (30 mT);
- time of etching (variable, but usually no longer than 50 seconds).

4.2.3 Device finalization

The operation following a dry-etching is the removal of the remaining resist by soaking again the sample in the stripper, leaving the superconducting nanowires exposed.

The final step[5] is the deposition of the bond-pads (ground and CPW) made of Ti-Au and therefore processed in analogy with § ***4.2.1***. The sample is ready (Fig. 4.6) to be packaged as described in § ***3.2.3***.

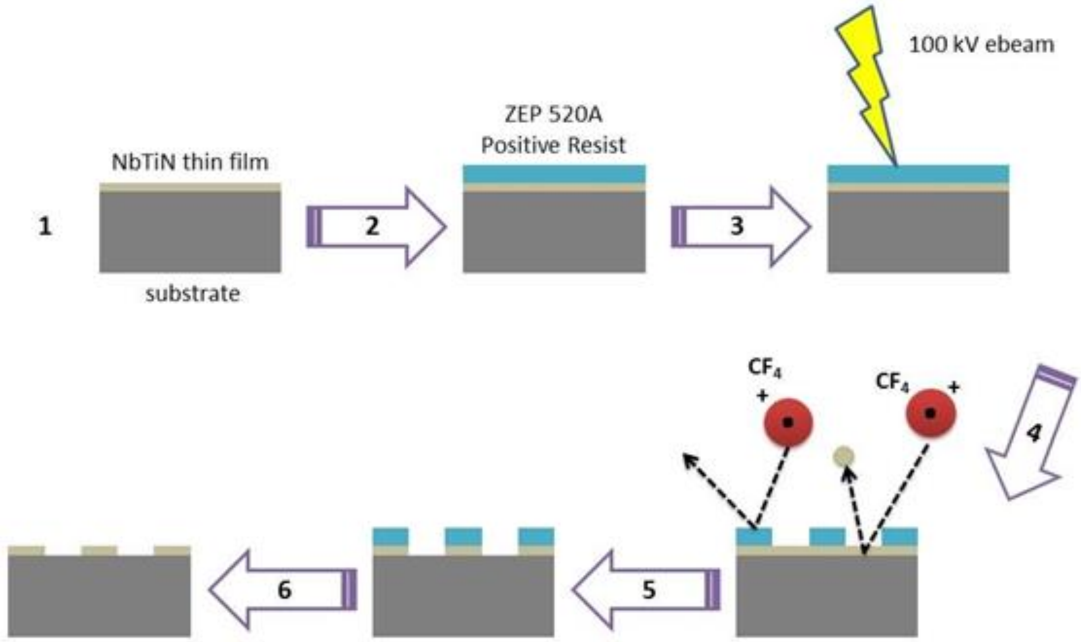

Fig 4.6: Nanowires fabrication diagram. 1) Growth of thin films over the substrate. 2) Application of a positive resist. 3) The pattern is written into the resist by electron beam lithography. 4) Dry-etching of unprotected areas of NbTiN with CF$_4$. 5) Application of a stripper to remove the residual resist. 6) Device patterned.

---

[5] To be precise, in the 30 x 30 µm^2 array, markers and bond-pads were processed together at the beginning of the fabrication-batch. In the 60 x 60 µm^2 array, CPW and ground bond-pads were processed after the dry-etch in order to differentiate the thickness of the layers.

4.3 30 x 30 µm^2 array characterization

4.3.1 Electrical characterization

The resistance of the four pixels was measured, at room temperature, via a digital multimeter, obtaining values in the range 1.51-1.52 MΩ.

After a cooldown to ~3.6 K in a closed-cycle pulse-tube (PT) refrigerator [3], a critical temperature (T_c) of 7.7 K and a uniform critical current (I_c) of 38 µA, for all the pixels, was observed (Fig. 4.7a).

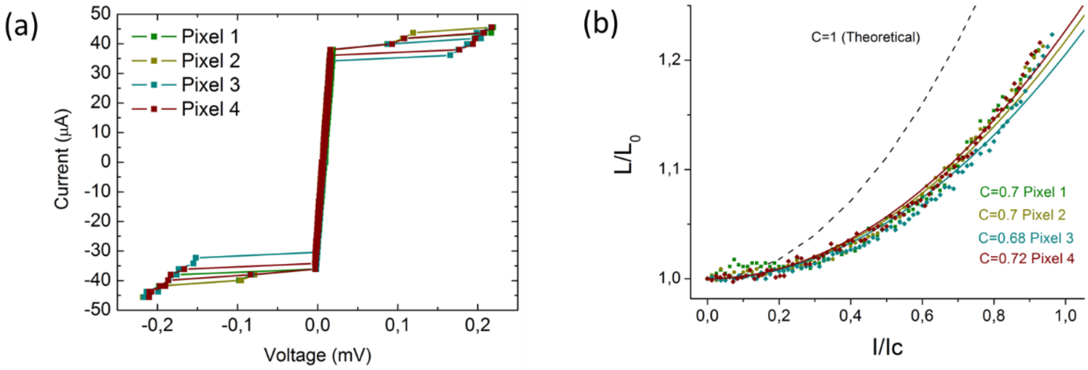

Fig 4.7: Electrical characterization, at 3.5 K, of the 30 x 30 µm^2 array. (a) *I-V* characteristic for the four pixels showing a critical current (I_c) of 38 µA. (b) Inductances for the four pixels normalized at the value of L_0 (Eq. 16), at varying of the bias current normalized at the critical value. The L/L_0 curves were fitted as explained in § *3.3.2*. In the figure is also shown the theoretical curve (dashed line) for C = 1 (i.e. nanowires with no constriction).

A further proof of uniformity comes from the *L-I* curves (Fig 4.7b). The obtained value of C (see § ***3.3.2***) ranged between 0.68 (*pixel 3*) and 0.72 (*pixel 4*) showing a high degree uniformity of nanowire cross-section in the fabrication. These values are almost close to the theoretical value of C = 1 for nanowires with no constriction and it is reasonable to think that the discrepancy could be mainly due to the non-uniformity of the film thickness, including potential bumps in the substrate, instead of the constriction of the nanowire width in the fabrication. In fact, for C of about 0.7, a variation in the nanowire width of 15-20 nm should be clearly recognizable.

But from extensive SEM[6] inspection (Fig. 4.8) of the devices none of such errors were observed. This suggests that such constrictions result either from thickness variations or material defects, which may have been present in the film before patterning, and may even be due to defects present in the substrate itself before film growth.

---

[6] Scanning Electron Microscope

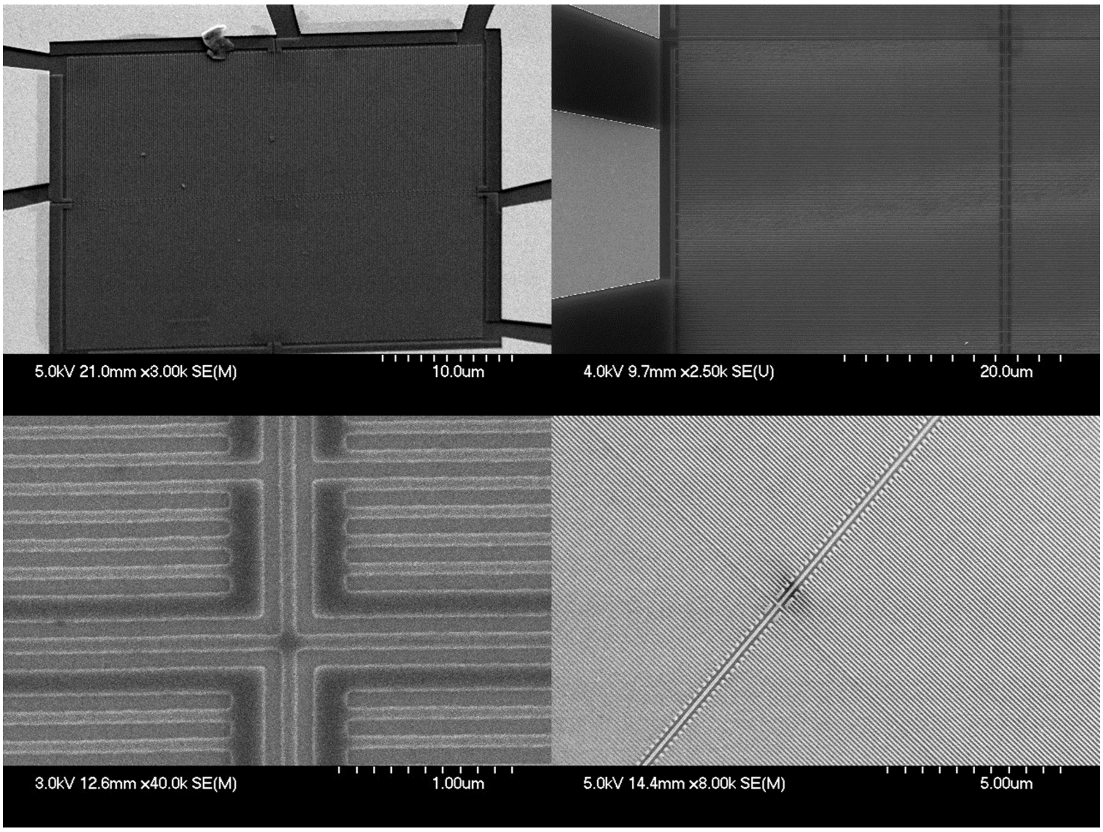

Fig 4.8: SEM inspection of the 30 x 30 μm^2 array.

4.3.2 Optical characterization

The optical characterization setup is a revision of the one described in § ***3.3.4***. Bias current (I_b) and signal pulse readout for each of the four pixels was performed using a bias tee. The signal-pulses from the four RF arms of the bias tee were amplified using an amplifier (LNA-1000, RF Bay Inc.) with a total gain of 33dB. Then the pulses were sent to a power combiner (804-2-0.600-M01, MECA Electronics Inc.) which was connected to a second amplifier (LNA-580, RF Bay Inc.) with a gain of 23dB, for a total gain of 56dB (Fig. 4.9).

The role of the 4-to-1 power combiner, running at 500 MHz, is to switch the delivery of the four input signals toward the output port, providing a Time Division Multiplexing (TDM, explained in § **2.2**).

The pulses then were sent to a digital counter (Agilent 5313A) or an 8 GHz bandwidth oscilloscope (Agilent Infiniium DSO80804A), depending on the test to execute.

Following the procedure explained § ***3.3.3***, the count rate as function of the photon flux generated by the 1550nm laser for different bias voltage was measured, in order to compute detector efficiency and dark count rate (DCR) for all the four pixels in the array (Fig. 4.9).

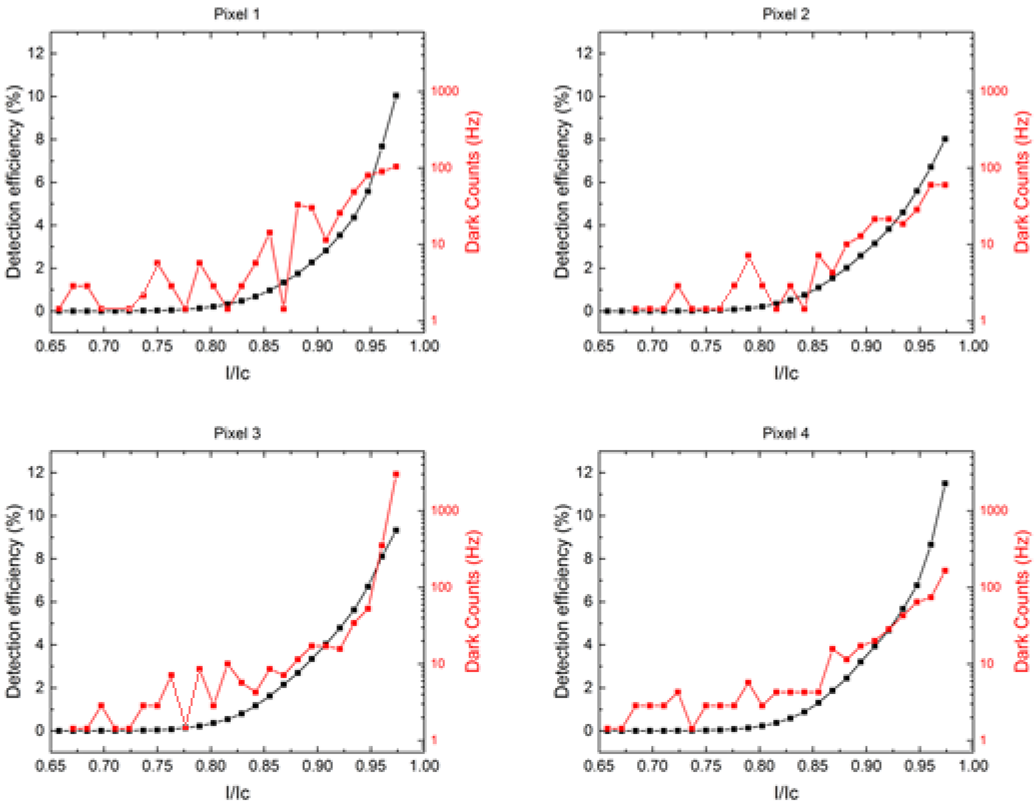

Fig 4.9: Detection efficiency (1550 nm wavelength, pulsed at 1 MHz) and dark count-rate as a function of the normalized bias for the four pixels in the 30 x 30 μm^2 array.

Biased at the highest value (97% of I_c) the detector shows detection efficiencies from ~8% (*pixel 2*) to ~11.5% (*pixel 4*). As the DCR is of the order 100 Hz (except for ~3 KHz measured on *pixel 3*), it is reasonable to conclude that the detection efficiencies are mainly limited by the lack of an optical cavity optimized at 1550 nm wavelength.

After the single-pixel efficiencies, an array count map was obtained by scanning the 1550 nm laser spot across the entire device (Fig. 4.10). The employed laser is characterized by a pulse duration of 5 ns, a power of 1 µW (attenuated by 60 dB) and a repetition rate of 1 Mhz. The input light-beam for this characterization contained ~7.5 photons per pulse. However, there are losses through the fibre connections in the cryostat of the order of 2dB (measured via an optical power-meter). This characterization shall be considered a response map (rather than an efficiency map) and confirms how the nanowire uniformity is good across the whole sensitive area of the array, even close to the edges. The four pixels were biased individually at the 95% of the I_c. The region between the pixels (green) includes a nanowire, 150 nm wide, connecting the electrical ground of the four pixels (common ground configuration), providing also a sensitive area with a smaller efficiency.

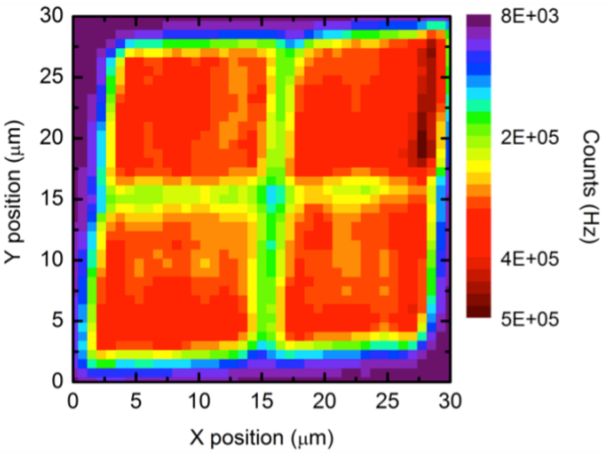

Fig 4.10: SNSPD array count map obtained by scanning the laser spot across the 30 x 30 µm^2 device area. The map was acquired at 3.5 K, the device was operated at the 95% of the critical current. The 1 µW power laser pulses (5 ns duration, 1 MHz repetition rate) were attenuated by 60 dB.

By positioning the laser on the centre of the array and defocusing the laser spot just before the counts start to decrease (laser spot size a bit smaller than the sensitive area of the SNSPD array), the overall system detection efficiency (SDE) and the associated DCR of the array were measured (Fig. 4.11). The maximum value measured are a 2.6% SDE and a DCR of ~300 Hz, at 97% of the I_c.

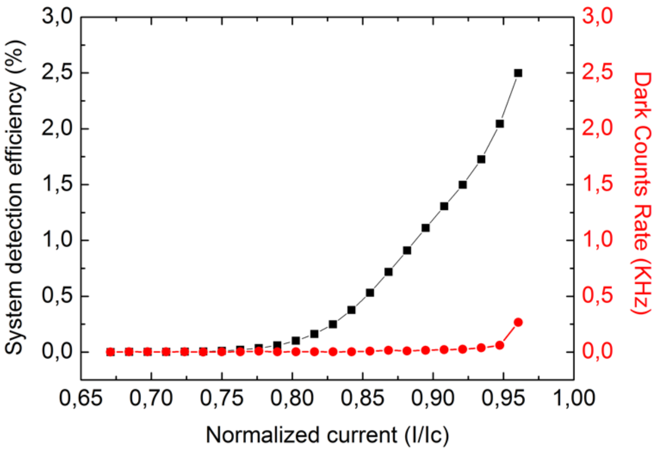

Fig 4.11: Overall system detection efficiency (black squares) and the relative dark counts (red circles) at the varying of the normalized bias current.

By leaving the laser spot in the same position used for the efficiency measurements, the time jitter histograms (§ ***3.3.5***) for every pixel, biased at the same time, were measured (Fig. 4.12). The histograms were acquired using a multichannel TCSPC module with 1 ps bin width. All the pixels responded with a Gaussian shape with no asymmetric tails and the values of the respective FWHM is in the range of 71-72 ps at the 97% of the I_c (Fig 4.12). This is another proof of the device uniformity.

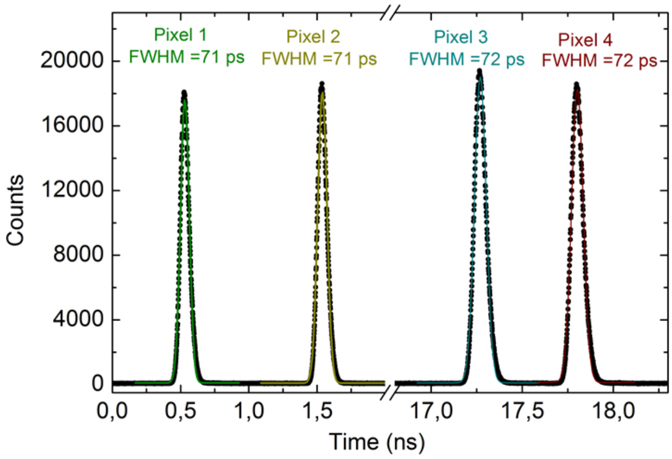

Fig 4.12: Timing jitter histogram measured for the four pixels in the 30 x 30 μm^2 array biased at the 97% of the critical current.

The variation of the maximum peak position and FWHM of the time jitter histograms at varying of I_b was also investigated (Fig. 4.13). The peak position shifts towards smaller times and the FWHM of the peak decreases at increasing of I_b. Likewise, no significant change (asymmetry) in the shape of the Gaussian peak was noticed.

All these observations match with other results reported in literature [4].

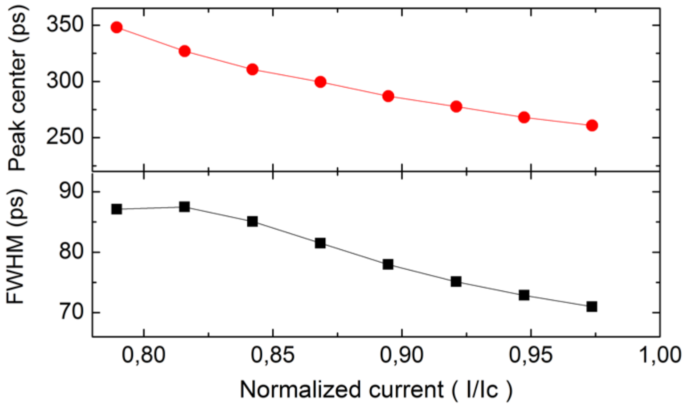

Fig 4.13: Position of the maximum of the histogram (red circles) and the FWHM (black squares) of the histogram with varied bias current when only pixel number one is biased.

4.4 60 x 60 μm^2 array characterization

4.4.1 Electrical characterization

At room temperature and on a digital multimeter, the 60 x 60 μm^2 array showed resistance values of 1.76-1.78 MΩ. After a cooldown to ~3.6 K in the same PT cryostat, a T_c of 6.7 K and critical currents from 40 μA (*pixel 2*) to 49 μA (*pixel 3*, *4*) were observed (Fig. 4.14a).

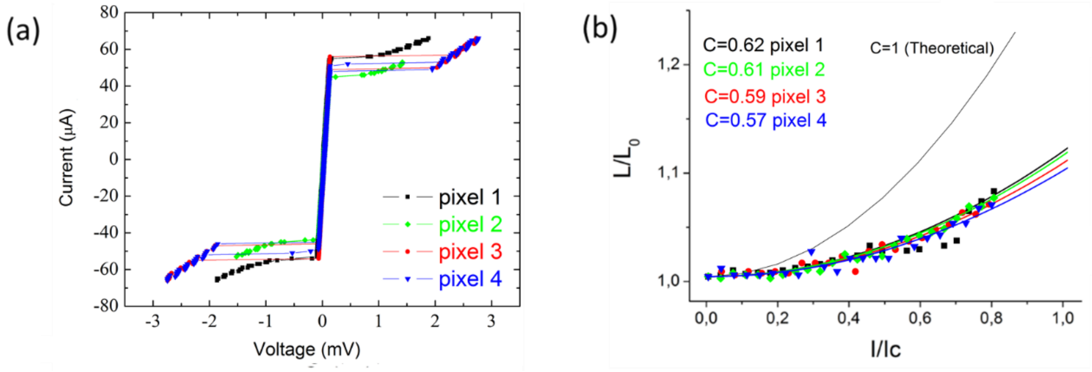

Fig 4.14: Electrical characterization, at 3.5 K, of the 60 x 60 µm^2 array. (a) *I-V* characteristic for the four pixels, showing critical currents from 41 to 51 µA. (b) Inductances for the four pixels normalized at the value of L$_0$ (Eq. 16), at varying of the bias current normalized at the critical value. The L/L$_0$ curves were fitted as explained in § *3.3.2*. In the figure is also shown the theoretical curve (dashed line) for C = 1 (i.e. nanowires with no constriction).

The obtained value of C (see Eq. 16) ranged between 0.57 and 0.62 (Fig. 4.14b). Although representing a good uniformity in terms of fabrication, the values are lower than the kinetic inductance of the previous array (a difference of ~0.1) and thus farer from the optimal value of C = 1. As the device, during a SEM inspection (Fig. 4.15), appeared uniform in terms of nanowire width, such result should depend again on a not uniform film thickness, bumps in the substrate or material inhomogeneity.

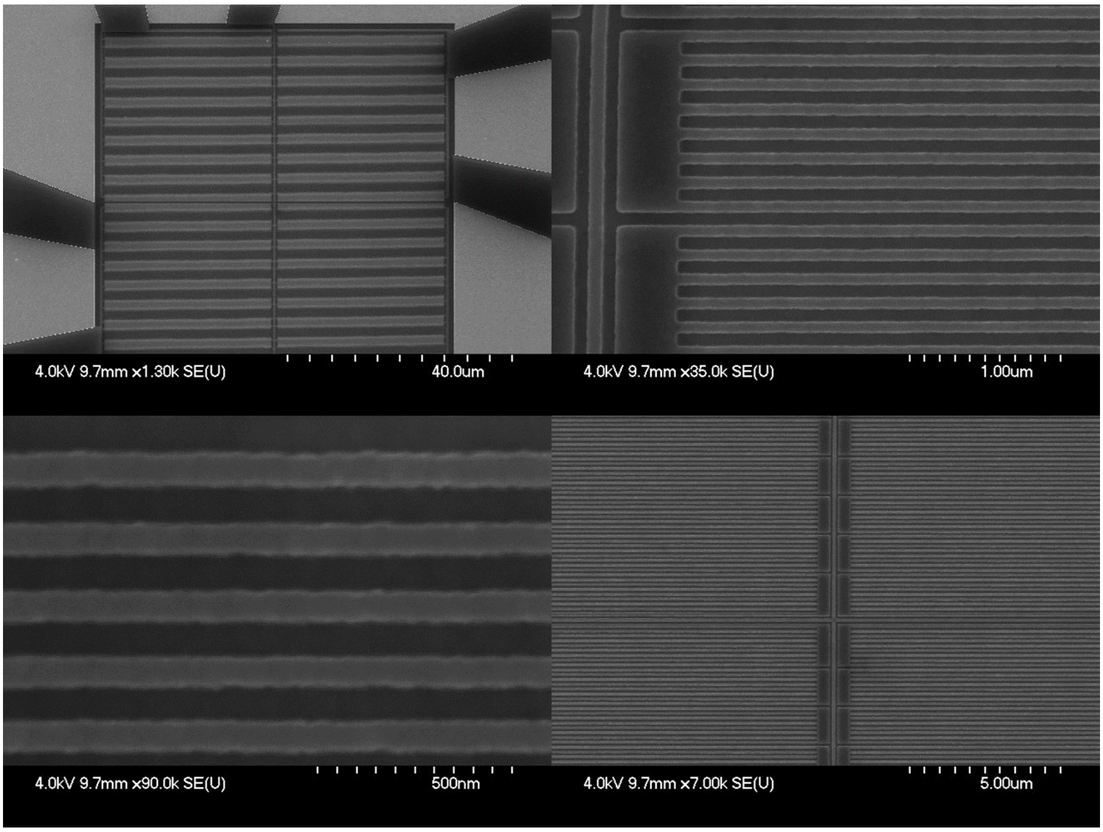

Fig 4.15: SEM inspection of the 60 x 60 µm^2 array.

4.4.2 Optical characterization

Biased at the highest value (97% of I_c) the detector showed detection efficiencies from ~9% (*pixel 2*) to ~25% (*pixel 1* and *4*). It is consistent with the measurements of the critical currents, as I_c for *pixel 2* is about 9 µA lower than the other pixels (Fig. 4.14a). At the same bias, the DCR is quite uniformly of the order 10 kHz (Fig. 4.16).

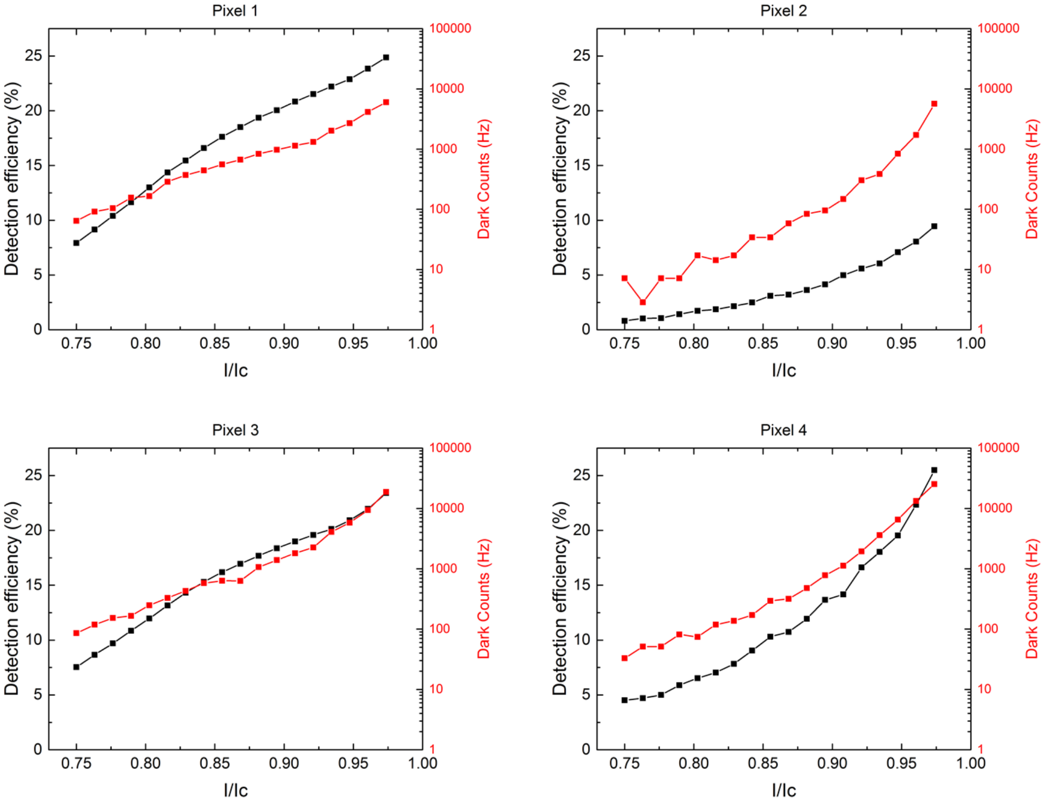

Fig 4.16: Detection efficiency (1550 nm wavelength, pulsed at 1 MHz) and dark count-rate as a function of the normalized bias for the four pixels in the 60 x 60 µm^2 array.

An array count map, scanning the 1550 nm laser spot across the entire device, was performed on this array too. Although responding all over the active area, the array shows an inhomogeneous count rate (Fig. 4.17), showing its peak response only near the centre of the X axis.

The timing jitter histograms were measured, as described in § ***4.3.2***. All the pixels responded with a Gaussian shape, but asymmetric tails were noticed in *pixel* 1 and 4. The values of the respective FWHM varies from 116 to 163 ps at the 97% of I_c (Fig. 4.18).

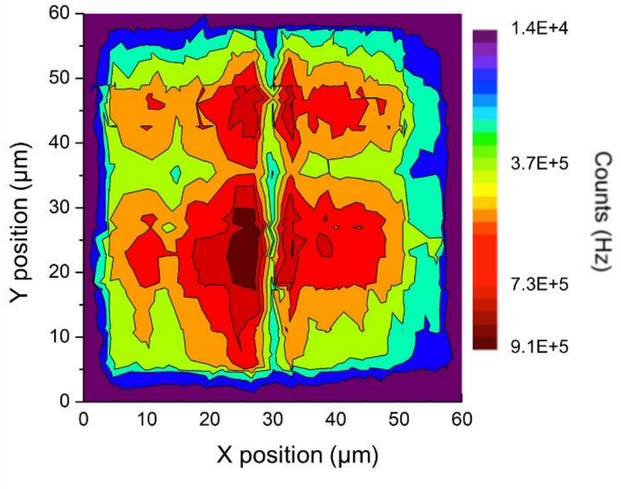

Fig 4.17: SNSPD array count map obtained by scanning the laser spot across the 60 x 60 µm^2 device area. The map was acquired at 3.5 K, the device was operated at the 95% of the critical current. The 1 µW power laser pulses (5 ns duration, 1 MHz repetition rate) were attenuated by 60 dB.

In conclusion, the use of an optimized optical cavity at 1550 nm enhanced the detection efficiency of this array of about a factor 3, compared to the 30 x 30 µm^2. However, the 60 x 60 µm^2 array showed less uniformity, perceptible by the jitter measurements and the scanning map.

As the two detectors were fabricated on different substrates and films, it is reasonable to state that such issues are not related to the fabrication process but rather to inhomogeneous surfaces (non-optimized NbTiN film and bumps over the Si substrate).

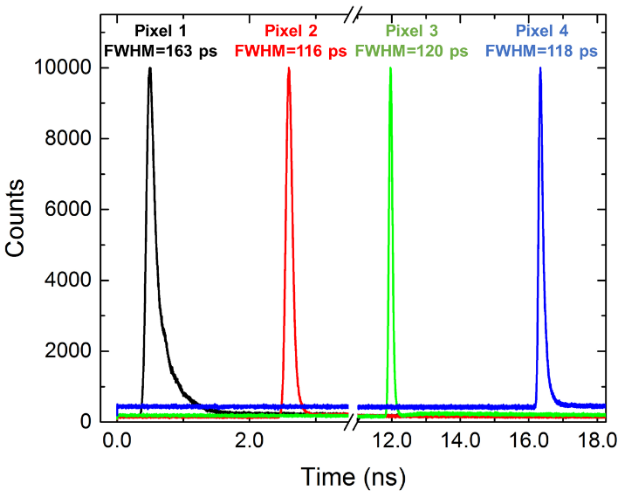

Fig 4.18: Timing jitter histograms measured for the four pixels in the 60 x 60 µm^2 array biased at the 97% of the critical current.

4.5 On-chip code-division multiplexer for SNSPDs

4.5.1 Electrical equivalent circuit of an SNSPD

An SNSPD equivalent electric circuit (Fig. 4.19) can be modelled by few components. The kinetic inductance can be represented by an inductor L_k, which depends on the geometry and the materials of the nanowire. The hotspot resistance (see § ***2.4.5***) can be represented by a resistor R_n that depends on the material, but generally of the order few kΩ. A DC-current generator represents the bias (I_b) of the pixels with a shunt resistor in parallel (R_S). The photo-absorption can be simulated by a voltage controlled switch: in the superconducting state, it is closed and the signal bypasses R_n while in the normal states the switch is open. R_n is now part of the circuit, creating a parallel with the load impedance Z_0 at 50 Ω, where most of the signal is diverted. As every LR circuit, during a fall-time constant τ_{fall} = $L_k/(R_n + Z_0)$, I_b decays through the nanowire; τ_{fall} also limits the rise time of the voltage pulse across Z_0. At this stage, the current reaches the so-called return value I_r [2] and it increases up to its critical value I_c in a rise-time constant τ_{rise} = L_k/Z_0, due to the disappearance of the resistive hotspot.

Those time constants are mirrored at the oscilloscope when one observes the voltage output pulses generated across Z_0: a current fall-time corresponds to a pulse rise-time and vice versa.

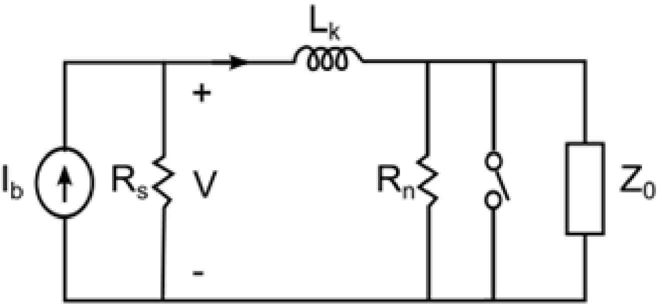

Fig 4.19: Equivalent electrical circuit of a superconducting nanowire.

The electrical responses of an SNSPD can be effectively modelled by using four elements on SPICE[7] software:

- an inductor representing the kinetic inductance (Fig. 4.20/L1) of the nanowire;
- a voltage source used as ammeter (Fig. 4.20/V2) (required by SPICE for the current readout);

---

[7] Simulation Program with Integrated Circuit Emphasis

- a current-controlled switch (Fig. 4.20/W1) simulating the transition from the normal state to the superconducting state and vice versa when I_b overcomes the critical current of the nanowire;
- a voltage-controlled switch (Fig. 4.20/S3) driven by a time triggered voltage source (Fig. 4.20/V1) simulating the impinging photon that generates the hotspot formation.

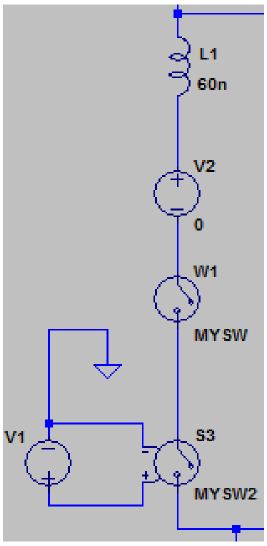

Fig 4.20: Equivalent SPICE circuit of a superconducting nanowire.

4.5.2 Simulated 4-pixel code-division multiplexing scheme

As already mentioned in *Chapter 2* and *Chapter 3*, every current signal deriving from a photo-detection by an SNSPD passes through a resistor to be converted in a voltage pulse. If the output resistor is shared by all the pixels on the SNSPD, there will be a single readout pulse whose amplitude is proportional to the number of detected photons. Such idea was already exploited for PNR purposes (see § ***2.1.6***).

A further resistor is integrated on-chip and in parallel with each pixel of the SNSPD [5]. Successful schemes arrived to include up to 24 pixels [6]. However, such devices should not be considered multiplexed arrays because a firing pixel is spatially undistinguishable over the entire detector and this is due to the equality of all the resistors integrated. Thus, different resistors would offer a different voltage output for the same current input. Hence, in theory, it possible to define a code-division multiplexed SNSPD array, in which the channel-code is represented by the amplitude of the output voltage pulse.

In order to simulate a complete device, additional elements are introduced (Fig. 4.21):

- an equivalent bias-tee formed by an 8 mH inductor and a 20 nF capacitor[8];
- a 50 Ω output impedance;
- a 1 Ω resistor, simulating the wiring resistivity;
- a current generator formed by a DC voltage source in series with a 1 MΩ resistor, representing the bias. In practice, an arbitrary I_c (here 15 μA) is uniformly assigned to the circuit but the same current-value is set for the current-controlled switch in each pixel. Hence the simulation runs in terms of normalized bias currents (here set at 100%).

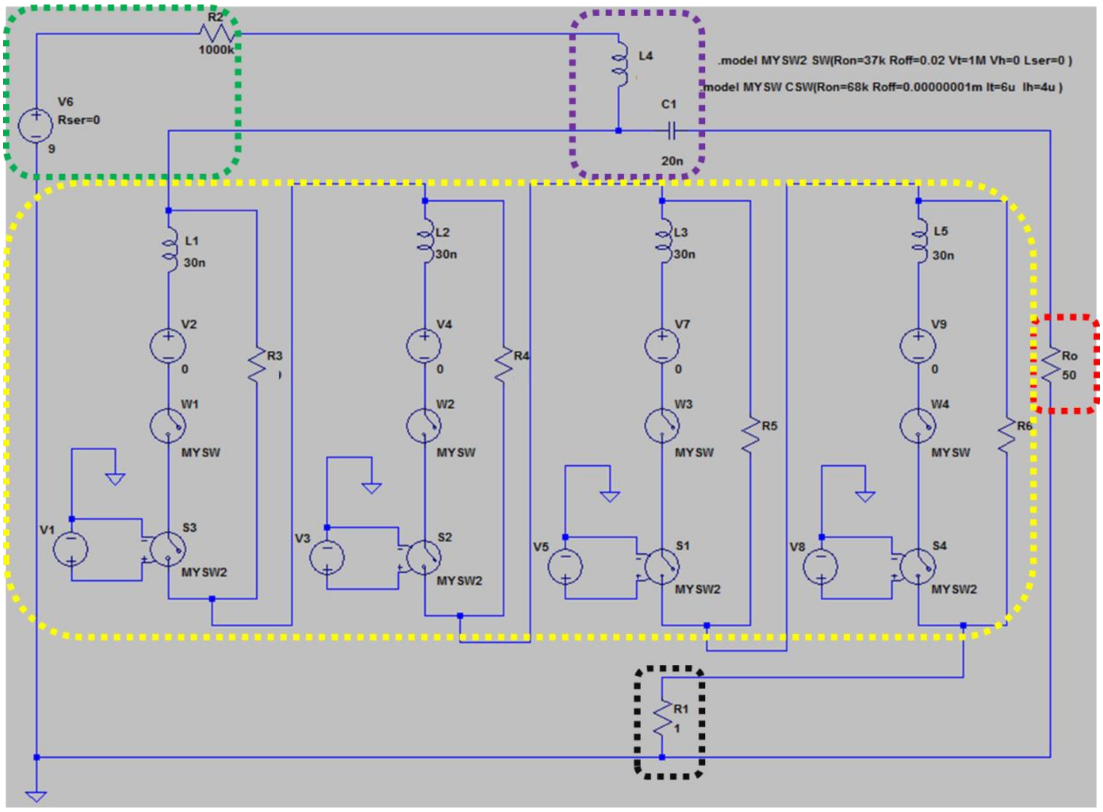

Fig 4.21: Full simulated SPICE schematic of a 4-pixel detector with integrated parallel resistors. Circled in green: bias current generator. Circled in purple: bias tee. Circled in yellow: 4 SNSPDs in series with a different resistor in parallel each. Circled in black: 1 Ω wiring resistivity. Circled in red: 50 Ω output impedance.

The SNSPD pixels were all characterized by a kinetic inductance of 20 nH. Such value was selected in agreement with experimental data available in the research group (~116 pH/sq). The kinetic inductance however will affect the timing of the response but timing has a secondary importance in the proposed simulation.

---

[8] From the Model-5575A datasheet, Picosecond Pulse Labs.

The crucial elements in the design are the resistors. They shall be different enough to produce distinguishable pulses for the readout electronics.

In agreement with all the assumptions above, four SNSPDs were simulated triggering (after 20 ns each, with ideal rise time and fall time of 1 ps). The four resistors in parallel are respectively 60 Ω, 500 Ω, 850 Ω and 2.3 kΩ and produced voltage output pulses of ~90 µV, ~150 µV, ~280 µV and ~390 µV respectively (Fig. 4.22). Such voltage amplitudes do not include the usual ~50dB amplification of the SNSPDs testing setup.

In conclusion, the simulations confirm how the output pulses of four SNSPDs in series (i.e. a 4-pixel array) can be differentiated (of at least 60 µV, without additional amplification) by the insertion of four resistors, each one in parallel with a pixel.

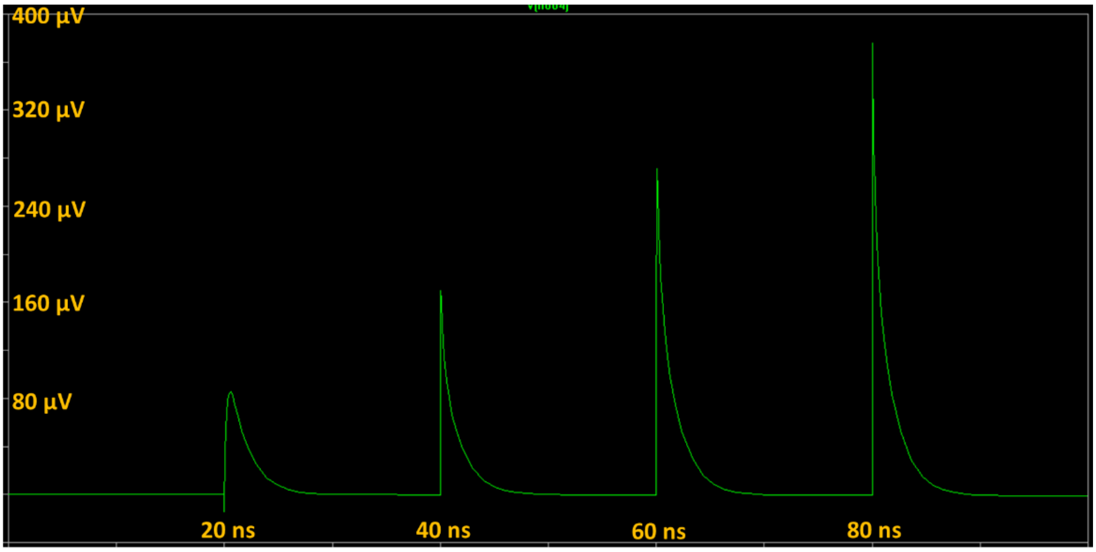

Fig 4.22: Simulated voltage output pulses of a 4-pixels SNSPD with integrated parallel resistors of 60 Ω, 500 Ω, 850 Ω and 2.3 kΩ, separately triggered every 20 ns.

4.5.3 Progresses toward the fabrication

Palladium (Pd) was immediately considered as an appropriate metal for the resistors. It is not superconducting and its high resistivity per square (Fig. 4.23a) results in reasonably-sized resistors on the chip. Investigating the literature [7], a film thickness of 20 nm was considered for a real device and a verification was done by measuring a sheet resistance of ~6.1 Ω, in the temperature range 3.5-12 K, from a 20 nm thick unpatterned film, deposited over a Si substrate in the JWNC (Fig. 4.23b).

An aspect that electrical simulations could not model is the thermal influence of the resistors on the superconducting region. Every electric conductor dissipates power transformed into heat (Joule heating). Therefore, even if the resistors would be placed as far as possible from the nanowires and the thermal dissipation is expected to be isotropic, the detector could reach a temperature exceeding its T_c. The mentioned references [5, 6], indeed, report about integrated resistors of the order of 4 x 38 Ω and 24 x 70 Ω. A precise prediction of the thermal load is not plausible as the dissipated power is a square function of I_b, which is *a priori* unknown because related to several features of the SNSPD. In a worst-case scenario, I_b could be supposed of the order of 20 μA and whether all the pixels fired simultaneously, the total power would be around 1.5 μW. Such a thermal power produces a local increment of the temperature and extends, in time, the resistive state of the device (see § ***2.4.1***), i.e. the detector could show a very long dead time (see § ***2.1.1***).

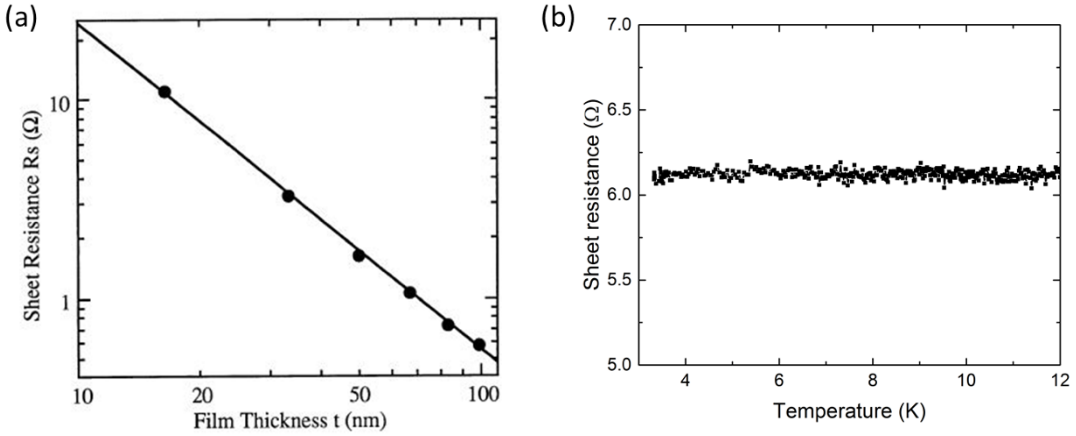

Fig 4.23: (a) Pd-film sheet resistance as a function of the thickness [7]. (b) Sheet resistance of a 20 nm thick Pd unpatterned film as a function of the temperature, deposited in the JWNC.

4.6 Summary

Two simple multiplexing scheme have been presented. The first one is a TDM readout, in which four pixels are independently biased and readout, whose pulses are successively power-combined. It gives the possibility to use the array as infrared camera. In terms of performances, the 30 x 30 μm^2 array system detection efficiency is limited to ~2.6% by the lack of a proper quarter-wave optical cavity and a mirror or DBR for the light source wavelength at 1550 nm; also, the nanowires thickness is 8 nm, rather thick compared with state-of-the-art NbTiN devices [9]. The DCR for such efficiency is ~250 Hz and the timing-jitter is ~71 ps at the 97% of I_c. The 60 x 60 μm^2 array includes a quarter wave optical cavity optimized for photon absorption at 1550 nm and a thinner superconducting film (6 nm). This enhances the efficiencies of the single-pixels up to 24-26%, with the exception of *pixel 3* which is only ~9% efficient. The measurements of the critical currents had already evidenced such nonuniformity (a difference of ~9 μA). At this bias point, the DCRs are all around 10 kHz and the timing-jitter varies from 116 to 163 ps at the 97% of I_c.

A second readout scheme, based on code-division multiplexing, was simulated using SPICE software, suggesting it is possible to obtain a 4-pixel array with common bias and common readout. Without any form of amplification, output pulses from ~80 μV to ~390 μV were obtained, with a margin of at least 60 μV (without external amplification), in order to discriminate the firing pixel. The simulation could have included a higher number of pixels but that would have not been realistic, as the thermal impact of further and higher resistors is supposed to stop the functionality of the superconducting circuit. As the two schemes are fully independent, in principle it would be possible to arrange a multiplexing cascade in which every port of the power combiner is connected to a detector owing four pixels already on-chip multiplexed. Such device could be considered as a 16-pixels camera.

References

[1] Klopfenstein, R. W. (1956). A transmission line taper of improved design. Proceedings of the IRE, 44(1), 31-35.

[2] Kerman, A. J., Dauler, E. A., Keicher, W. E., Yang, J. K., Berggren, K. K., Gol'Tsman, G., & Voronov, B. (2006). Kinetic-inductance-limited reset time of superconducting nanowire photon counters. Applied physics letters, 88(11), 111116.

[3] O'Connor, J. A., Tanner, M. G., Natarajan, C. M., Buller, G. S., Warburton, R. J., Miki, S., et al. & Hadfield, R. H. (2011). Spatial dependence of output pulse delay in a niobium nitride nanowire superconducting single-photon detector. Applied physics letters, 98(20), 201116.

[4] Najafi, F., Marsili, F., Dauler, E., Molnar, R. J., & Berggren, K. K. (2012). Timing performance of 30-nm-wide superconducting nanowire avalanche photodetectors. Applied Physics Letters, 100(15), 152602.

[5] Sahin, D., Gaggero, A., Zhou, Z., Jahanmirinejad, S., Mattioli, F., Leoni, R., ... & Fiore, A. (2013). Waveguide photon-number-resolving detectors for quantum photonic integrated circuits. Applied Physics Letters, 103(11), 111116.

[6] Mattioli, F., Zhou, Z., Gaggero, A., Gaudio, R., Leoni, R., & Fiore, A. (2016). Photon-counting and analog operation of a 24-pixel photon number resolving detector based on superconducting nanowires. Optics express, 24(8), 9067-9076.

[7] Nakagawa, H., Aoyagi, M., Kurosawa, I., & Takada, S. (1992). Palladium thin-film resistors for Josephson LSI circuits. Japanese journal of applied physics, 31(8R), 2550.

[8] Radebaugh, R. (2009). Cryocoolers: the state of the art and recent developments. Journal of Physics: Condensed Matter, 21(16), 164219.

[9] Natarajan, C. M., Tanner, M. G., & Hadfield, R. H. (2012). Superconducting nanowire single-photon detectors: physics and applications. Superconductor science and technology, 25(6), 063001.

Chapter 5 – Low power and long distance Raman-based fibre temperature testbed

This chapter presents a 100 m calibration-free thermometer assembled from standard telecom optical components. A temperature profile is extracted by a separate collection of Stokes and anti-Stokes backscattered photons detected by a single SNSPD channel and time-correlated single photon counting electronics. The performance of this distributed fibre optic temperature sensor is evaluated in the context of potential geothermal energy applications.

5.1 Introduction

As outlined in § ***2.5.4***, there is a growing demand for versatile high performance fibre optic sensors for applications such as geothermal energy. Geothermal industry is continuously investing in newer, more accurate and efficient techniques for downhole temperature measurements (Fig. 5.1). The possibility of rapid and real-time data-acquisition through improved sensing technologies would be revolutionary in this field.

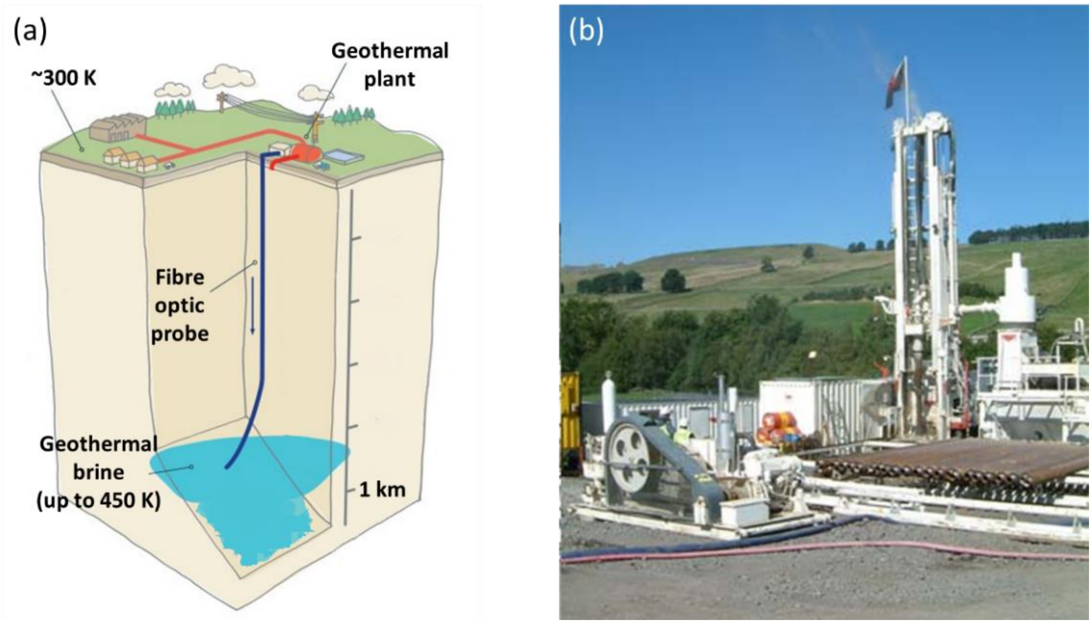

Fig. 5.1: (a) Sketch of a distributed fibre optic testbed to be employed in a 1 km deep borehole; (b) picture of the Eastgate geothermal borehole in Weardale, County Durham, UK.

In fact, a temperature value may lead to the estimation of further parameters such as pressure and enthalpy [1]. This chapter presents development of a novel distributed fibre optic temperature sensor[1] based on infrared photon counting of Raman backscattered signals.

5.2 Setup design and test

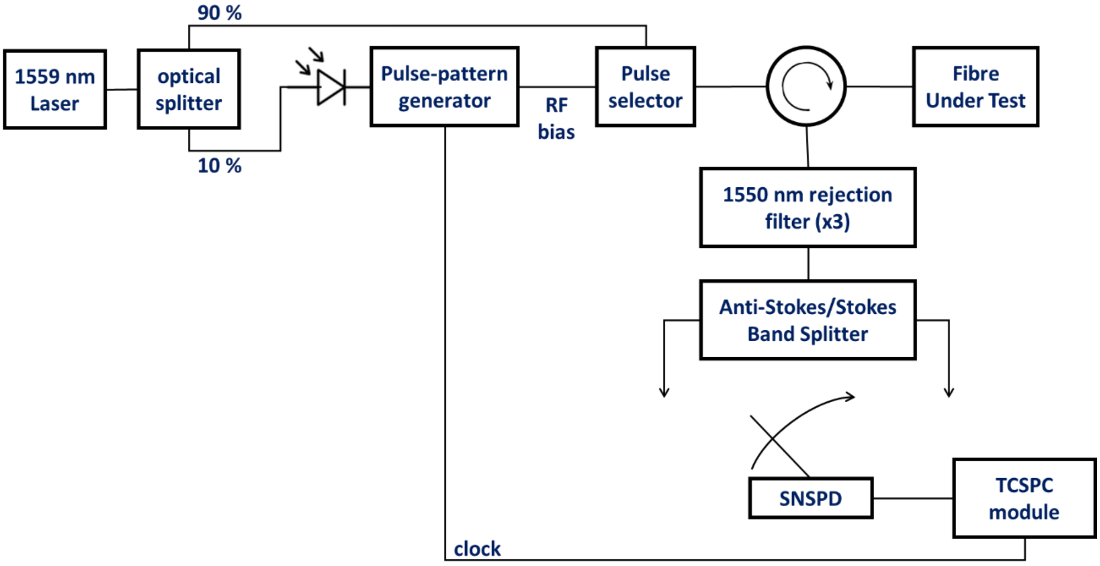

Fig. 5.2: Diagram of the proposed long-distance fibre-optic temperature testbed. The pulsed laser is a picosecond fibre laser with a 50 MHz clock rate, later reduced to 0.93 MHz by a pulse selector and sent to a circulator which delivers the signal to a fibre under test and collects backscattered photons. The final splitter is used to separate Stokes band wavelengths and anti-Stokes band wavelengths. A single SNSPD was available for this experiment, and the outputs of the Stokes and anti-Stokes channels were measured in sequence.

A detailed representation of the testbed is shown in Fig. 5.2. The light source is a Kphotonics CNT-1550-TK fibre laser[2]. Pulses are delivered at a flip of a switch. It is characterized by a centre wavelength at 1559.4 nm, a spectral bandwidth of about 8 nm, an average output power of 1 mW, a pulse duration < 1 ps and a repetition rate (RR) of 50.2 MHz. The laser output is connected to a 90:10 fibre optical-splitter. The 10% splitter-port is used as input for a DET08CFC InGaAs biased detector. It is an APD detector used as optical trigger in the system[3]. The electrical pulses generated by the APD pass through an Ortec Model 9327. It is a 1 GHz amplifier and timing

---

[1] Work carried out in collaboration with Dr. Nathan Gemmell.

[2] A mode-locked oscillator using fibre taper embedded in carbon nanotube saturable absorber.

[3] The laser in use does not own an electrical trigger output.

discriminator used here to increase by a factor ~2 the pulses from the detector. Such signal drives the external input port of a pulse/pattern generator (PPG, model Agilent 8110A) and it is used as an internal clock by the PPG itself that generates then two outputs. The first one is a 0.93 MHz pulsed 10 V signal at 160 MHz [Fig. 5.3], required as AC bias for an acousto-optic modulator (MT160-IIR10-Fio by AA Optoelectronic), acting as a pulse selector. The second output from the PPG is 400 mV pulse pattern at 0.93 MHz. It is the reference clock for a TCSPC module and constitutes the RR for the experiment. As mentioned in § ***2.5.1*** (Eq. 7), RR is a key factor for time-of-flight experiment, determining the maximum length of the fibre under test (FUT). The time measured between a pulse sent into the fibre and the backscattered photon returning down the fibre (and being detected), gives the position in the fibre that the scattering happened. The more time interval there is between pulses, the more time the pulse can stay in the fibre, the longer the fibre can be.

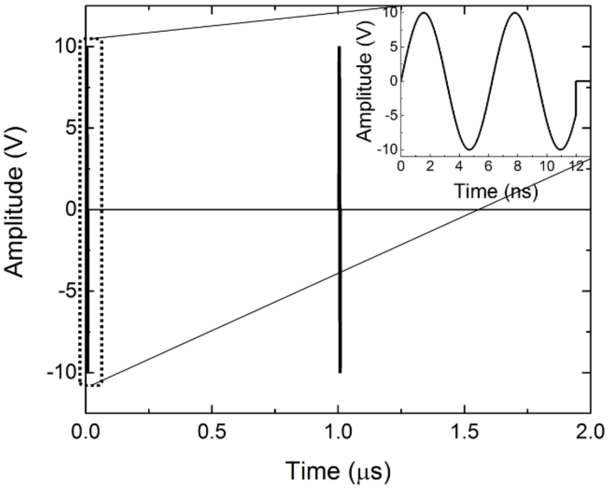

Fig. 5.3: AC bias plot of the acousto-optic modulator employed as pulse selector. Every 1 μs the pulse selector is turned on by a 10 V signal at 160 MHz.

All the optical fibres in the setup are Corning SMF-28e type, characterized by a group refractive index (n)of the core, at 1560 nm, equal to 1.468 (Fig. 5.4) and an attenuation of 0.2 dB/km. Thus, replacing these data in Eq. 7, the proposed setup can perform time-of-flight measurement over ~110 m.

The power of the light leaving the pulse selector was measured on by an optical power-meter (Thorlabs PM100D) and it was found of the order of 0.4 μW. Such light gets injected into the FUT via a three-port fibre-optic circulator. The FUT is ~101m; the first meter is just the port-2 end of the circulator which is connected with a 100 m section by an APC[4]/APC adapter. In terms of temperature, almost 25 m lay on an optical table in a room at ~17 °C (290 K; temperature read on a thermostat in the room) and the remaining part of the fibre is stored inside a commercial freezer at about -22 °C (251 K; temperature read on a digital thermocouple). The FUT had been placed overnight in the freezer, in order to be properly and uniformly cooled down. The backscattered signal propagates from port-3 of the circulator to the SNSPD; profiles of Stokes and anti-Stokes gain as a function of the frequency shift are extensively investigated in the literature [2, 3]. In case of silica fibres, like SMF-28e, Stokes photo-generation shows a peak for a 440 cm^{-1} shift, which corresponds to ~12 THz. The anti-Stokes gain does not show a peak around that shift but it is almost constant over a small neighbourhood of the Stokes peak. It is possible to compute that for the employed laser, there is a peak of backscattered Stokes-photons at 1675 nm.

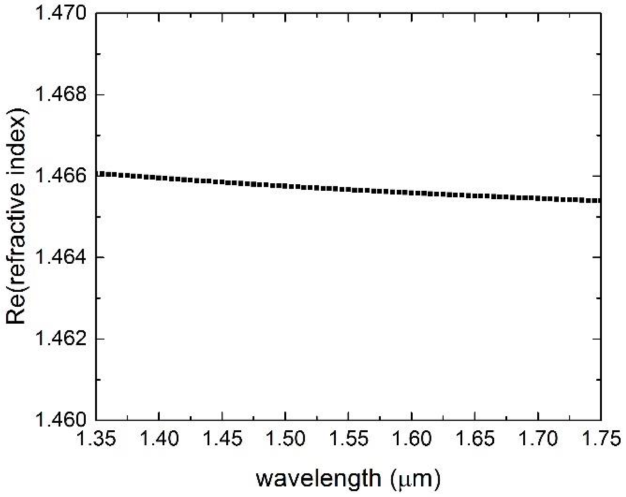

Fig. 5.4: Real part of the group refractive index of Silica as a function of the wavelengths in the range of the experiment. Data reproduced from [4].

Considering all above, a chain of in-fibre rejection filters (Thorlabs WD202B, WD202H and WD202C) was assembled and connected to circulator port-3, in order to reject Rayleigh photons around the 1560 nm wavelength. At the end of the filtering chain there is a splitter (GoFoton EWDM-FP-K-M-112), which separates

---

[4] Angled Physical Contact

Stokes and anti-Stokes signals. For the backscattered photons, the final splitter is the only bifurcation in the optical path. The SNSPD will then alternately detect photons from the two outputs of the splitter. Such optical channels were characterized as a function of the wavelength (Fig 5.5), using tuneable laser sources at the input: HP 8168F (from 1480 to 1590 nm) and Yenista Optics ECL/T100 (from 1570 to 1680 nm).

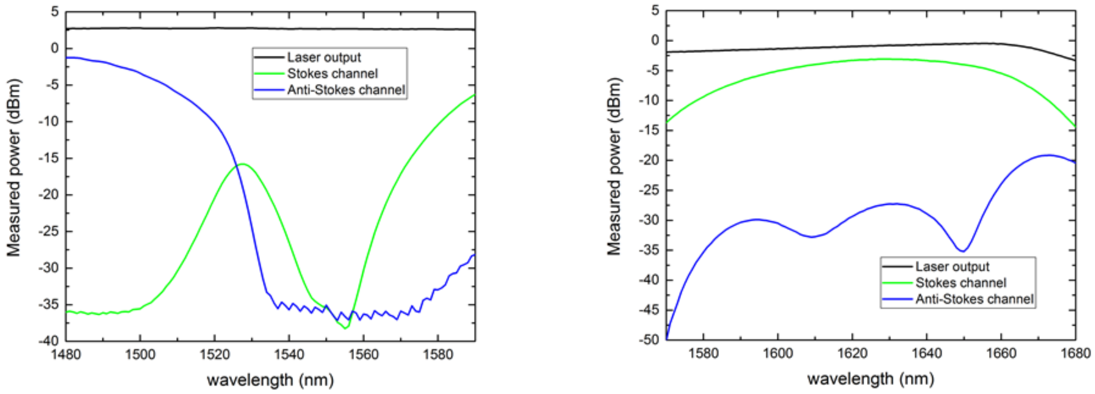

Fig. 5.5: Measured optical power (via power meter) as a function of the wavelength of the optical setup for Stokes and anti-Stokes photodetection. In black, the tuneable laser power output. In green, the Stokes channel optical response. In blue, the anti-Stokes channel optical response.

The data show how the anti-Stokes channel (blue line) attenuates by ~30dB photons at unwanted wavelength (1530 – 1660 nm). The Stokes channel, instead, presents a -15dBm peak around 1530 and a ~35dB attenuation till 1510 nm and around 1555 nm (Rayleigh backscattered photons).

5.3 Detector characterization

The detector selected for the experiment (Fig. 5.6) was fabricated in Japan at the National Institute of Information and Communications Technology (NICT), in 2013 [5]. It is single-pixel NbTiN meander, whose wires are 5 nm thick, 60 nm spaced and 100 nm wide, with an overall active area of 15x15 µm^2. Nanowires are encapsulated among a 270 nm SiO2 and a 250 nm SiO layer, with both thickness designed to be quarter-wave for a 1550 nm wavelength.

The top layer is a reflective 100 nm Ag mirror, deposited to enhance the absorption efficiency. The entire device was fabricated on an Si substrate.

Following the same procedures explained in chapter 3, after a cool down to 2.4 K, transport properties were immediately tested; a current versus bias voltage (*I*-*V*) plot was taken, applying a 50 Ω shunt (fig. 5.7). Although a small offset due to the readout electronics, the sample showed a critical current I_c of about 4.5 µA, measured over the 10%-90% transition interval.

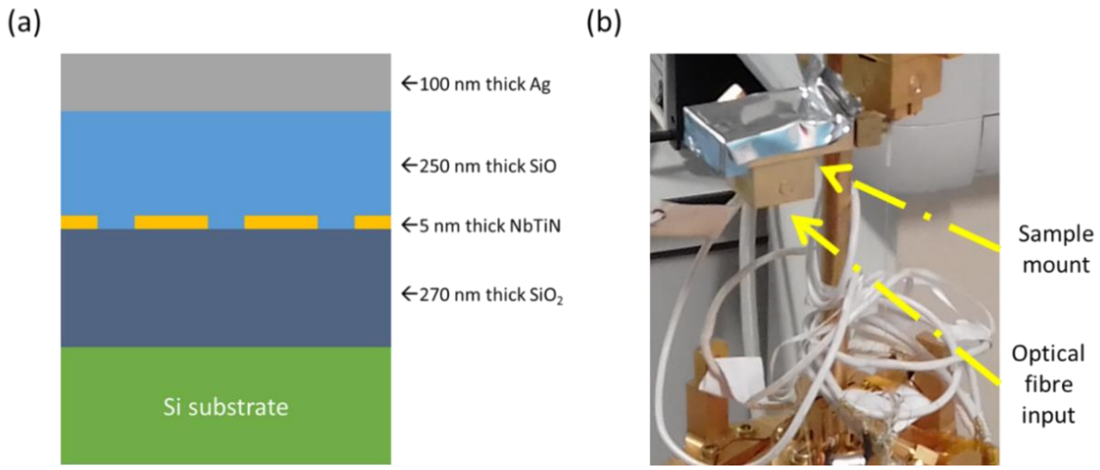

Fig. 5.6: (a) Schematic configuration (not in scale) of the SNSPD employed in the experiment. The superconducting NbTiN meander is encapsulated between an SiO layer and an SiO_2 layer, on top of which is placed an Ag mirror to complete the optical cavity. The photons are delivered via an optical fibre coupled from below. (b) Picture of the packaged detector mounted in the cryostat. A metal tape is applied on top of the sample mount to protect the detector.

An estimation of the system detection efficiency was then calculated as in § ***3.3.3***, differing only for the photon flux generated by a 1559 nm laser for different bias voltage and regulated also by a manual fibre polarization controller: its use is motivated by a different photo-absorptance (a factor 2, typically [6]) of an SNSPD when light is polarized parallel to the nanowires compared to a perpendicular polarization.

The measurements revealed a ~1% detection efficiency for low-efficiency polarization and ~2.5% for the high-efficiency polarization, at the highest single-photon detection bias where dark count rate is about 1 kHz (Fig 5.8). Those efficiencies, however, are lower than expected compared to the best devices of this design reported [5]. It is reasonable that the practical efficiency is low either due to fibre misalignment or degradation of the device over time and with thermal cycling. The latter hypothesis is supported by the reduced critical current observed (4.5 µA versus >15 µA for the first measurements on other devices from this batch). This low I_c also impacts the timing jitter (smaller output pulses lead to larger timing jitter).

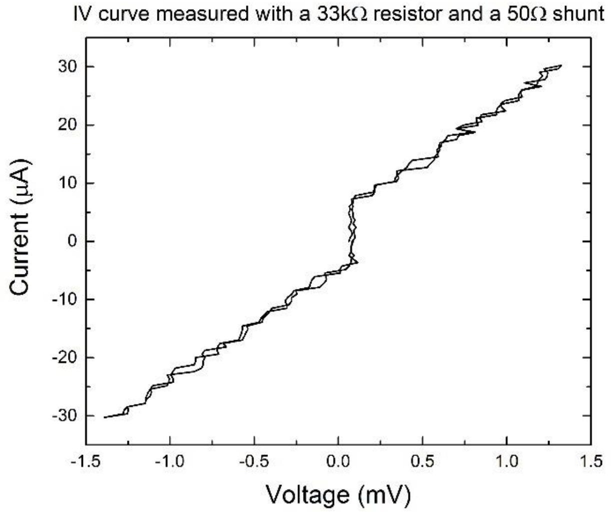

Fig. 5.7: *I-V* curve of the SNSPD mounted in a closed cycle refrigerator at 2.4 K. Correcting the offset, the critical current is ~4.5 μA.

However, an additional efficiency characterization is required, aimed to check the behaviour of the detector as a function of the wavelength of the light source.

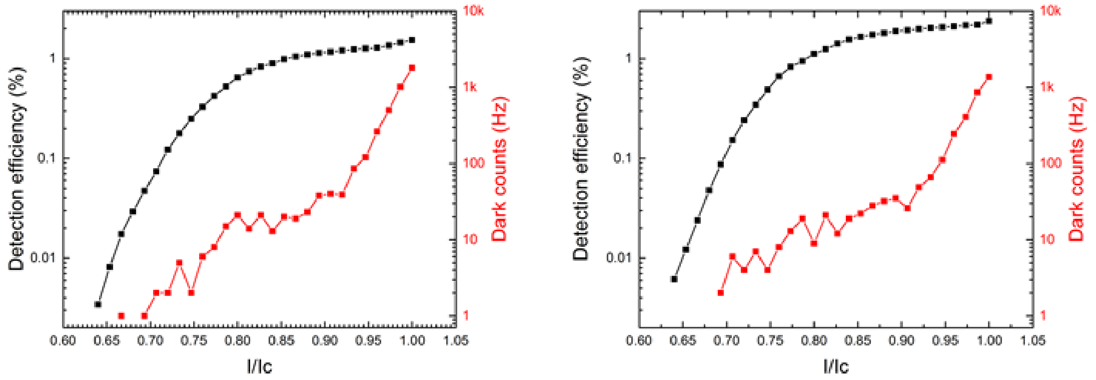

Fig. 5.8: Detection efficiency (1559 nm wavelength, pulsed at 50 MHz) and dark count-rate as a function of the normalized bias for low-efficiency polarization (left) and high-efficiency polarization (right).

With the help of an Agilent 111896A computer-controlled polarizer and set the bias at the 98% of the I_c, such a detection efficiency was computed (Fig. 5.9). Data were normalized for the two polarizations to extract a factor indicating the variation of the efficiency in the wavelength range from 1480 to 1590 nm. For the high-efficiency polarization and low-efficiency polarization, a maximum discrepancy of ~1.34 and ~1.32 were noticed respectively and the related standard deviations are ~0.041 and ~0.018. A degradation of the device is now more plausible, as no enhancement of the optical response is observed around 1550 nm. A damage to the top Ag mirror could also account for this.

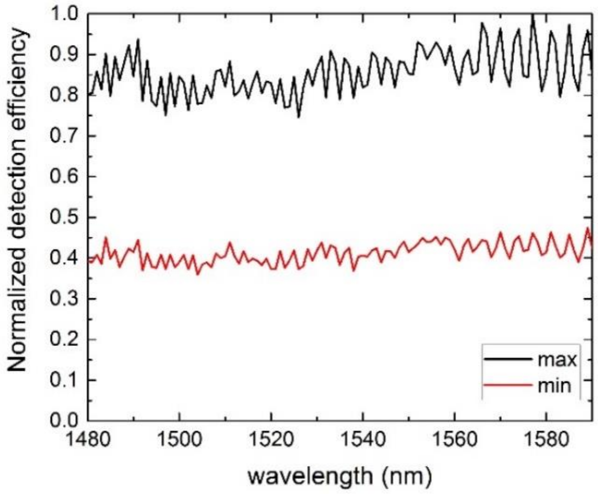

Fig. 5.9: Normalized detector efficiency as a function of the source-wavelength, biased at the 98% of the critical current. Minimum value (red line) and maximum value (black line), for a given wavelength, computed with the use of a computer-controller polarizer.

Essential measurement for a reflectometry is the timing-jitter. Photons are collected as a function of time until a reference threshold is reached (10^6 detection events chosen in this case). Measuring the jitter of the detector as explained in § ***3.3.5***, a full-width at half-maximum (FWHM) of 223 ps was obtained (Fig. 5.10).

There are other jitter-components in the testbed. The first one (≤40 ps) due to the amplifier in series with the APD, the second one (≤20 ps) due to the PPG that drives the pulse-selector transitions. As the total jitter is the square root of the sum of the squared components, the previous time jitter does not change significantly.

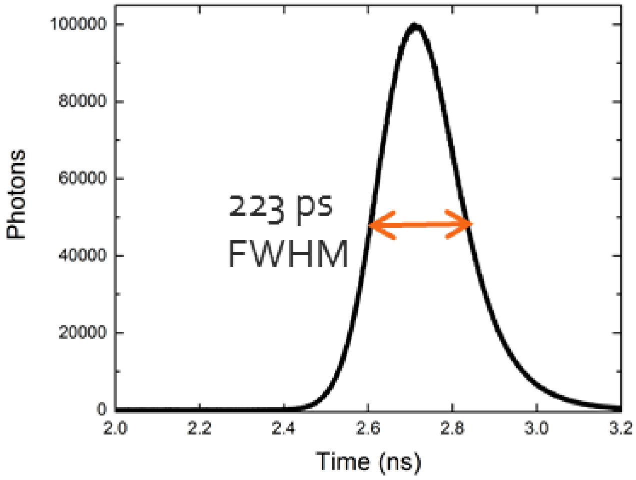

Fig. 5.10: Time-jitter plot of the SNSPD detector in use, biased at the 98% of the critical current.

In conclusion, setting the bin-width higher than 223 ps in a time-of-flight experiment, such setup offers time (and consequently spatial) single-photon resolution no lower than ~112 ps, i.e. half of the timing-jitter because, in time-of-flight tests, signal propagates forward and backward between two given points (see Eq. 7).

5.4 Optical measurements and temperature extractions

With the support of the TCSPC module, it was possible to have plots of the Stokes and anti-Stokes channel as a function of the bins. The bin-width is set through the software of the TCSPC module and governs the spatial resolution (SR) of the measurement.

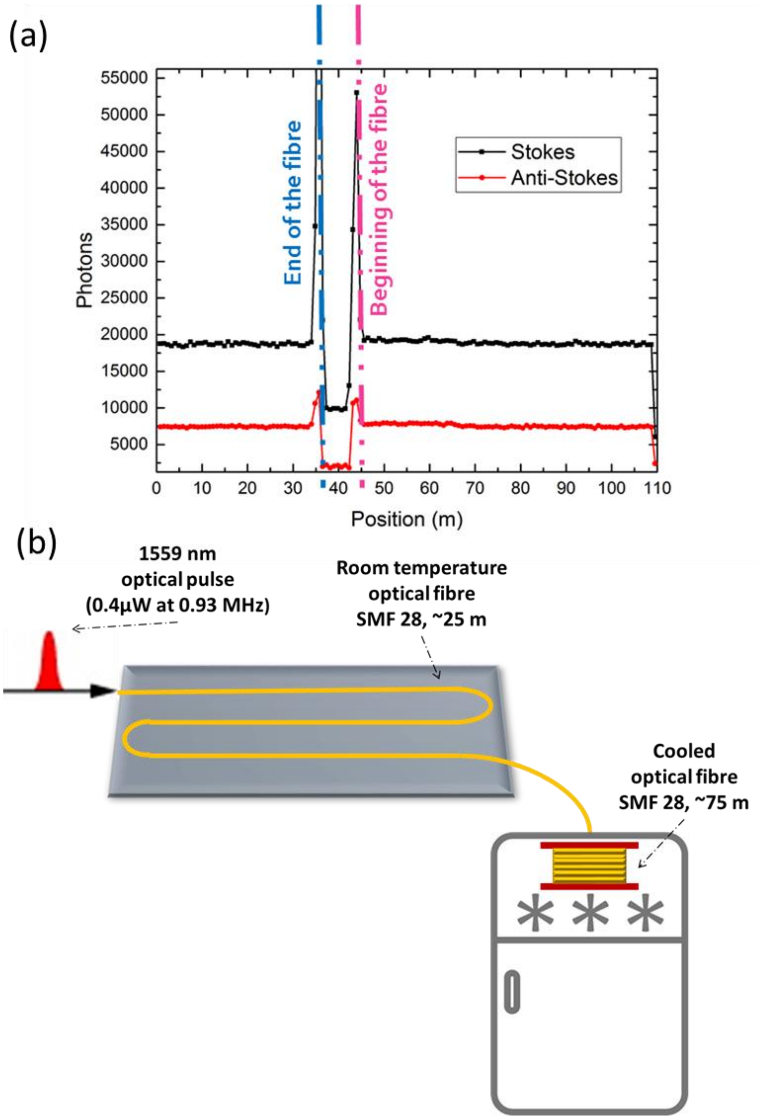

Fig. 5.11: (a) TCSPC plot of Stokes (black) and anti-Stokes (red) backscattered count rates as a function of the position for a 100 m long fibre, tested by a 1559 nm laser source with a repetition rate of 0.93 MHz and power of 0.4 μW.
(b) Illustration of the distributed optical probe configuration.

Dividing the speed of light in the vacuum by the group refractive at the 1560 nm pump wavelength (Fig. 5.4), a group velocity in-fibre of ~21 cm/ns is obtained. Hence, the 8192 ps bin-width, set on the Hydraharp module[5], corresponds to a SR of ~83 cm[6]. In other words, to avoid as much as possible local noise on some sections of the 100 m FUT, a wider bin width was deliberately selected, sacrificing the minimum SR given by the 223 ps jitter, that is ~2.35 cm.

Moreover, in order to avoid any pile-up effect (see § ***3.3.5***), the detector was biased below the critical value, resulting in a photon count rate below the 5% of the 0.93 MHz RR. That implies a DCR around 10^2 Hz. In this way, the DCR is also visibly lower than the backscattered signal.

Setting an acquisition time of 100 minutes per channel and converting the bins axis into a position axis, it was possible to plot the backscattered photons from the FUT as a function of the position (Fig. 5.11a).

The plot offers some positive indications:

1. The anti-Stokes count rate is lower than the Stokes one. As the detector (and its bias) is the same and as the optical path is almost entirely common for both the channels (excluding the final splitter), the measurement is in good agreement with the theory of Raman backscattering (see § ***2.5.3***). Also, from Eq. 11 solved with the known temperatures (290 K, 251 K), the peak wavelengths of the Stokes and anti-Stokes contributions (1675 nm and 1480 nm) and the wavelength shift (440 cm^{-1}), the ratio between the Stokes and the anti-Stokes intensities was expected to be almost equal to 5. Here, the experimental result indicates a ratio of about 2.5, that is even in better agreement with other experimental results [2]. The mismatch is attributed to a non-ideal selectivity of the filters and, therefore, a fraction of photons at shorter or longer wavelength of the Stokes and Anti-Stokes contributions are included in the count-rates. Moreover, the Stokes channel is centred around 1640 nm.
2. Two major peaks are noticeable on each signal. They are strong reflections produced by the end of the FUT and the circulator. The offset on the position

---

[5] The Hydraharp bin-width can be set solely as power of two.

[6] Half (because it is a time of flight) of the product of the group velocity times the bin-width.

axis (~35 m) depends on the delay between the optical pulse and the electrical pulse (from the PPG) used to trigger the TCSPC module. Indeed, that module cyclically acquires the signal while the optical-start may be shifted to the mechanical beginning of the FUT length. To confirm that, the distance from the peak around 45 m to the end of the axis and the initial offset is very close to 100 m, i.e. the length of the FUT.

3. Both the acquisitions show a ~10 m section over which the count is significantly lower than the rest of the plot. This is due to the clock of the setup which allows a maximum FUT of 110 m, as explained in § **5.2**. Such extra section can be helpful to evaluate the backscattered dark pulses B_S and B_{AS}, necessary for Eq. 15. Indeed, the arithmetic mean of those points on the plot will be used to approximate B_S and B_{AS}.

First step of the data analysis (Fig. 5.12) was the subtraction of the dark counts on the two signals.

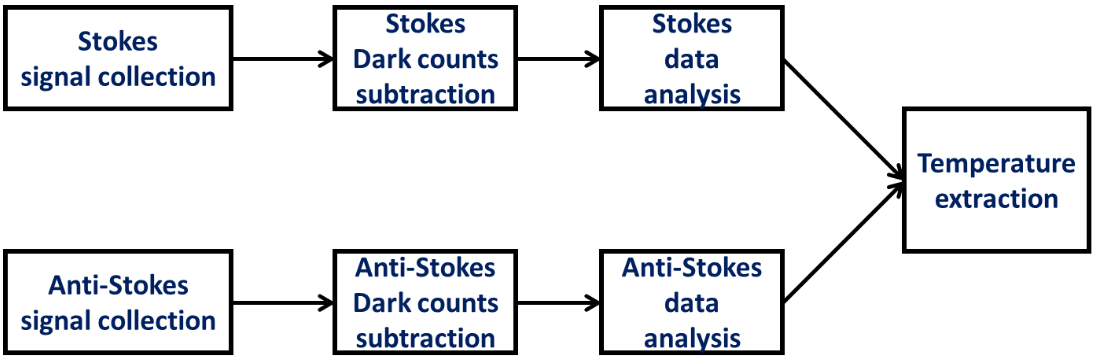

Fig. 5.12: Flow chart of a fibre temperature sensor based on Raman backscattering. Stokes and anti-Stokes signals are collected (simultaneously or sequentially). Then, dark counts (measured or estimated) are removed from those signals which are numerically filtered by Eq. 20 (data analysis). Finally, the signals are used in Eq. 21 to obtain a temperature profile.

Secondly, a shifting weighted average among five sequential points, in which the central one has a double weight, was calculated for the two channels (Fig. 5.13):

$$I_u'(x) = [I_u(x-2) + I_u(x-1) + 2I_u(x) + I_u(x+1) + I_u(x+2)]/6 \quad \text{(Eq. 20).}$$

As the number of bins is not reduced and the average is weighted, the space resolution is mainly preserved. The reason for such average is the use of wavelength peak-values in the following calculations rather than a proper integral over the entire interval of wavelengths included in the Stokes and anti-Stokes channels.

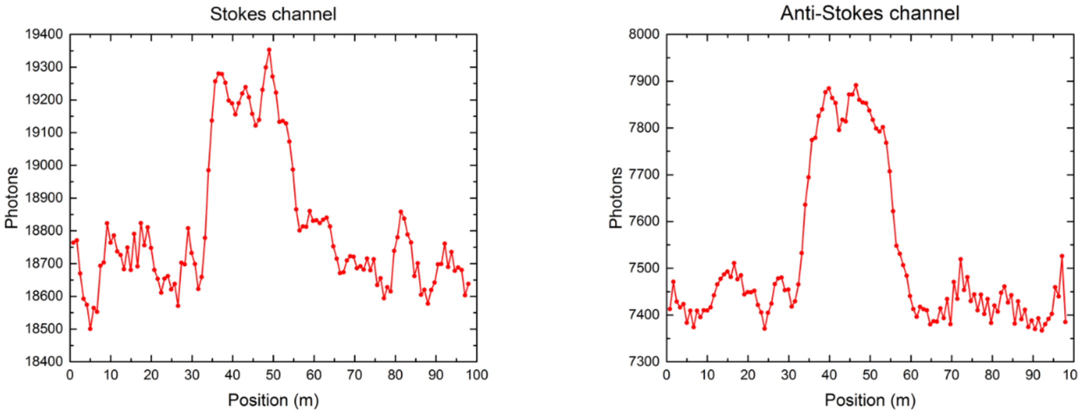

Fig. 5.13: TCSPC plot of Stokes and anti-Stokes backscattered signal as a function of the position for a 100 m long fibre, tested by a 1559 nm laser source with a repetition rate of 0.93 MHz and power of 0.4 µW. The measured count rates were processed by Eq. 20 and later used to extract a temperature profile.

Essential operation for a correct temperature extraction is the determination of the parameters coming from the setup, which also eliminates every form of pre-calibration for the setup. One of those parameters is the Raman gain ratio (R_{gr}) between the two channels. Knowing the pump central wavelength λ_p (1559 nm), the peak anti-Stokes wavelength (1480 nm) and the real part of the FUT refractive index (n = 1.468), the frequency shift F_{AS_p} between the anti-Stokes central wavelength (λ_{AS} = 1480 nm) and the pump peak wavelength (λ_p = 1559 nm) may be quickly approximated as follows:

$$F_{AS\_p} = \frac{c}{n}\left|\frac{1}{\lambda_p} - \frac{1}{\lambda_{AS}}\right| \qquad \text{(Eq 19).}$$

For the designed setup, F_{AS_p} is of the order of $7\text{x}10^{12}$ Hz meaning the Stokes photo-generation may be approximated as 2.5 times stronger than the anti-Stokes photo-generation [2], in total agreement with the value experimentally obtained (Fig. 5.11a).

The bandwidth gain ratio may be computed dividing the 3dB bandpass wavelength-interval of the two channels. However, for the chosen optical components, the bandwidth gain ratio can be approximated to 1. In brief, Eq. 15 is transformed into:

$$T(x) = {h\left|F_{AS\_p}\right|} \Big/ {k_B \ln\left(\frac{I'_S(x)-B_S}{R_{gr}[I'_{AS}(x)-B_{AS}]}\right)} \qquad \text{(Eq 21).}$$

The last equation was implemented in MatLab to compute a temperature profile.

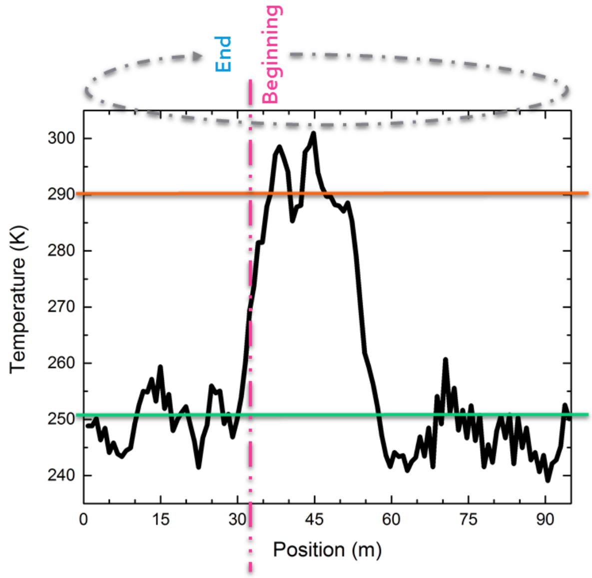

Fig. 5.14: Temperature as a function of the position extracted from Eq. 21. Around 75m of the fibre was stored in freezer at 251 K (green line), the remaining length was left at room temperature (orange line). tested by a 1559 nm laser source with a repetition rate of 0.93 MHz and power of 0.4 µW.

Data indicate that ~75 m of the FUT show temperature between 261 K and 239 K (Fig. 5.14). That corresponds to the section inside the freezer, providing a maximum discrepancy of 12 K with respect to the 251 K from the digital thermocouple reference. The remaining part of the FUT (~25 m) measures temperature between 281 K and 301 K, whose maximum discrepancy with temperature read on the room thermostat is 11 K.

5.5 Discussion

At the time of writing, the presented setup, enabling temperature measurements over 100 m of fibre, is the longest fibre-temperature sensor based on Raman backscattered photons detected by SNSPD. The SR of the setup is ~83 cm per bin, which is higher than other results seen in literature [7, 8] for Raman-effect sensor at single-photon-level. However, the ratio between the space resolution and the total length under test is sensibly closer to the same results.

Setup	Pizzone *et al.*	Tanner *et al.*	Vo *et al.*
Length (*l*)	100 m	2.8 m	2.7 m
Spatial resolution (SR)	83 cm	1.2 cm	0.6 cm
Ratio (SR/*l*)	$0.83\cdot10^{-2}$	$0.43\cdot10^{-2}$	$2.22\cdot10^{-3}$
Acquisition time	100 min	1 min	2 min
Temperature range	316-251 K	360-310 K	303-383 K
Temperature uncertainty	5.1 K	3 K	0.2 K
Fibre type	SMF-28	SMF-28	Chalcogenide
Raman peak	$\sim 9\text{x}10^{-14}$ m/W	$\sim 9\text{x}10^{-14}$ m/W	$\sim 5\text{x}10^{-12}$ m/W
Stokes shift (peak)	440 cm^{-1}	440 cm^{-1}	344 cm^{-1}
Laser source	0.4 µW 1559 nm	18 mW 1533 nm	2.7 mW 1551 nm

Tab. 1: Comparison of SNSPD-based distributed fibre temperature sensors [7, 8].

By the use of standard uncertainty analysis methods [9], the standard deviation of the temperature profile was calculated, indicating an uncertainty of ~5.11 K. A deeper analysis can be done using the following equation:

$$\Delta T \approx \frac{k_B T^2}{h|F_{AS\_p}|}\sqrt{\frac{1}{I'_S}+\frac{1}{I'_{AS}}} \qquad \text{(Eq. 22).}$$

Such analysis reveals a mean absolute error of ~5.16 K.

Both the presented methods evaluate the uncertainty starting from a temperature already extracted. A deeper investigation could be realized starting from the measured (and unsmoothed) count rates. Developing the concatenated standard deviation [10] of the simple sub-equations that constitute Eq. 13, the obtained equation is:

$$\sigma(T) = \frac{h|F_{AS\_p}|}{k_B\left(\ln\left({}^{I_S}/_{I_{AS}}\right)\right)^2}\sqrt{\left(\frac{\sigma_S}{I_S}\right)^2+\left(\frac{\sigma_{AS}}{I_{AS}}\right)^2-\frac{2\sigma_{S\_AS}}{I_S I_{AS}}} \qquad \text{(Eq. 23).}$$

After computing the standard deviations of the Stokes and anti-Stokes count rates (σ_S and σ_{AS}) and the relative covariance (σ_{S_AS}), the resulting value $\sigma(T)$ is ~7.79 K. That also means that, statistically, the data-smoothing affect the temperature extractions by less than 3 K.

In contrast with other configurations, no form of polarization control was introduced in the setup. It is useful to underline the performed measurement involves the ratio of two signals, Stokes and anti-Stokes. If it is true that the state of polarization of the light-source varies randomly with position in the FUT, as a consequence of localized variations in the birefringence of the fibre-core depending on bends or twists in the fibre, it is also true that is common for both the signals. Equally common for both the signals are the polarization effects associated with the SNSPD meander geometry. The detection efficiency mismatch of an SNSPD for polarizations that are parallel to the meander wires compared with polarizations that are perpendicular to the meander could reach a factor ~2 [6], as already demonstrated in § **5.3** (Fig. 5.9). Another polarization-dependent factor is the Raman gain, which should be considered as a tensor [11]. Besides, the setup is subjected to variations in time of the polarization of the light-source that is not common for the anti-Stokes and Stokes signals when detected in different times. Anyway, as the acquisition time is of the order of 100 minutes and the bin-width covers ~83 cm of the FUT, a statistical compensation of photons impinging perpendicular and parallel on the detector is very reasonable, likewise a compensation between local photon generation altered by polarization-effects.

Truly, the use of narrower bandpass filter for the Stokes and anti-Stokes channels would deeply reduce the uncertainties on the approximations inserted in the temperature extraction relationship.

The total acquisition time of 200 minutes (100 minutes per channel) was demanded by the generation of a high photon-count in a setup having an optical power-source of 0.4 μW and a 1% efficiency detector. Indeed, the higher is the count rate, the lower is the bin-error (inverse of the SNR, Eq. 19).

Essentially, the acquisition time can be reduced in several and independent ways:

- The use of a second SNSPD halves the acquisition time, allowing a simultaneous measurement of the two channels. It is extremely helpful to delete the bias-shifting effects, in time, related to electrical noise from the ground that may result in unbalanced count rates between the Stokes acquisition and the anti-Stokes acquisition.

- A more powerful light-source will generate a higher number of backscattered photons, for an equal time interval.
- Higher efficient detector will contribute to count more photons, with the same light-source and acquisition time.

Merging these considerations (deriving from Eq. 12) with the performances accomplished by the testbed, it is possible to compute and approximated acquisition time as a function of the optical power and the detector efficiency (Fig. 5.15).

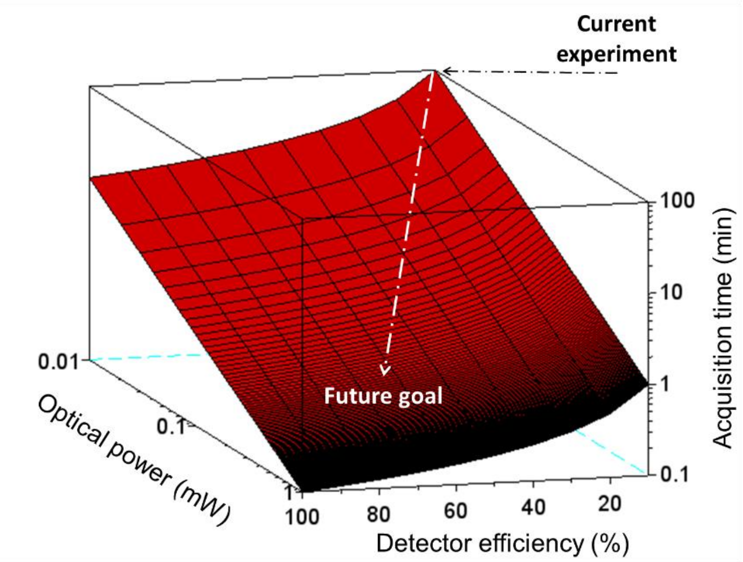

Fig. 5.15: Simulation illustrating the acquisition time (in log scale) per channels as a function of the optical power (in log scale) and the efficiency of the detector.

To prove this hypothesis, a test without the pulse selector was executed (Fig. 5.14). The optical power entering the circulator is now ~0.95 mW, while the FUT is 2 m long, the maximum allowed by a 50 MHz RR for the SMF-28e fibre. The first meter is again the port-2 end of the circulator, connected with a 1 m extension by an APC/APC adapter (Fig. 5.16). As the RR is ~50 higher than the previous case, there is no need for under-biasing the detector as the pile-up effect threshold on the TCSPC module is respected. The temperatures to be measured in this test are also closer to the range expected in a geothermal borehole.

Under such circumstances, the DCR increases to ~10^3 Hz, while photon count-rate is of the order of 10^5 Hz. That means the dark pulses factor B_S and B_{AS} are now neglectable in the temperature extraction. The bin-width was set to 256 ps, which implies a space resolution of ~2.68 cm.The variation of temperature along the fibre was achieved by placing a metal teapot, having a diameter of ~14 cm, filled with hot water. Such method for modifying the temperature over a part of the fibre is not ideal as the in-freezer cool-down. For that reason, the acquisition time for this test is 6 minutes per channel, although the optical power now is almost 2400 times higher.

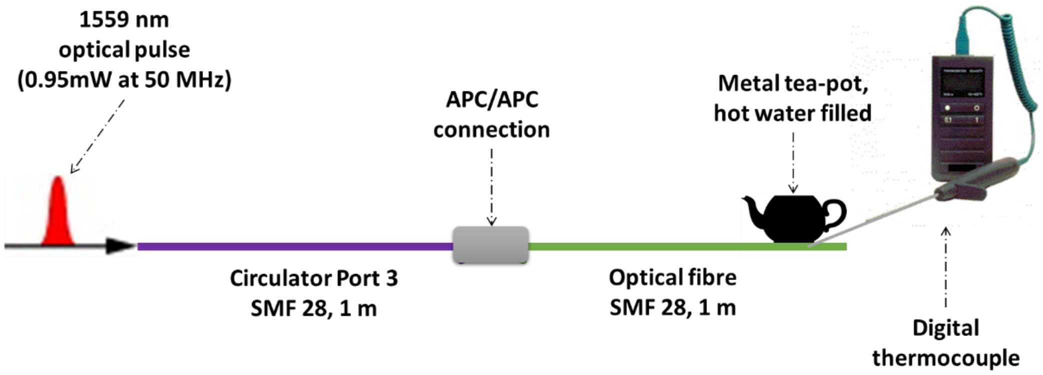

Fig. 5.16: Graphic illustration of the experiment performed over 2 m, without the pulse selector.

All the other settings to extract the temperature were not changed, apart from the weighted average on the backscattered count rates that were reduced to three points:

$$I_u''(x) = [I_u(x-1) + 2I_u(x) + I_u(x+1)]/4 \qquad \text{(Eq. 24).}$$

The reduction of the points in weighted average from five to three derives from the bin-width and the FUT, both shorter. A weighted average over five points, like previously computed, would have excessively altered the signals ratio.

Hence the equation used for the extraction of the temperature from the 2 m FUT is:

$$T(x) = {h|F_{AS\_p}|} \Big/ {k_B ln\left(\frac{I''_S(x)}{R_{gr}[I''_{AS}(x)]}\right)} \qquad \text{(Eq. 25).}$$

The measured data (Fig. 5.17) confirms how the designed setup is still able to identify the warmed-up section of the FUT from the rest. The ratio between the Stokes and anti-Stokes count-rate is almost equal to 2.6, again in good agreement with the previous test, the theoretical expectations (i.e. Eq. 11) and other experimental results [2]. For ~120 cm the temperature oscillates between 295 K and 283 K, while the temperature read on the room thermostat was ~290 K. For what concerned the heated part of the fibre, temperatures between 319 K and 310 K were obtained, while the temperature read on a digital thermocouple, whose probe was sensing the surface touching a portion of the FUT, indicated 316 K.

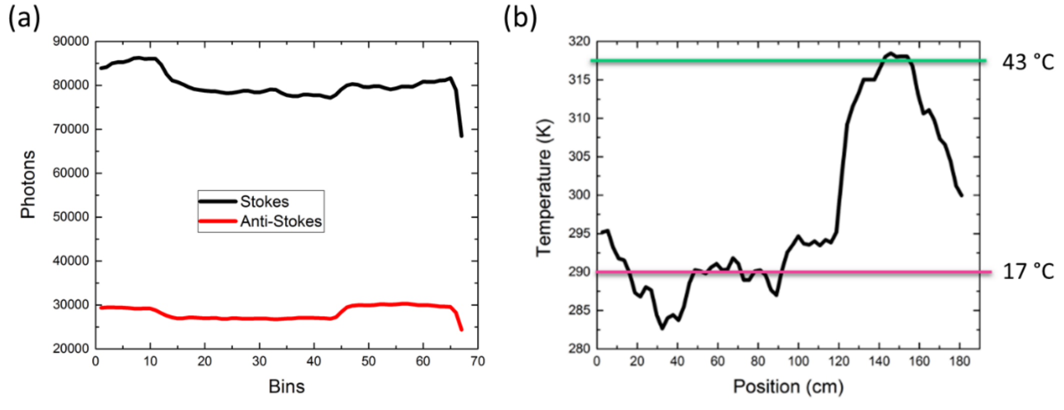

Fig. 5.17: Stokes and anti-Stokes photo-intensities as a function of the bins (a), converted to temperature as a function of the position (b). The green line is the temperature of a metal teapot used to warm up ~14 cm, while the remaining length was left at room temperature (pink line).

The last temperature was read during the switch between the acquisition from the two channels. Also, to be noticed is the lack of the offset between the geometrical start of the fibre and the optical start of the measurements (seen in Fig. 5.9a and 5.12), in agreement with absence of an electrical signal, from the PPG, that modulates the TCSPC module.

The plot shows steady transitions between the parts of fibre at different temperatures. It is reasonable to assume that is a combined effect of the pressure of the teapot on the fibre and the heat conduction inside the fibre.

Such test, on a shorter FUT, demonstrates how the Stokes channel is noisier than the anti-Stokes channel (Fig. 5.15). That is consistent with the tuneable-laser characterization of the channels (Fig. 5.3), in which the Stokes filtering is less selective than the anti-Stokes filtering.

5.6 Summary

A proof-of-principle 100 m optical fibre thermometer based on Raman backscattered photons detected by an SNSPD sensor was designed, assembled and tested. Utilizing a 0.4 µW laser source at 1559 nm with a RR down-converted to 0.93 MHz and a 1% efficient detector, the testbed responded with a maximum temperature error of 12 K and a standard deviation/mean absolute error of ~5.1 K.

In terms of demonstrated performance, the presented setup shows promising characteristics for a geothermal energy testbed [12]. In terms of SR of the optical probe, the setup worked better than current commercial technologies for geothermal energy [13, 14]. Nonetheless, the typical geothermal boreholes may vary from 500 m to 3.5 km of depth, meaning that at least 5 measurements should be performed to cover the full distance. This is a slow procedure if using only one SNSPD because the whole measurement would last around 17 hours (5 times 200 minutes). It is twice the time required by the logging method (see § ***2.5.4***).

A specification that needs to be enhanced is the achievement of a lower temperature uncertainty. In some geothermal boreholes previously studied, the extracted average temperatures were included in a range of 20 K [15]. That is close to the maximum temperature error observed (12 K). However, it is important to remark that such system is calibration-free with respect to the temperature scale and harsh environmental conditions (e.g. pressure, density, mass-fractions). Additionally, the probe could stay longer inside high-temperature boreholes, compared to electronic thermocouples usually employed in logging techniques [16]. In fact, in terms of thermal stress on the probe during on-field measurements, the FUT shall resist to temperatures of the order of 450 K. Ruggedized and metallized optical fibres represent valid solutions although the isolation provided by thermal shields like those, must be considered when extracting the temperature from the count rate. As the setup was tested between room temperature and freezing, it is thus desirable to proceed with in-lab tests by employing hot-plates, ovens or heated water baths, in order to locally reproduce the range of temperatures in borehole. Furthermore, the optical probe is supposed to experience some random strains inside a borehole, like vibrations and twists[7]. Those actions affect the polarization and then the count rate. Some indications were already noticed in the test where a tea-pot pressed on the fibre (Fig. 5.15). In any case, the simultaneous measurement of the Stokes and anti-Stokes would guarantee a simultaneous influence on the count rate, to be removed in the ratio of the two signals.

---

[7] The candidate acknowledges Prof. Paul Younger, Dr. Robert Westaway and Anggoro Wisaksono, from the *Systems, Power and Energy* research division of the University of Glasgow, for all the discussions held.

Excluding the detector and the light source, this setup is, in principle, ready to extend the spatial range of measurement to 1 km and more. Just by tuning the pulse selector, a lower RR is easily achievable. However, a lower RR implies an extra under-bias for the SNSPD in use. Hence, a pair of detectors with higher efficiency and very low DCR becomes more than a requirement that reduce the minimum acquisition time to observe a decent signal.

Also, for long distances, the use of a picosecond pulsed laser source was not exploited because the bin width was kept deliberately higher, in order to obtain a reasonable temperature resolution. Therefore, it is preferable to switch to a nanosecond pulsed laser, whose linewidth is intrinsically narrower (e.g. ID300 1550 nm DFB laser, by ID Quantique). That would dramatically reduce the Rayleigh backscattered photons and other forms of noise generated by Stokes and anti-Stokes photons at wavelengths close to the bandpass peaks of the optical filters/splitters.

References

[1] Palliser, C., & McKibbin, R. (1998). A model for deep geothermal brines, I: TpX state-space description. Transport in porous media, 33(1), 65-80.

[2] Lin, Q., Yaman, F., & Agrawal, G. P. (2007). Photon-pair generation in optical fibers through four-wave mixing: Role of Raman scattering and pump polarization. Physical Review A, 75(2), 023803.

[3] Asobe, M., Kanamori, T., Naganuma, K., Itoh, H., & Kaino, T. (1995). Third-order nonlinear spectroscopy in As_2S_3 chalcogenide glass fibers. Journal of applied physics, 77(11), 5518-5523.

[4] https://refractiveindex.info/?shelf=main&book=SiO2&page=Lemarchand

[5] Miki, S., Yamashita, T., Terai, H., & Wang, Z. (2013). High performance fiber-coupled NbTiN superconducting nanowire single photon detectors with Gifford-McMahon cryocooler. Optics express, 21(8), 10208-10214.

[6] Anant, V., Kerman, A. J., Dauler, E. A., Yang, J. K., Rosfjord, K. M., & Berggren, K. K. (2008). Optical properties of superconducting nanowire single-photon detectors. Optics Express, 16(14), 10750-10761.

[7] Dyer, S. D., Tanner, M. G., Baek, B., Hadfield, R. H., & Nam, S. W. (2012). Analysis of a distributed fiber-optic temperature sensor using single-photon detectors. Optics express, 20(4), 3456-3466.

[8] Vo, T. D., He, J., Magi, E., Collins, M. J., Clark, A. S., Ferguson, B. G. *et al.* & Eggleton, B. J. (2014). Chalcogenide fiber-based distributed temperature sensor with sub-centimeter spatial resolution and enhanced accuracy. Optics express, 22(2), 1560-1568.

[9] Taylor, J. R. (1982). An Introduction to Error Analysis University Science. Mill Valley, Calif.

[10] Kreyszig, E. (1988). Engineering mathematics. Wiley.

[11] Mandelbaum, I., Bolshtyansky, M., Heinz, T. F., & Walker, A. R. H. (2006). Method for measuring the Raman gain tensor in optical fibers. JOSA B, 23(4), 621-627.

[12] Wisaksono, A., Pizzone, A., Gemmell, N. R., Younger, P. L., & Hadfield, R. H. (2017). Direct Downhole Temperature Measurement and Real Time Pressure-Enthalpy Model Through Photon Counting Fibre Optic Temperature Sensing. Stanford University 42nd Workshop on Geothermal Reservoir Engineering, Stanford.

[13] Brown, G. (2008). Downhole temperatures from optical fiber. Oilfield Review, 2009(20), 4.

[14] Smolen, J. J., & van der Spek, A. (2003). Distributed Temperature Sensing. A primer for Oil and Gas Production. Shell.

[15] Finger, J., & Blankenship, D. (2010). Handbook of best practices for geothermal drilling. Sandia National Laboratories, Albuquerque.

[16] Ferronsky, V. I. (2015). Application of Penetration Logging Techniques for Geoengineering Exploration. In Nuclear Geophysics (pp. 193-223). Springer International Publishing.

Chapter 6 – Conclusions

This chapter will summarise the individual conclusions of the previous results chapters and the broader conclusions of the whole body of work. It will discuss the significance of the work, offer a critical analysis, and suggest future work that could improve on the results.

6.1 SNSPDs arrays: conclusion and prospects

6.1.1 Summary of results

This thesis presents a full picture of the superconducting nanowires single-photon detector (SNSPD) technology, discussing key aspects of design, fabrication and promising application areas.

By employing a 4-ports power combiner, a Time-Division Multiplexing scheme (reported in *Chapter 4*) was accomplished and tested with two independently biased 4-pixels arrays, fabricated in the University of Glasgow cleanroom (James Watt Nanofabrication Centre). The 30 x 30 µm^2 array, has given extremely uniform responses during the electrical characterization (critical current equal to 38 µA) and the jitter computation (around 71 ps, at the 97% of the critical current). The optical response is also uniform but performances (~2.6% efficiency and ~250 Hz dark counts rate at 1550 nm and biased at the 97% of the critical current) are affected by an optical cavity optimized for a light-source around 2.3 µm.

The 60 x 60 µm^2 array, instead, includes a quarter wave optical cavity optimized for photon absorption at 1550 nm, however the efficiencies of the single-pixels vary in the range 9-25%. The electrical response is again uniform, with I_c in the range of 41-49 µA, but the FWHM jitters and the dark counts rates (both measured at the 92% of the I_c) varies from 116 to 163 ps and from 1 to 4 KHz, respectively.

Nevertheless, the simulations presented in § **4.5** indicate that a set of different on-chip resistors in parallel with superconducting nanowires may produce a code-division multiplexed array, at least for a small number of pixels. Thus, the modularity of the multiplexing protocols permits to merge the two readouts in order to extend the number of multiplexed pixels.

6.1.2 Outlook

For what concerns the large-area arrays, immediate goals could be:

- the fabrication of a 30 x 30 µm^2 device over an optical cavity optimized for 1550 nm in order to demonstrate how the poor efficiencies measured in § ***4.3.2*** is only due to the substrate;
- the fabrication a new 60 x 60 µm^2 detector, with higher efficiency and a timing-jitter as uniform and low as achieved for the 30 x 30 µm^2 array. Such detector could be coupled with a multi-mode optical fibre, overcoming the limitations of single-mode fibres about in terms of optical collection. The larger fibre-core and numerical aperture in multi-mode fibre implies higher photon-coupling capacity than single-mode fibre.

Concerning the code-division multiplexing scheme, a fabrication of the full device will indicate if the thermal load, introduced by palladium (Pd) resistors, can really compromise the functionality of an SNSPD. A successful proof-of-principle device would lead to further steps oriented to extend the number of on-chip multiplexed pixels via Pd resistors, according to the available cooling power.

During the time of writing, new scalable architectures were introduced [1], including an innovative frequency-multiplexed bias and readout scheme for 16 pixels [2].

6.2 Distributed fibre temperature sensing: conclusion and prospects

6.2.1 Summary of results

An SNSPD detector was also employed in a distributed fibre temperature sensing based on the collection of Raman backscattered photons. A profile of temperature over a length of 100 m with a spatial resolution of ~83 cm was achieved in an acquisition time of 200 minutes due to the availability of a single SNSPD and a laser power of ~0.4 µW.

The optical attenuation introduced is mainly due to a pulse selector that reduced the repetition rate of the laser, in order to extend the fibre under test to 100 m. Thus, to validate the result, the testbed, powered by 0.95 mW without that pulse selector, was used to sense the temperature of a heated section in a 2 m long fibre, in 12 minutes. The tests reveal the variations of temperature artificially created along the fibre, with a maximum error of 12 K and a standard deviation/mean absolute error of ~5.1 K.

6.2.2 Outlook

Future and realistic development for the Raman-based distributed fibre temperature testbed is the use of two detectors having efficiency of at least an order of magnitude higher than the 1% SNSPD used. Concurrently, a more powerful laser with a narrow linewidth would surely reduce noise on the signals and the relative acquisition time. In case of on-field tests in a geothermal borehole, some logistic issues could arise from the use of cryogenic equipment necessary to reach the operative temperatures of SNSPDs. A more compact battery-powered system is preferable.

Recent works have produced miniaturized cryogenic platforms for superconducting detectors [3]. However, the presented testbed is fully independent from the photodetector. Hence, InGaAs free-running detectors may replace the SNSPD detector.

A deeper development could be the use of waveguide integrated SNSPDs (Fig. 6.1). Such a solution would discriminate, on-chip, Stokes and Anti-Stokes backscattered photons, dramatically simplifying the system due to the removal of any in-fibre filter or splitter. This kind of photonic circuitry is already reported in literature [4].

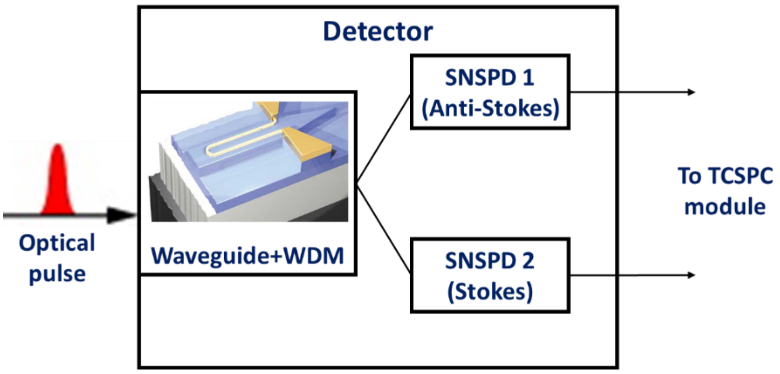

Fig. 6.1: Diagram of a waveguide integrated detector, including a wavelength division multiplexer (WDM) able to separate Stokes and anti-Stokes signal on-chip, simultaneously detected by two different SNSPDs.

References

[1] Zhao, Q. Y., Zhu, D., Calandri, N., Dane, A. E., McCaughan, A. N., Bellei, F. *et al.* & Berggren, K. K. (2017). Single-photon imager based on a superconducting nanowire delay line. Nature Photonics, 11(4), 247-251.

[2] Doerner, S., Kuzmin, A., Wuensch, S., Charaev, I., Boes, F., Zwick, T., & Siegel, M. (2017). Frequency-multiplexed bias and readout of a 16-pixel superconducting nanowire single-photon detector array. Applied Physics Letters, 111(3), 032603.

[3] Gemmell, N., Hills, M., Bradshaw, T., Rawlings, T., Green, B., Heath, R., Tsimvrakidis, K. *et al.* & Hadfield, R. (2017). A miniaturized 4 K platform for superconducting infrared photon counting detectors. Superconductor Science and Technology. In press.

[4] Kahl, O., Ferrari, S., Kovalyuk, V., Vetter, A., Lewes-Malandrakis, G., Nebel, C. *et al.* & Pernice, W. (2017). Spectrally multiplexed single-photon detection with hybrid superconducting nanophotonic circuits. Optica, 4(5), 557-562.

List of publications

Casaburi, A., **Pizzone, A.**, & Hadfield, R. H. (2014, May). Large area superconducting nanowire single photon detector arrays. In Photonics Technologies, 2014 Fotonica AEIT Italian Conference on (pp. 1-4). IEEE.

Wisaksono, A., **Pizzone, A.**, Gemmell, N. R., Younger, P. L., & Hadfield, R. H. (2017). Direct Downhole Temperature Measurement and Real Time Pressure-Enthalpy Model Through Photon Counting Fibre Optic Temperature Sensing. Stanford University 42nd Workshop on Geothermal Reservoir Engineering.